UNIVERSITÀ DEGLI STUDI DI CATANIA
facoltà di scienze matematiche, fisiche e naturali
Dottorato in Fisica

Vincenzo Minissale

HADRONIZATION VIA QUARK COALESCENCE OF THE QUARK GLUON PLASMA AT ULTRARELATIVISTIC HEAVY-ION COLLISIONS

Tesi di Dottorato

Relatore:
Prof. Vincenzo Greco
Correlatore:
Dott. Salvatore Plumari
Dott. Francesco Scardina

Ciclo XXIX 2013/2016

CONTENTS

ABSTRACT

Within the general framework of Standard Model, the Quantum Chromodynamics (QCD) is the fundamental theory that governs the dynamics of strongly interacting particles and has quarks and gluons as elementary constituents, they represent the fundamental degrees of freedom of the theory carrying the "color" charge. The QCD have two important and characterizing features, that are the colour confinement and the asymptotic freedom. The first one implies that quark and gluons can only exist as a confined colorless object inside hadrons. The second one is related to the non Abelian nature of the theory and consists in the decrease of interaction strength with the decreasing of interaction distance. The asymptotic freedom allow us to study the strong interaction in a perturbative regime for sufficiently high energy processes, and implies that under particular condition of temperature or density the strong interaction that confines quarks and gluons becomes smaller enough to release them. Hence a new state of matter can exist in which the colour charges are deconfined in a Quark Gluon Plasma (QGP), the predictions of Lattice Quantum Chromodynamics indicate that the critical temperature in which the nuclear matter experiences a phase transition is $T_c \approx 160MeV$. Heavy Ion Collisions (HIC) at ultrarelativistic energy can be used to probe the properties of nuclear matter under such extreme condition. In the studies of the Quark Gluon Plasma created in HIC is necessary taking into account that partonic behaviour in QGP is not directly projected on the observables measured in heavy ion collision experiments. This happens because the quark and gluon constituents must combine into colour-neutral objects: the hadrons. Thus the choice of the model for Hadronization process is a crucial point in order to have a comparison with experimental data. We are interested on an approach with the problem of hadronization of QGP that takes care about microscopic mechanism of hadronization. Within the microscopic description two different approaches have been developed: fragmentation and coalescence. In the fragmentation scheme each parton fragments into a jet of hadrons which carries a fraction of initial parton momentum. Instead coalescence model describes the recombination of two or three quarks adding their momenta to form mesons or baryons. The coalescence model that has a marginal role in the hadronization processes in pp collisions, has been able to explain at least two unexpected observations in heavy ion collisions, that other models can not explain simultaneously. In particular the coalescence model can predicts the enhancement of baryon to meson ratio at intermediate transverse momenta and the scaling of elliptic flow according to the constituent quark number that are observed in Au+Au collisions at RHIC. In this thesis we have developed a numerical code to implement an hadronization model based on a quark coalescence mechanism. Our first purpose has been to reproduce the transverse momentum spectra and the particle ratio at RHIC and LHC for pions, kaons, protons and Lambda with an implementation based on a coalescence model applied on a static medium. At RHIC and LHC we obtain a good description of transverse momentum spectrum in the whole range of momenta. Furthermore our model reproduces experimental data for both proton to positive pion ratio and Lambda to kaons ratio specially in the intermediate transverse momenta region where an anomalous large value is observed. The features of these ratios was one component of the so-called "baryonic puzzle". We can see that the ratio is quite well predicted from its rise at low transverse momenta up to the peak region and then the falling-down behaviour. However in both cases it is clear that in the region of $p_T \approx 5-7\, GeV$ there is a lack of baryon yield. At both RHIC and LHC such a lack of yield appears where coalescence becomes less important therefore one can say that it seems that the spectrum from AKK fragmentation function appears too flat. It is likely that studies of in-medium fragmentation function can solve it or it could be that coalescence contribution should extend to large p_T with respect to the present modelling. Then we have studied the hadronization effect with a coalescence model applied in the heavy quark sector. At both RHIC and LHC energies the relation between Heavy Quarks nuclear modification factor R_{AA} and the elliptic flow v_2 observed give indications that reveal a quite strong interactions between heavy quarks and the medium which is substantially beyond the expectations coming from perturbative QCD. Several theoretical efforts have been made to reproduce the R_{AA} and the v_2 observed in experiments but all the approaches show some difficulties to describe them simultaneously. A key result of our study is that when R_{AA} increases, elliptic flow decreases and viceversa. Generally in order to get the same R_{AA} that we have without including coalescence is necessary to further increase the interaction, which causes an additional increase of the elliptic flow. Coalescence inverts this relation, implying a contemporary increase of both these two observables and this is fundamental to reproduce the experimental data. In the final part we have presented a more realistic implementation of coalescence model, in which we have developed a model self-consistently applied to the freeze-out hypersurface of a Boltzmann Transport equation. Comparing the transverse momentum distribution of pions, kaons and protons with the experimental data at RHIC and LHC we find a really good agreement in the intermediate transverse momentum region. While for higher momenta we slightly underestimate the experimental data, however this can be ascribed to the partonic spectrum that results over-suppressed in the region at high p_T. Finally we have studied the elliptic flow for pions and we have obtained that the coalescence overestimate the v_2 observed experimentally in the momentum region above $2\,GeV$, on the other hand in the same region the elliptic flow of fragmentation is about two times smaller than the experimental data. But an approach that take in account of both coalescence and fragmentation is able to give a reasonable description of the elliptic flow behaviour in a quite large range of momenta.

INTRODUCTION

Within the general framework of Standard Model, the Quantum Chromodynamics (QCD) is the fundamental theory that governs the dynamics of strongly interacting particles and has quarks and gluons as elementary constituents, they represent the fundamental degrees of freedom of the theory carrying the "color" charge. The QCD have two important and characterizing features, that are the colour confinement and the asymptotic freedom. The first one implies that quark and gluons can only exist as a confined colorless object inside hadrons. The second one is related to the non Abelian nature of the theory and consists in the decrease of interaction strength with the decreasing of interaction distance.

The asymptotic freedom allow us to study the strong interaction in a perturbative regime for sufficiently high energy processes, and implies that under particular condition of temperature or density the strong interaction that confines quarks and gluons becomes smaller enough to release them.

Hence a new state of matter can exist in which the colour charges are deconfined in a Quark Gluon Plasma (QGP), the predictions of Lattice Quantum Chromodynamics indicate that the critical temperature in which the nuclear matter experiences a phase transition is $T_c \approx 160 MeV \sim 10^{12} K$.

Heavy Ion Collisions (HIC) at ultrarelativistic energy can be used to probe the properties of nuclear matter under such extreme condition.

Signatures of a Quark Gluon Plasma formation became manifest in the experiment with energies up to 200 $AGeV$ performed at Relativistic Heavy Ion Collider (RHIC) at Brookhaven National Laboratory. Further confirmations as well as new discoveries have been coming from the experiments at Large Hadron Collider (LHC) started in 2010 where it possible reach energies up to 5.5 TeV

In the studies of the Quark Gluon Plasma created in HIC is necessary taking into account that partonic behaviour in QGP is not directly projected on the observables measured in heavy ion collision experiments. This happens because the quark and gluon constituents must combine into colour-neutral objects: the hadrons. Thus the choice of the model for Hadronization process is a crucial point in order to have a comparison with experimental data.

There are at least two different classes of approaches to deal with the problem of hadronization of QGP. The first one is based on a statistical model, this approach does not care about microscopic mechanism that leads to production of hadrons, because it assumes that the number of hadrons and the spectra follows the kinetic and chemical equilibrium laws of statistical mechanics.

The other class of modeling takes care about microscopic mechanism of hadronization. Within the microscopic description two different approaches have been developed: fragmentation and coalescence. In the fragmentation scheme each parton fragments into a jet of hadrons which carries a fraction of initial parton momentum. Instead coalescence model describes the recombination of two or three quarks adding their momenta to form mesons or baryons.

The coalescence model that has a marginal role in the hadronization processes in pp collisions, has been able to explain at least two unexpected observations in heavy ion collisions, that other models can not explain simultaneously.
In particular the coalescence model can predicts the enhancement of baryon to meson ratio at intermediate transverse momenta and the scaling of elliptic flow according to the constituent quark number that are observed in Au+Au collisions at RHIC.

In this work we have used a numerical code that implement an hadronization model based on coalescence mechanism, where fragmentation has been taken into account to reproduce the features of hadron spectra at high transverse momentum accounting for the transition between the two mechanism.
Initially we have compared the experimental data at RHIC and LHC with the transverse momentum spectra of pions, kaons, protons, Lambda and ϕ, including decay of the main resonances, and also the respective baryon to meson ratio obtained from our implementation of coalescence model, finding a good agreement.
Then we have studied the effect of hadronization in the heavy quark sector. Heavy quarks and their bound states are recognized as probes of the medium produced in ultrarelativistic heavy-ion collisions and its early stages. At both RHIC and LHC energies the relation between Heavy Quarks nuclear modification factor R_{AA} and the elliptic flow v_2 observed is not successfully predicted by any of different models. We show in our study that coalescence can modify the relation between these two observables and lead to a significantly better description of the experimental data.
A more realistic implementation of coalescence model has been the final subject of our studies. We have developed a coalescence model self-

consistently applied to the freeze-out hypersurface of a Boltzmann Transport equation solved with the realistic initial condition of ultrarelativistic heavy-ion collisions. The Relativistic Boltzmann Transport equation describes the system in terms of a space-time evolution equation for the one body distribution function. Within this approach we have an unified description of short range interactions, due to collisions between particles, and long range interactions, associated to mean field dynamics that drives the equation of state. A dynamical coalescence coupled with a Boltzmann Transport Equation allow to study the effect, on final particles, of transport coefficient of QGP, such as shear viscosity, or spacial and time informations that regard particles formation of different species. Moreover this approach can allow one to study the consequence of initial fluctuations in phase-space or the effect of space-momentum correlation on the final elliptic flow of mesons and baryons.

This thesis is divided in six chapter.

In the **chapter 1**, we will present the general features and the peculiarity of Quantum ChromoDynamics.

In **chapter 2**, we give a primer of the ultra-relativistic heavy-ion collisions and the main probes and observables of the formation of the Quark Gluon Plasma.

In **chapter 3**, we introduce the problem of Hadronization and the main features of three different Hadronization processes with a focus on the coalescence model where we describe the general approach to coalescence process, then the Wigner formalism and the method used for the implementation of numerical code.

In **chapter 4**, we will show the comparison between experimental data from RHIC and LHC and the results of our implementation.

In **chapter 5**, we introduce the principal characteristics of heavy quarks and our study of the impact of coalescence for the results for the

Nuclear modification factor and the elliptic flow of D meson.

In **chapter 6**, we present the basic theory of the Boltzmann Equation, the numerical implementation and the coupling of the coalescence model. Finally we show the results of our model for spectra and elliptic flow both at RHIC and LHC in comparison with the experimental data. A main finding is that only an hadronization by coalescence plus fragmentation is able to correctly describe the shape of the elliptic flow observed in experiments.

CHAPTER 1

QUANTUM CHROMO DYNAMICS

1.1 Introduction to QCD

The modern physics aim is to describe the elementary building blocks of matter and the forces that rule on them. At present the Standard Model is the most comprehensive physical theory ever developed, that has been experimentally tested with high accuracy. In the Standard Model, gauge bosons are defined as force carriers that mediate the strong, weak, and electromagnetic fundamental interactions. The different type of gauge bosons, all with spin 1, are the *photon* that mediate the electromagnetic force, W^+, W^-, Z^0 that mediate weak interactions and *gluons* that are the carriers of strong interaction between color charged particles.

The Standard Model includes 12 elementary particles of spin ½, known as fermions. Each fermion has a corresponding antiparticle. There are six quarks (up, down, charm, strange, top, bottom), and six leptons (electron, electron neutrino, muon, muon neutrino, tau, tau neutrino). These particles are considered as point particles. All the other particles that have been discovered over the years, the *hadrons*, are composite particles consisting of three or two quarks, respectively. The quarks are fermions having not only the flavour degrees of freedom (up, down, strange, charm, bottom, top), but also color degrees of freedom (red, blue and green).

Isolated color has never been observed experimentally, which indicates that quarks are always bound together to form color-white composite objects. Baryons (proton, neutron, Λ, Σ, ...) comprise three valence quarks, and mesons (π, ρ , K , J/ψ ...) are made of a quark-antiquark pair. They are the simplest color-white constructions of hadrons, but possible multi-quark systems may exist.

The concept of color, as well as the quantum dynamics of color, was first proposed by Nambu [1] and this theory is now called “Quantum Chromodynamics” (QCD). This is a generalization of Quantum Electrodynamics (QED), which is a quantum theory of charged particles and the electromagnetic field. QCD (respectively QED) has gluons (the photon) as spin-1 gauge bosons that mediate the force between quarks (charged particles). Although QCD and QED look similar, there is a crucial difference: whereas the photon is electrically neutral and therefore transfers no charge, the gluons are not neutral in color. The fact that gluons themselves carry color is related to the fundamental concept of non-Abelian or Yang-Mills gauge theory [2]. The term “non Abelian”refers to the color SU(3) algebra on which QCD is constructed.

QCD has two main features that can be traced back to its non abelian structure. At high energies, the interaction becomes small, and quark and gluons interact weakly, it is called “asymptotic freedom” [3] [4], while at low energy the interaction becomes strong and leads to the confinement of color. The asymptotic freedom, which is a unique aspect of non-Abelian gauge theory, is related to the anti-screening of color charge. Because the gauge fields themselves have color, a bare color charge centered at the origin is diluited away in space by the gluons. Therefore, as one tries to find the bare charge by going through the cloud of gluons, one finds a smaller and smaller portion of the charge. This is in sharp contrast to the case of QED, where the screening of a bare charge takes place due to the cloud of, for example, electron-positron pairs surrounding the charge.

As the typical length scale decreases, or the energy scale increases, the coupling strength decreases in QCD. This is why we can expect QGP at high temperature, for which the typical thermal energies of the quark and gluons are large entering the weak regime of the interaction.

The strenght of the interaction in QCD becomes stronger at long distances or at low energies. This is a signature of the confinement of color. Indeed, the phenomenological potential between a quark and an anti-quark at large separation increases linearly. Consequently, even if we try to separate the quark and the anti-quark beyond some critical distance the potential energy becomes large enough to allow a new quark-antiquark pair pops up from the vacuum. Then, the original quark-antiquark pair becomes two pairs. In this way, quarks are always confined inside hadrons and can never be isolated.

Because the QCD coupling strength, α_S, becomes large at long distances, which means low energies (about 2-3 GeV), we encounter a technical difficulty, i.e. we cannot adopt a perturbative method. Wilson's lattice gauge theory [5] may be used to circumvent this problem. It treats four-dimensional space-time not as a continuum, but as a lattice, just as in crystals, in which quarks occupy lattice points while the gauge field occupies lattice links. By this lattice discretization, one may solve QCD utilizing Monte Carlo numerical simulations. Results on quark-antiquark interaction confirm that the potential energy is indeed proportional to the length of the string. This agrees with that of the string model, making the ideas of confinement feasible.

1.2 Classical QCD action

The classical Lagrangian density of QCD contains quark and gluon fields as fundamental degrees of freedom; also, it is designed to have a local color $\mathrm{SU}_C(3)$ simmetry. For a quark with mass m, the Lagrangian density is given by

$$\mathscr{L}_{cl} = \bar{q}^{\alpha}(i\not{D}_{\alpha\beta} - m\delta_{\alpha\beta})q^{\beta} - \frac{1}{4}F^{a}_{\mu\nu}F^{\mu\nu}_{a} \tag{1.1}$$

The quark field q^{α} belongs to the $\mathrm{SU}_C(3)$ triplet, the gluon field A^a_μ belongs to the $\mathrm{SU}_C(3)$ octet. Therefore α runs from 1 to 3, while i runs from 1 to 8.

We define $\not{D} \equiv \gamma^{\mu}D_{\mu}$, where D_μ is a covariant derivative acting on the color triplet quark field:

$$D_\mu \equiv \partial + igt^a A^a_\mu \tag{1.2}$$

Here g is the dimensionless coupling constant in QCD; the t^a denotes the fundamental representation of $\mathrm{SU}_C(3)$ Lie algebra. They are traceless 3×3 hermitian matrices satisfying the following commutation relation and normalization:

$$[t^a, t^b] = if_{abc}t^c,\ tr(t^a t^b) = \frac{1}{2}\delta^{ab} \tag{1.3}$$

For later convenience, we also define the covariant derivative acting on the color-octet field:

$$\mathscr{D}_\mu \equiv \partial_\mu + igT^a A^a_\mu \tag{1.4}$$

Here T^a are the adjoint representations of the $\mathrm{SU}_C(3)$ Lie algebra. They are traceless 8×8 hermitian matrices given by $(T^a)_{bc} = -if_{abc}$.

The field strength tensor of the gluon $F^a_{\mu\nu}$ is defined as

$$F^a_{\mu\nu} = \partial_\mu A^a_\nu - \partial_\nu A^a_\mu - gf_{abc}A^b_\mu A^c_\nu \tag{1.5}$$

By introducing $A_\mu \equiv t^a A^a_\mu$ and $F_{\mu\nu} \equiv t^a F^a_{\mu\nu}$, we may simplify Eq.(1.5) as follows:

$$F^a_{\mu\nu} = \partial_\mu A^a_\nu - \partial_\nu A^a_\mu + ig[A_\mu, A_\nu] = \frac{-i}{g}[D_\mu, D_\nu] \tag{1.6}$$

The Lagrangian density, Eq.(1.1), is invariant under the $\mathrm{SU}_C(3)$ gauge transformation

$$q(x) \to V(x)q(x), \quad gA_\mu(x) \to V(x)(gA_\mu(x) - i\partial_\mu)V^\dagger(x) \tag{1.7}$$

where $V(x) \equiv \exp(-i\theta^a(x)t^a)$. To show this gauge invariance, it is useful to remember that $F_{\mu\nu}$ and $D_{\mu\nu}$ transform covariantly; i.e

$$F_{\mu\nu}(x) \to V(x)F_{\mu\nu}(x)V^\dagger(x), \qquad D_\mu(x) \to V(x)D_\mu(x)V^\dagger(x) \tag{1.8}$$

After the transformation, we obtain:

$$\begin{aligned} tr_c(F_{\mu\nu}F^{\mu\nu}) \to tr_c(V(x)F_{\mu\nu}V^\dagger(x)V(x)F^{\mu\nu}V^\dagger(x)) = \\ = tr_c(V^\dagger(x)V(x)F_{\mu\nu}V^\dagger(x)V(x)F^{\mu\nu}) = \\ = tr_c(F_{\mu\nu}F^{\mu\nu}) \end{aligned} \tag{1.9}$$

$$D_\mu(x)q(x) \to V(x)D_\mu(x)V^\dagger(x)V(x)q(x) = V(x)D_\mu(x)q(x) \tag{1.10}$$

in this way, the Lagrangian results invariant.

Observe, from Eq.(1.1), that the term $F_{\mu\nu}F^{\mu\nu}$ contains not only the standard kinetic term of the gauge fields, but also an interaction vertex with three gauge bosons, proportional to g, and a vertex with four gauge bosons, proportional to g^2. One can observe also that gauge invariance has fixed the three-boson, four-boson, and boson-fermion-fermion vertices in terms of a single parameter, the gauge coupling g.

1.3 Running Coupling Constant and Asymptotic Freedom

One of the most important feature of QCD is the asymptotic freedom. It was demonstrated that asymptotic freedom is possible only for the non-Abelian gauge theories [6] [7].

This phenomenon can be investigated analyzing the renormalization of a quantum field theory. In field theories, the quantum correction calculated with the perturbation theory have ultraviolet divergences which are originated from the states with high momenta. In the case of QCD and QED, that are renormalizable field theories, these divergences can always be absorbed in renormalized parameters. In QED we have the normalization of two quantities: the charge and the mass. We are interested in the charge. Can be defined a "naked" charge that is infinite, but not observable, and an "effective" charge that is measurable. As shown in Fig.(1.1) in every vertex there is a contribution due to the naked coupling constant. But we measure the summation of all the series terms, reducing the charge to an effective charge. We can proceed with an analogy from another physical situation, let consider a small charged sphere immersed in a dielectric medium. The charge polarises the near molecules of the medium which tend to become oriented toward the sphere. This causes a screening action that macroscopically appears as the dielectric constant. If a charged probe approaches the sphere in order to measure its charge, the minimum distance that can be reached is a decreasing function of the initial energy of the probe. Consequently, higher-energy probes will "see" a larger charge on the sphere. In QED the vacuum becomes, spontaneously, polarised at microscopic level; e^+e^- pairs appear continuosly for a short time and then recombine. In presence of a charged body the pairs become oriented. This leads to the formation of a virtual particle cloud around the charged body, that reduces the power of its charge at a distance by its screening action. As a consequence the effective charge is larger at smaller distances.

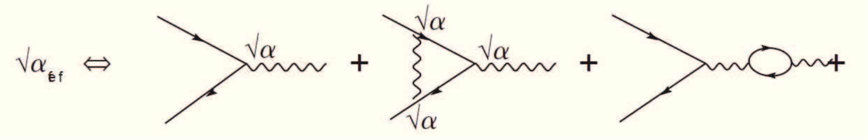

Figure 1.1: Lowest order diagram contributing to an electromagnetic vertex

The fine structure constant, in this way, is not constant, rather it evolves with the momentum transfer Q or, in other cases, with the centre of mass energy at which the measurement is performed. The same mechanism happens considering the formation of gluons from the QCD vacuum. The fundamental difference between QED and QCD lies in the possibility, in addition of quark-antiquark pair creation, for gluons to split in loops where other virtual gluons can be formed. These bosonic contributions have an opposite signs respect the fermionic loop. The effect of vacuum polarisation due to the quarks is similar to that which we have seen in electrodynamics, with the colour charges in place of the electric charge. The quark-antiquark pairs coming out of vacuum shield the colour charge, reducing its value for increasing distance, or for increasing momentum transfer in the measuring process. However, the action of gluons is a smearing of the colour charge called antiscreening. The net result is that the colour charges decrease with decreasing distance. Complete calculation of these diagrams after a standard renormalization at an energy scale named "renormalization point" leads to the expression for QCD running coupling constant in Eq.(1.11). The physical observables do not depend on the renormalization point but the coupling $\alpha = g^2/4\pi$ depends on it and therefore α depends on the momentum transfer, see Fig.1.3. It is possible to show [3] [4] that, for $N_f \leq 16$, α is a decreasing function of the renormalization point and therefore, in the case of QCD, with $N_f = 6$, α is a decreasing function of the momentum transfer, as indicated in the formula at the leading order:

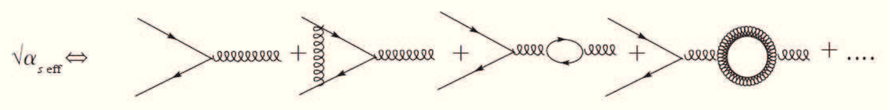

Figure 1.2: Lowest order diagram contributing to QCD vertex

$$\alpha_s(Q^2) = \frac{4\pi}{(11 - \frac{2}{3}N_f) ln(Q^2/\Lambda^2_{QCD})} \tag{1.11}$$

where $\Lambda_{QCD} \lesssim 200-250\, MeV$ is an intrinsic energy scale for the strong interactions.

Theories where the coupling becomes small in the UV are called *asymptotically free*. Asymptotic freedom implies that at large energies (and therefore at short distances) the fields which appear in the Lagrangian can be treated perturbatively. The other side of the coin, however, is that in an asymptotically free theory for energy comparable with $\Lambda_{QCD} = 200 MeV$, the coupling becomes strong, and the perturbative treatment is inadequate. This occurs at energy scales and size of the order of the hadrons.

1.4 Confinement

An important non-perturbative feature of the QCD is the colour confinement. The hypothesis of confinement says that hadrons can only exist in states with zero colour charge and quarks can only exist confined within hadrons. This hypothesis is supported by experimental results, in fact free quarks or gluons have never been observed in experiments, but there is no analytical description of confinement yet.

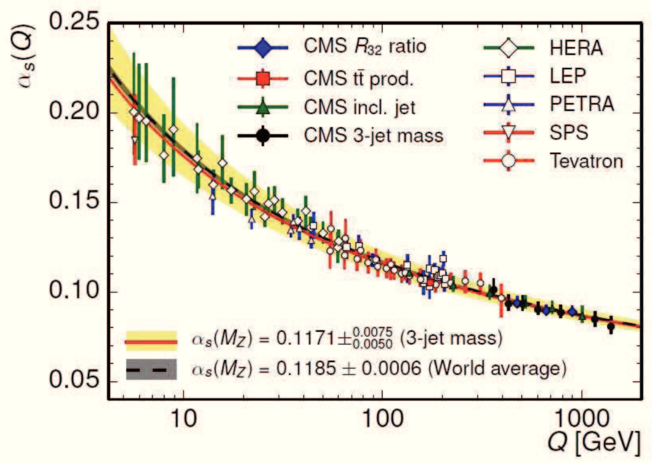

Figure 1.3: Running coupling as a function of the transfer momenta. The graphic have been obtained performing measure at various energy scales

Let us consider the simple case of a mesons. In a first approximation a meson is made up of a quark-antiquark pair and the colour field, with all its virtual particles, between them. The distance between quark and antiquark oscillates continuously with a maximum elongation of the order of the fermi. Indeed, the attractive force increases when the distance increases, because the cancellation of the two antiscreening clouds decreases. The colour field between a quark and an antiquark at distances of about one fermi is concentrated in a narrow "tube". When the separation between quark and antiquark increases, the length of the tube increases, but its diameter remains approximately constant. Therefore the field energy density remains constant and the total energy in the tube increases proportionally to its length. When the energy in the tube is large enough it becomes energetically convenient to break the tube producing a new quark-antiquark pair at the two new ends. We now have a second meson, which is colour neutral.
This can be described by a potential between a quark and an antiquark as a function of the distance as:

$$V(r) = Kr - \frac{4}{3}\frac{\alpha_s}{r} \tag{1.12}$$

The second term is Coulomb-like while the first term, named *string potential*, increases with the distance and is responsible for confinement. The typical value for the string tension parameter is $K \simeq 0.9\, GeV fm^{-1}$. The situation is similar for the quark confinement in a baryon, in which there are three colour tubes.

1.5 Chiral Symmetry

Another key property of QCD is the chiral symmetry which is a global symmetry dynamically broken at the low temperature ($T \lesssim 155\, MeV$). We first introduce the left-handed and right-handed quark fields (see

Appendix A for gamma matrices)

$$\left(q_L = \frac{(1-\gamma_5)q}{2} \quad ; \quad q_R = \frac{(1+\gamma_5)q}{2}\right)$$

They are eigenstates of the chirality operator γ_5 with eigenvalues ± 1, in the case of free quarks with zero masses the chirality is equivalent to the helicity $\sigma \cdot \hat{p}$. One says the Lagrangian of a system is chirally symmetric if it is invariant under the global $\mathrm{SU}(N_f)_L \times \mathrm{SU}(N_f)_R$ transformation that are given by:

$$\mathrm{SU}(N_f)_L = q_L \to e^{-i\theta_a^L \frac{\lambda_a}{2}} q_L \quad ; \quad \mathrm{SU}(N_f)_R = q_R \to e^{-i\theta_a^R \frac{\lambda_a}{2}} q_R \qquad (1.13)$$

where λ_a are the generator of the $\mathrm{SU}(N_f)$ group. This symmetry is equivalent to the symmetry that leave the Lagrangian invariant under global vector and axial vector transformations, $\mathrm{SU}(N_f)_V \times \mathrm{SU}(N_f)_A$.

The chiral symmetry is an approximate symmetry for the Lagrangian of QCD seen in Eq.(1.1), but in the so called chiral limit ($m \to 0$) this symmetry is exact. On the other hand, from the analysis of hadrons spectra there are no evidence of chiral symmetry and therefore one should conclude that chiral symmetry is not realized in the ground state (vacuum) of QCD.

However this is not in contradiction with the QCD classical Lagrangian that would predict a nearly exact chiral symmetry. In fact even if the Lagrangian has a symmetry it can happens that it is not realized in the ground state, in other words it is spontaneously broken (More precisely is the $\mathrm{SU}(N_f)_V$ symmetry that is spontaneously broken).

A simple example for Spontaneous Symmetry Breaking is given by a ferromagnet. The action governing its microscopic dynamics is invariant under spatial rotations. For instance, we can describe a ferromagnet by an Hamiltonian of the type

$$\mathscr{H} = -J \sum_{i,j} s_i \cdot s_j$$

introducing a vector variable s_i associated to each site i, where $J > 0$ and the sum is restricted to nearest-neighbour pairs. Above a critical temperature a ferromagnet has a unique ground state, with zero magnetization. Of course this state respects the rotational invariance, since on it the expectation value of the magnetization $M = \langle s_i \rangle$ vanishes, and therefore no preferred direction is selected. Below a critical temperature instead it becomes thermodynamically favourable to develop a non-zero magnetization, and in this new vacuum $M \neq 0$ and the full SO(3) rotational symmetry is broken to the subgroup SO(2) of rotations around the magnetization axis. The original invariance of the Lagrangian is now reflected in the fact that, instead of a single vacuum state, there is a whole family of vacua related to each other by rotations, since the magnetization can in principle develop in any direction. However, the system will choose one of these states as its vacuum state. The symmetry is then said to be spontaneously broken by the choice of a vacuum.

The mechanism responsible for chiral spontaneous symmetry breaking is of non-perturbative nature and is related to the existence of a quark condensate different from zero $\langle \hat{q} q \rangle = -(240 MeV)^3$.
The spontaneous breaking for chiral symmetry was introduced by Nambu and Jona-Lasinio in their model of an effective theory of nucleons and meson [8]. In 2008 Nambu was awarded the Nobel Prize "for the discovery of the mechanism of spontaneous broken symmetry in subatomic physics".
An important consequence of the spontaneous breaking of an exact continuous global symmetry is the existence of a massless mode, the so called “Goldstone boson”, which, in the case of chiral symmetry, can be identified with pions. If chiral symmetry was a perfect symmetry of QCD the pions should be massless. However due to the non-zero value of $\langle \hat{q} q \rangle$ quark masses acquire an extra effective mass, called *constituent*, of about $m \approx 300 MeV$ and chiral symmetry for QCD becomes

not exact. Hence we expect that pions have a finite mass that has to be, however, small compared to the masses of all other hadrons, in fact the mass of pions is about 140 MeV, quite smaller than the proton mass, for example, that is 940 MeV. This QCD model gives rise to a dynamical mass contribution without a need of a Higgs mechanism for spontaneous electroweak symmetry breaking. We understood also that for heavy quarks such dynamical mass is not a main contribution to their mass values, which instead depends quite uniquely on the Higgs mechanism (Fig.(1.4)).

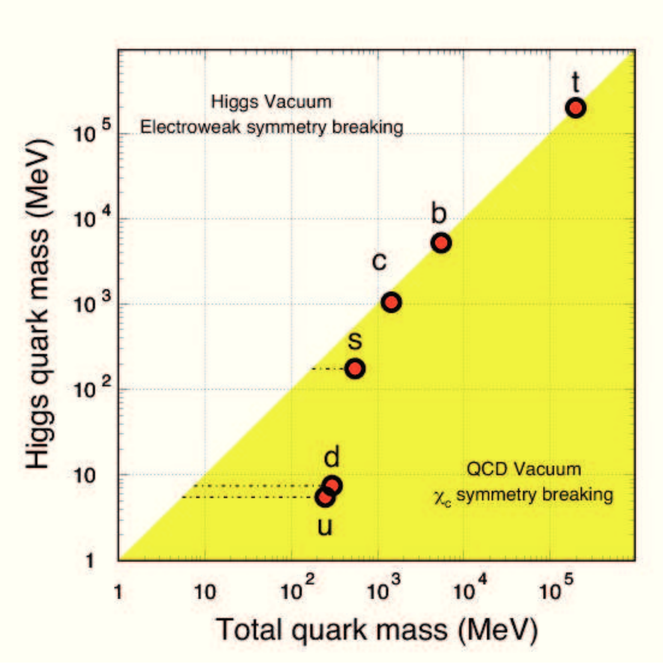

Figure 1.4: Comparison of physical quark masses with the QCD mass estimate. Light quarks fall in the domain of chiral symmetry breaking, while all heavy quark masses seem to arise totally from Higgs mechanism.

1.6 Quark Gluon Plasma

Asymptotic freedom suggests that under particular condition of temperature or density the interaction which confine quarks and gluons in-

side hadrons becomes smaller enough to release them. Thus a new state of the matter can exist in which the color charges are deconfined in a Quark Gluon Plasma (QGP).
There are two methods for the creation of the Quark Gluon Plasma

- QGP at high T. We assume that the QCD vacuum is heated in a box. At low temperature, hadrons, such as pions, kaons, etc., are thermally excited from the vacuum. Note that only the color-white particles can be excited by the confinement at low energies. Because the hadrons are all roughly the same size (about 1 fm), they start to overlap with each other at a certain critical temperature, T_C. Above this temperature, the hadronic system dissolves into a system of quarks and gluons (QGP). Note that in the QGP thus produced the number of quarks, n_q , is equal to that of anti-quarks, $n_{\bar{q}}$. The various model calculations and the Monte Carlo lattice QCD simulations yield $T_c = 150 \sim 200$ MeV. Although this is extremely high in comparison with (for example) the temperature at the center of the Sun, 1.5×10^7 K = 1.3 keV, it is a typical energy scale of hadronic interactions and can be obtained in laboratories, furthermore this phase of the matter should have existed in the early stage of Universe life up to a time of about $10-20\ \mu s$ after the Big Bang.

- QGP at high ρ. Let us put a large number of baryons into a cylinder with a piston and compress the system adiabatically, keeping $T \sim 0$. The baryons start to overlap at a certain critical baryon density, ρ_c, and dissolve into a system of degenerate quark matter. The quark matter thus produced is of high baryon density with $n_q \gg n_{\bar{q}}$. Model calculations show that $\rho_c = (\text{several}) \times \rho_{nm}$, where $\rho_{nm} = 0.16\ fm^{-3}$ is the baryon number density of normal nuclear matter

Based on the two recipes for high T and high ρ, we should expect to find QGPs in three places: (i) in the early Universe (T), (ii) at the center of compact stars (ρ)and (iii) in the initial stage of colliding heavy nuclei at high energies (T, ρ).

(i) In the early Universe, about 10^{-5} s after the cosmic Big Bang. According to Friedmann's solution [9] of Einstein's gravitational equation, the Universe experienced an expansion from a singularity at time zero. This scenario has been confirmed by the formulation of Hubble's law for the red shift of distant galaxies [10]. Hubble's law (Fig.1.5) states that: all objects observed in deep space (intergalactic space) are found to have a Doppler shift observable relative velocity to Earth, and to each other; and that this Doppler-shift-measured velocity, of various galaxies receding from the Earth, is proportional to their distance from the Earth and all other interstellar bodies.

$$v = H_0 \times l \tag{1.14}$$

where $H_0 = 65 - 79\,\mathrm{km}\,s^{-1}\,\mathrm{Mpc}^{-1}$ is the Hubble constant .

If we extrapolate our expanding Universe backward in time toward the Big Bang, the matter and radiation become hotter and hotter, resulting in the "primordial fireball," as named by Gamow. The discovery of $T \simeq 2.73\,\mathrm{K} \sim 3 \times 10^{-4}\; eV$ cosmic microwave background (CMB) radiation by Penzias and Wilson [11] confirmed the remnant light of this hot era of the Universe. In addition, the hot Big Bang theory explains the abundance of light elements (d, He, Li) in the Universe as a result of the primordial nucleosynthesis. If we go back further in time to $10^{-5} \sim 10^{-4}\; s$ after its inception, the Universe is likely to have experienced the QCD phase transition at $T = 150 \sim 200\,\mathrm{MeV}$ and an electro-weak phase transition at $T \sim 200\,\mathrm{GeV}$.

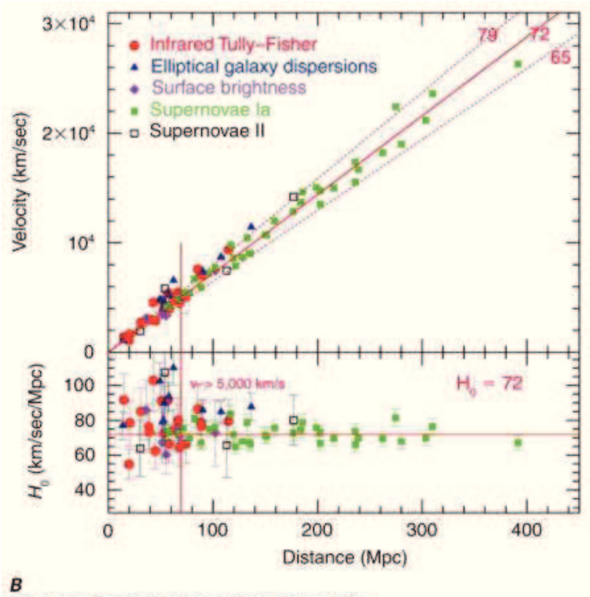

(Wendy L. Freedman, Observatories of the Carnegie Institution of Washington, and NASA)

Figure 1.5: Hubble law

(ii) At the core of super-dense stars such as neutron stars and quark stars. There are three possible stable branches of compact stars: white dwarfs, neutron stars and quark stars. The white dwarfs are made entirely of electrons and nuclei, while the major component of neutron stars is liquid neutrons, with some protons and electrons. The first neutron star was discovered as a radio pulsar in 1967 [12]. If the central density of the neutron stars reaches $5-10\ \rho_{nm}$, there is a fair possibility that the neutrons will melt into the cold quark matter. There is also a possibility that the quark matter, with an almost equal number of u, d and s quarks (the strange matter), may be a stable ground state of matter; this is called the strange matter hypothesis. If this is true, quark stars made entirely of strange matter become a possibility. In order to elucidate the structure of these compact stars, we have to solve the Oppenheimer-Volkoff equation [13], obtained from the Einstein equation, together with the equation of states for the superdense matter.

(iii) In the initial stage of the "Little Bang" by means of relativistic nucleus-nucleus collisions with heavy ion accelerators. Suppose we accelerate two heavy nuclei such as Au nuclei (A = 197) up to relativistic/ultra-relativistic energies and cause a head-on collision. In such relativistic energies, the nuclei are Lorentz-contracted as "pancakes". When the center-of-mass energy per nucleon is more than about 100 GeV, the colliding nuclei tend to pass through each other, and the produced matter between the receding nuclei is high in energy density and temperature but low in baryon density (see paragraph 2.1).

The Relativistic Heavy Ion Collider (RHIC) at Brookhaven National Laboratory and the Large Hadron Collider (LHC) at CERN provide us with this situation.

Phase diagram of the QCD

The above consideration bring us to sketch the phase diagram for the QCD matter Fig.(1.6). In the horizontal axis there is the baryon chemical potential μ_B, while in vertical axis there is the temperature, both quantities are expressed in MeV. The cold nuclear matter, as one can find in the inner part of a lead nucleus, has a temperature equal to zero and a chemical potential μ_B equal to 940 MeV.

In correspondence to $\mu_B = 0$ and T =170 MeV the matter undergoes a cross over from the confined phase of hadronic gas to a quark gluon plasma (QGP). As we have seen this phase should have existed in the early phase of the universe after the Big-Bang. In the region of non zero μ and low temperature there is also a phase transition towards the QGP phase, the place in which may exist this condition is the interior of neutron stars. The phase transition in this region seems to be of first order. For some moderate value of μ and T a critical point is expected,

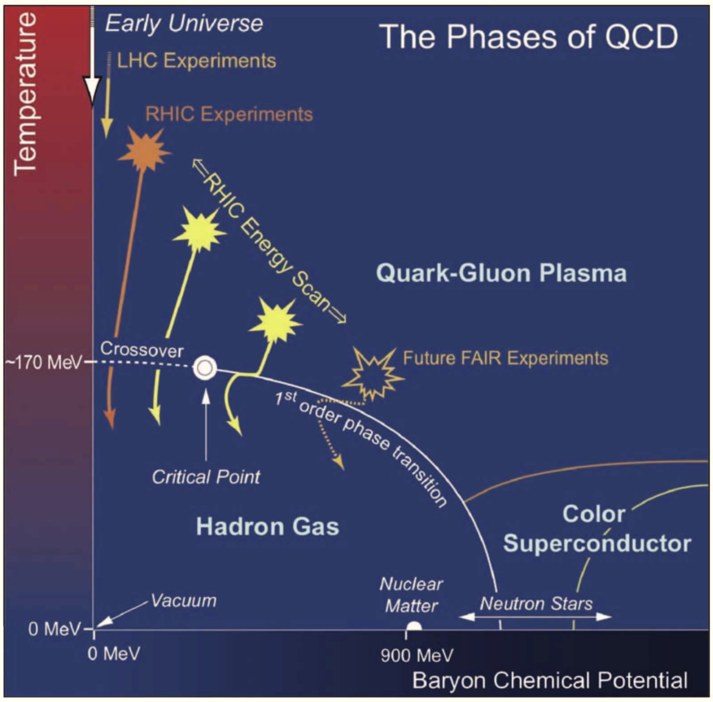

Figure 1.6: Phase diagram of QCD matter in the (T, μ) plane

for which the first order transition becomes a cross-over. The only possibility to create the Quark gluon plasma in laboratory is to perform ultra-relativistic heavy-ion collisions that will be discussed in the next chapter.

CHAPTER 2

QGP IN HEAVY ION COLLISION

A main tool to investigate the properties of nuclear systems, especially under conditions far from the one of stable nuclei, has been provided by heavy-ion collisions.

Over the years, nuclear collision energies have increased from beam kinetic energies of a few MeV/nucleon on fixed targets in small university laboratories to, at present, collider of very high energy of few TeV per nucleon in large laboratories with international collaborations. As the energy is increased, the relevant degrees of freedom change. At the lowest energies, the nucleus may remain intact or be broken up into light nuclear fragments. As various thresholds for particle production are reached, some of the energy of the system may go into producing new particles, such as pions or kaons. At high enough energies, the relevant degrees of freedom are expected to be quarks and gluons, forming the quark-gluon plasma, rather than hadrons.

The modern era of heavy-ion collisions arrived with beam energies of 10-200 GeV/nucleon at fixed-target facilities: the Alternating Gradient Synchrotron (AGS) at Brookhaven National Laboratory (BNL) and the Super Proton Synchrotron (SPS) at the European Center for Nuclear

Research (CERN). Both the AGS and the SPS accelerated protons and several types of ions onto fixed targets of heavy nuclei.

In 2001 has started the activity at RHIC (Relativistic Heavy Ion Collider) where it was possible to reach energies up to 200 GeV for nucleons. The experiments at RHIC have supplied a large amount of observables that have permitted to start a quantitative study of the Quark Gluon Plasma properties [14] [15] [16] [17]. In 2010 the experiments at LHC have started with an energy of 2.7 TeV per nucleons and in 2016 have been performed experiments with the highest energy accessible at LHC that is 5.5 A/TeV. In the first part of this chapter the main features of the collision dynamic and the evolution of the matter created in such collisions will be describe, instead in the final part of the chapter the observables that allow us to identify if a new state of matter have been created during the collisions, will be briefly examined.

2.1 Collision Dynamics

We will briefly sketch the main aspect of the heavy-ion collision at the relativistic energies.

The incoming nuclei comes at a velocity close to the speed of light and so they are strongly Lorentz contracted along the beam direction and in the center of mass frame they appear as two tiny disk of thickness $2R/\gamma_{CM}$, where R is the nuclear radius. The amount of contraction γ_{CM} can be easily calculated as

$$\gamma_{CM} = \frac{1}{\sqrt{1-b^2}} = \frac{1}{\sqrt{(1-\frac{p_z^2}{E_{CM}^2})}} \tag{2.1}$$

Where E_{CM} is the energy in the center of mass frame (see Appendix B). However, due to the uncertainty principle, the longitudinal size of nuclei cannot be smaller than a value Δz which depends on the energy of the

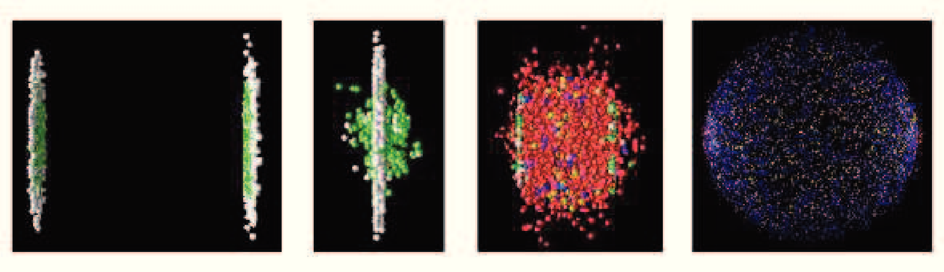

Figure 2.1: Heavy ion collision sequence

collision; for example if the energy of the collision is about 200 GeV then Δz is about 1 fm. This implies a geometrical delocalization of the nucleons inside the nuclei that consequently pass through each other and leave the region of the collision. Such a transparency behaviour of ultra-relativistic nuclei increases with the energy of the collision and allows to create in the central region of the collision a matter that in not contaminated by the original baryonic matter of the colliding nuclei.

As well established by the deep-inelastic lepton-hadron scattering experiments, the nucleon is composed of valence quarks and the wee partons (gluons and sea-quarks). Wee partons have a much smaller momentum fraction (x) of the nucleon compared with the valence quarks, and the number of wee partons increases as x approaches zero.

The wee partons may be considered as vacuum fluctuations which couple to the fast-moving valence quarks passing through the QCD vacuum [18]. Alternatively, the wee partons may be regarded as part of a coherent classical field created by the source of fast partons, which is called the color glass condensate [19]. Because of its non-perturbative nature, the typical momentum p, of the wee partons is of order Λ_{QCD} ($\sim$ 200 MeV), which characterizes the strong interaction scale of QCD. Since nucleons and nuclei are always associated with these low-momentum wee partons, the longitudinal size of hadrons or nuclei, Δz, can never be smaller than $1/p \sim 1$ fm owing to the uncertainty principle at ultra-high

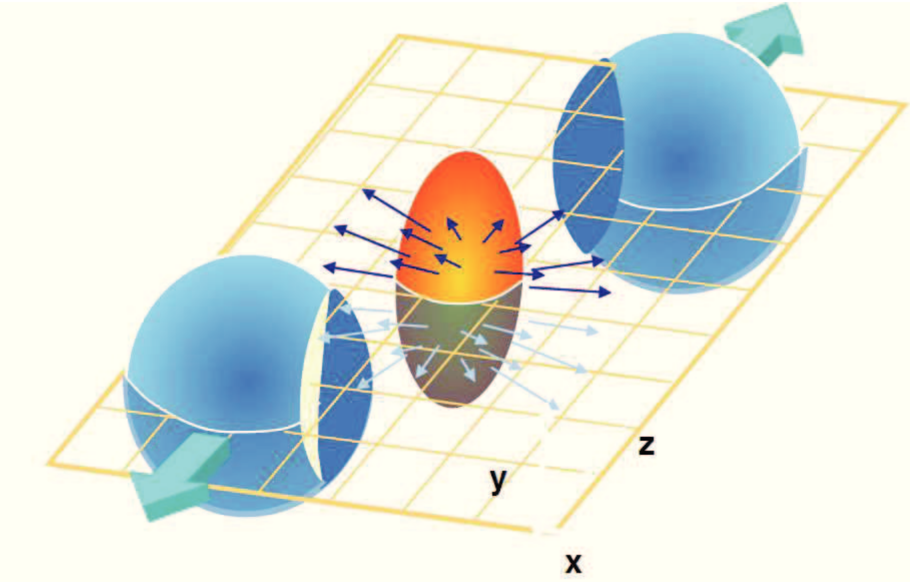

Figure 2.2: Non-central (b≠0) relativistic nucleus-nucleus collision.

energies,

$$\Delta z \geq \frac{1}{p} \approx 1\,\mathrm{fm} \tag{2.2}$$

As a consequence, the two incoming nuclei in the center-of-mass frame before the collision wear the “fur coat of wee partons” [18] of typical size 1 fm, while the longitudinal size of the wave function of a valence quark is $\sim 2R/\gamma_{cm}$. Therefore, the wee partons are expected to play a vital role at ultra-high energies which fulfil the condition

$$\gamma_{cm} > \frac{2R}{1\,\mathrm{fm}} \tag{2.3}$$

in Pb+Pb collisions this condition is reached at $\sqrt{s} \approx 30\,GeV$.

After the head-on collision of two beams of partons, many virtual quanta and/or a coherent field configuration of the gluons will be excited. It takes a certain proper time, τ_{de} (de-excitation or de-coherence time), for these quanta to be de-excited to real quarks and gluons. The de-excitation time, τ_{de} would typically be a fraction of 1 fm ($\sim 1/\Lambda_{QCD}$)’ or it could be much less than 1 fm. The state of matter for $0 < \tau < \tau_{de}$ is said

to be in the pre-equilibrium stage.
Since τ_{de} is defined in the rest frame of each quantum, it experiences Lorentz dilation and becomes $\tau = \tau_{de}\gamma$ in the center-of-mass frame of the collision, where γ is the Lorentz factor of each quantum. This implies that slow particles emerge first near the collision point, while the fast particles emerge last, far from the collision point. This phenomenon is called the "*inside-outside cascade*".
The real partons produced during the de-excitation process interact with each other and constitute an equilibrated plasma (quark-gluon plasma). We define $\tau_0(> \tau_{de})$ as a proper time within which the system is equilibrated. τ_0 depends not only on the basic parton-parton cross-section but also on the density of partons produced in the pre-equilibrium stage.
The highly excited matter thus produced cools down and then hadronizes into mesons and baryons, which are eventually observed in the detectors. This thesis focus just on the impact of the hadronization process assuming that quarks can either recombine and fragment (see next chapter).

An important role in the collision dynamics is played by the geometric aspects, that can be described using the *Glauber model* presented in the following section.

2.2 Glauber Model

The Glauber model is based on the geometrical configuration of the nuclei in order to estimate the initial spatial distribution just after the nuclei collide. It is a semiclassical model in which the nucleus-nucleus collisions are treated as multiple nucleon-nucleon interaction:a nucleon of incident nucleus interacts with target nucleons with a given density distribution. Nucleons are assumed to travel in straight lines, and are not deflected after the collisions, which holds as a good approximation at very high energies. Also, the nucleon-nucleon inelastic cross-section, σ_{NN}^{in} ,is assumed to be the same as that in the vacuum. The justification

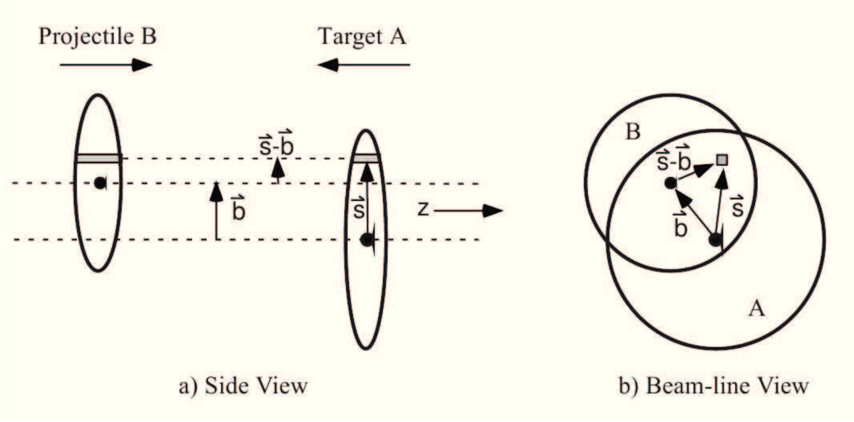

Figure 2.3: Representation of a collision between the nuclei A and B at a given impact parameter: (a) trasverse view, (b) longitudinal view

for the use of a geometrical model is that at high energies the De Broglie wave length of the nucleons are smaller with respect to the typical nuclear sizes. Moreover nucleons are assumed to travel in straight lines and are not deflected after the collision and according to eikonal approximation the multiple interaction can be considered as independent.

In order to describe the Glauber model we begin by introducing the nuclear overlap function $T_{AB}(b)$ [20]

$$\hat{T}_{AB}(\mathbf{b}) = \int \hat{T}_A(\mathbf{s})\hat{T}_B(\mathrm{s}-\mathbf{b})d^2s \tag{2.4}$$

where b is the impact parameter and s is the transverse coordinate; while $\hat{T}_A$ and $\hat{T}_B$ are the nuclear tickness function that give the probability to find a nucleon per unit of transverse area and it is defined as

$$\hat{T}_A(\mathbf{s}) = \int \hat{\rho}_A(\mathbf{s}, z_A)dz_A \tag{2.5}$$

Being $\hat{\rho}_A$ the nuclear mass number density normalized to mass number A, that in case of heavy ion is usually is parametrized as a Wood Saxon distribution

$$\rho = \frac{\rho_0}{1+\exp(\frac{r-R}{a})}.$$

Through the nuclear thickness function and the nuclear overlap function it is possible to evaluate the number of binary nucleon nucleon collision N_{coll} and the number of the participant nucleons N_{part}, that are both strongly related to the value of the impact parameter b.

$$N_{coll}(b) = AB\hat{T}_{AB}(b)\sigma_{inel}^{NN} \tag{2.6}$$

$$\begin{aligned} N_{part}(b) = A \int \hat{T}_A(\mathbf{s})\{1-[1-\hat{T}_B(\mathrm{s}-\mathbf{b})\sigma_{inel}^{NN}]^B\}d^2s + \\ B \int \hat{T}_B(\mathbf{s}-\mathbf{b})\{1-[1-\hat{T}_A(\mathrm{s})\sigma_{inel}^{NN}]^A\}d^2s \end{aligned} \tag{2.7}$$

The number of binary collisions and the number of participant cannot

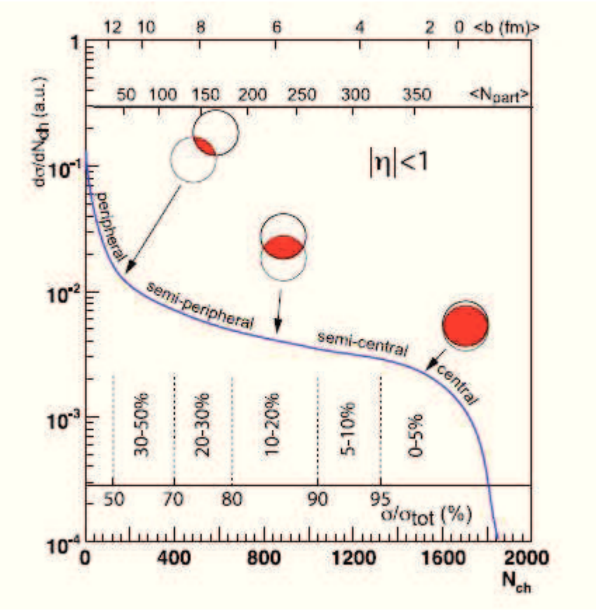

Figure 2.4: Cross section observed in function of N_{ch}. On the x-axes can be seen the relations between N_{ch}, N_{part} and b

be directly measured in experiments but they are related to the charged particle multiplicity N_{ch} that is a measurable quantity. Exploiting the relation between b, N_{part} and N_{ch} it is possible to trace back to the impact parameter of the collision performing a subdivision of N_{ch} in terms of centrality class, as shown in Fig.2.4. The relation between N_{ch} and

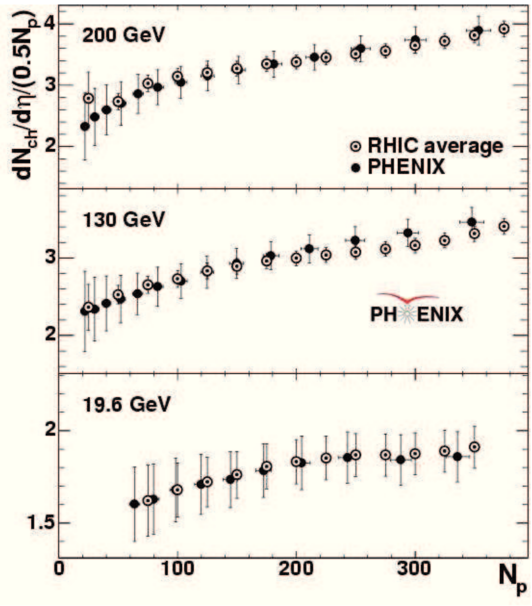

Figure 2.5: $dN_{ch}/d\eta$ RHIC average values of multiplicity production per participant pair (including PHENIX) compared to the PHENIX results [21].

N_{part} is shown in Fig. 2.5. is shown in figure.

The Glauber model can also be exploited to estimate the initial spatial distribution of partons in the transverse plane. In fact if one do not perform the integration over s in Eq.(2.7) and in Eq.(2.4) obtain respectively the density profile in the transverse plane of the number of participant and that of the binary collision. Whose linear combination could well approximate the density profile in the transverse plane of the partons created in the heavy-ion collision.

2.3 Time history of ultra-relavistic AA collisions

We now describe briefly the different stages of the evolution of relativistic heavy-ion collisions, as shown in Figs. 2.6 and Fig. 2.7

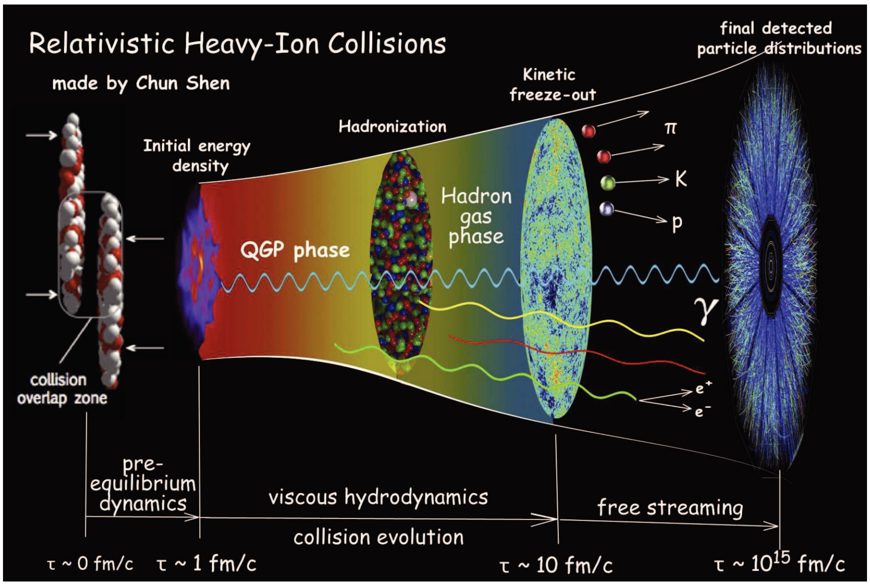

Figure 2.6: Sketch of how relativistic ion collision evolves in different stages

Pre-equilibrium stage and thermalization: $0 < \tau < \tau_0$

The nuclei meet each other at the point $(z,t) = (0,0)$. As we have said due to the Lorentz contraction the incoming nuclei are approximately transparent and thus they pass through each other. However, in the region of the collision is generated a strong color field, which causes an excitation of the vacuum and produces a dense pre-equilibrium matter consisting mostly of gluons and also of quarks and anti-quarks. This system takes about 1 fm/c to achieve the local thermalization and forms the quark gluon plasma. In this very early collision stage, the primary collisions between fast partons inside the colliding nuclei generate hard particles with either a large mass or a large transverse momenta $m, p_T \gg \Lambda_{QCD}, T$). Their creation involves large momentum transfer, therefore their production can be calculated in perturbative QCD using factorization theorems from the nuclear structure function.

To describe the successive stages of evolution it is necessary to know the initial condition, for the energy and spatial density. Moreover is necessary to estimate the time τ_0 at which the system reaches the equilib-

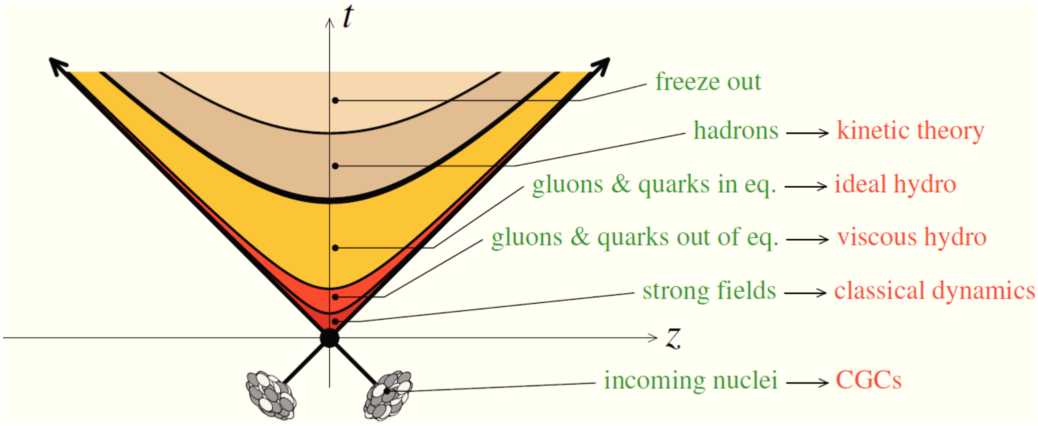

Figure 2.7: Schematic representation of the various stages of a HIC as a function of time t and the longitudinal coordinate z (the collision axis). The 'time' variable which is used in the discussion in the text is the *proper time* $\tau \equiv \sqrt{t^2 - z^2}$, which has a Lorentz–invariant meaning and is constant along the hyperbolic curves separating various stages in this figure.

rium. The initial energy density ϵ_0 can be estimated knowing the energy density released in the collision region (dE_T/dy), which is accessible if one measure the total energy of the final products collected in the detectors. The initial energy density is

$$\epsilon_0 = \frac{1}{\pi R_0^2 \tau_0} \frac{dE_T}{dy}$$

and the Bjorken estimate for RHIC is between 5 and 7 GeV/fm^3 [22], assuming an isoentropic expansion and neglecting the work needed by longitudinal expansion. Taking into account the expansion of the plasma, the previous estimation must be corrected to a value $\epsilon_0 \sim 10 \div 15\, GeV/fm^3$ at RHIC, this energy density is very greater than the critical energy density estimates by the lattice QCD. A further correction would be necessary if the expansion of the system were not iso-entropic and dissipation is taken in account. However the corrent estimated value of viscosity would lead to correction of about 10-15%.

Thermalization and expansion

Once the system has reached a kinetic equilibrium it is characterized by an energy density well above the critical energy density of the QCD phase transition ($\sim 1\, GeV fm^{-3}$); at RHIC for example, this energy density is about $10 \div 15 GeV/fm^3$, and at LHC the energy density is $\sim 2.5 \div 2.7\, \epsilon_0^{RHIC}$. Thus the system is expected to be in the quark gluon plasma phase. Actually due to the predominant presence of gluons with respect to quarks, at the beginning of this phase the system is often considered as a gluon plasma (Glasma). Driven by thermal pressure gradients the QGP expands and cools down very quickly and the partons inside the bulk rescatter elastically and inelastically. In particular, the elastic collisions lead the system towards kinetic equilibrium, while inelastic collisions cause a change in the relative abundances of the different flavours of partons, leading the system towards chemical equilibrium [23] [24]. This phase of the evolution of QGP can be described by relativistic hydrodynamics or using kinetic theory. In the more simple hydrodynamical approach, the equation of motion is obtained from the local conservations law for energy-momentum and baryon number

$$\partial_\mu T^{\mu\nu}(x) = 0 \;\; ; \;\; \partial_\mu J^\mu_B(x) = 0 \tag{2.8}$$

where $T^{\mu\nu}$ is the energy momentum tensor, that for a perfect fluid can be written in the following way

$$T^{\mu\nu}(x) = [\epsilon(x) + P(x)]u^\mu(x)u^\nu(x) - P(x)g^{\mu\nu} \tag{2.9}$$

where $u^\mu(x)$ is the four flow velocity and $g^{\mu\nu}$ is the metric tensor.
In the local rest frame

$$T^{00} = (\epsilon + P) - P = \epsilon, \qquad\qquad T^{ii} = -P$$

In order to solve the five equations (2.8) an additional equation is needed, in the form $P = P(\epsilon, \rho)$, that is the Equation Of State of the system and drives its evolution. In fact together with the EOS, the equations (2.8) form a closed system, that can be solved once the initial condition, i.e the energy density $\epsilon(x)$ and the velocity profile $u^{\mu}(x)$, have been specified. The expression for the energy momentum tensor can be modified adding terms that enable to take into account the dissipative effect present in a viscous fluid. In fact it seems that the quark gluon plasma has a low but non zero shear viscosity η/S to entropy density ratio close to the conjectured lower boundary equal to $1/4\pi$, expected for system in the infinite coupling limit.

When the energy density reaches the critical value $\epsilon_c \simeq 0.5 - 1\, GeV/fm^3$, the hadronization process take place. This argument will be widely treated in the next chapter.

After the hadronization process the system unfergoes hadronic rescatterings during the further expansion of the fireball. The collisions can be either elastic or inelastic. When the probability of inelastic collision becomes negligible, the specie of hadrons doesn't change, and the system reaches the so-called *chemical freeze-out*. Studies by mean of statistical model show that at RHIC and LHC $T_{fo}^{chem} \sim 155 - 165\, MeV$ When the mean distance between particles exceed the interaction range, there are no more collisions and there is the *kinetic freeze-out* at a temperature $T_{f-o} \sim 120 MeV$.

2.4 Principal observable probes for QGP

There are several suggestions at present to identify whether the matter produced in a high energy heavy ion collision is the Quark Gluon Plasma phase. One approach is to look for primordial remnants in the observed hadron features: discontinuities in the momentum distribution of the secondaries reflecting a first order phase transition or strangeness enhancement which is expected to be significantly larger if it arises from the QGP. Another usual suggestion is to look for signals produced at early times and are not affected by the subsequent hadronization. Possible observables of this type are thermal dileptons and thermal photons, which are emitted by the plasma and then escape. This would provide a direct signal from the QGP but the drawback is that there are many others sources of dileptons and photons that generate a very large background.

In the same context, one may also study the effect of the produced dense medium on the observed production of heavy quark bound states, like J/Ψ suppression or hard jets.

In the following a list of the principals observables of the QGP will be presented

Global observables

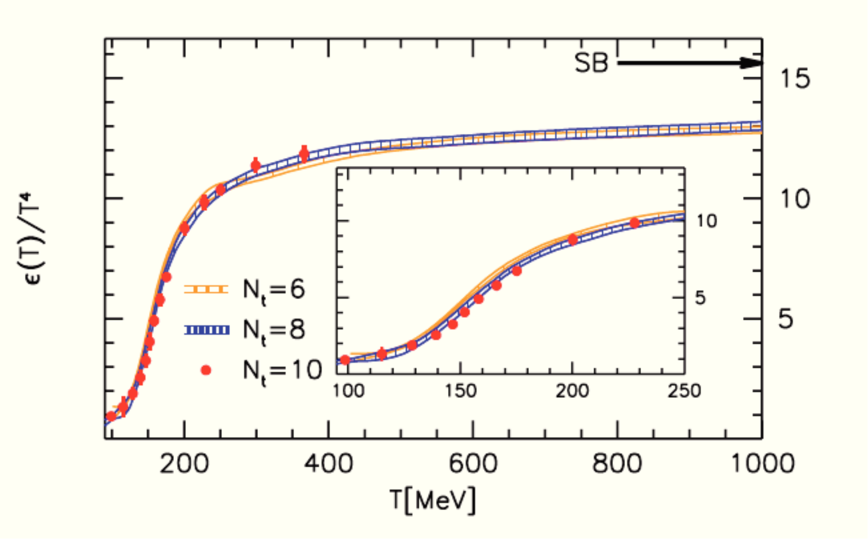

Figure 2.8: Lattice calculations of the energy density scaled by T^4 showing the transition to QGP. The hadronic matter dissolves into QGP with a finite number of degrees-of-freedom.

The aim of this group of signatures is to measure the equation of state and the thermodynamic parameters of the superdense matter. For example one wants to search for a rapid rise in the effective number of degrees of freedom, for $N_f = 2$ the hot hadron gas has only three light degrees of freedom (π^+, π^0 and π^-) neglecting the states with mass $m > T$, while the QGP has about 37 degrees of freedom (quarks and gluons). This is reflected as a rapid change in ϵ/T^4 or s/T^3 across the critical temperature, see Fig.2.8. The experimental transverse energy, dE_T/dy, the hadron multiplicity, dN/dy, and the average transverse momentum, $\langle p_T \rangle$, roughly correspond to ϵ, s and T respectively. Therefore, a plot of $\langle p_T \rangle$ as a function of dE_T/dy or dN/dy may show characteristic correlations reflecting the QCD equation of state [25]. These quantities would exhibit a discontinuity, if there were a first-order phase transition. In real heavy ion collisions, we may expect a steep, continuous rise even if the phase transition is 1st order because the system is finite and thermodynamics discontinuity are damped.

The rapidity distribution of particles dN/dy, in Fig.2.9, and transverse energy density dE_T/dy allow for the determination of temperature, en-

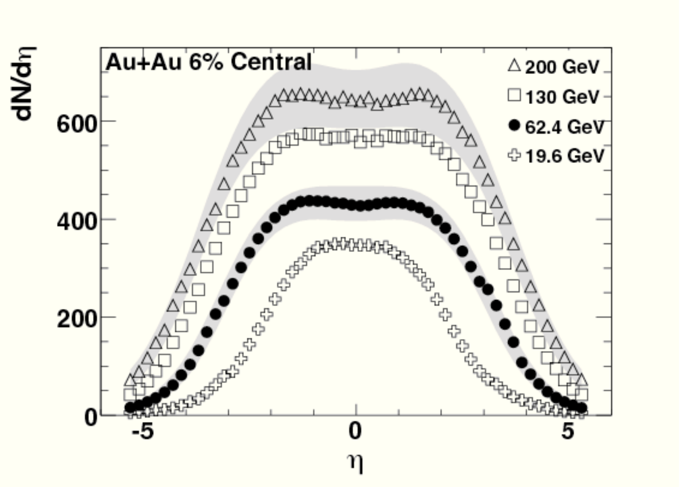

Figure 2.9: Charged particle multiplicity distributions for collisions at RHIC with four different energies as a function of pseudorapidity.

tropy and energy density of the system created in a heavy ion collision. The transverse energy density dE_T/dy is related to the energy density by the formula:

$$\epsilon = \frac{1}{\tau_f S}\frac{dE_T}{dy} \simeq \frac{3}{2}\frac{\langle m_T \rangle}{\tau_f S}\frac{dN_{ch}}{dy} \tag{2.10}$$

where $\tau_f S$ is the formation time, conventionally taken as $\tau_f S \simeq 1 fm/c$, S is the transverse overlap area of the colliding nuclei (for a central collision of two identical nuclei of radius R this is simply $S = \pi r^2$) and m_T is the mean value of the transverse mass of secondary particles, and dN_{ch}/dy is the measured density of charged particles per unit of rapidity.

Strangeness and Anti-baryon enhancement

Enhancement of strangeness and antibaryon production is a frequently discussed signal, it is due to the reduction of the threshold for production of strange hadrons from $2m_K - 2m_\pi \approx 700\, MeV$ to $2m_s \approx 300\, MeV$ and baryon-antibaryon pairs from $\approx 2GeV$ to almost zero. The strongest signal is obtained by considering strange antibaryons which combine both effects [26] [27] [28]. The enhanced strange quark production in deconfined quark-gluon plasma leads to chemical equilibrium abundances for all strange quarks. The strangeness abundance for hadronic matter in chemical equilibrium is smaller. This signal was first predicted [27] as a consequence of the interaction between partons in the QGP. It has indeed been observed at both the SPS and the RHIC energies. When the collision volume becomes larger the number of baryons increases with respect to the baseline (a pp or a $Be-Be$ collision). This is also observed at $Pb-Pb$ collisions at LHC, however the enhancement is smaller than that at lower energies as shown in Fig. 2.10.

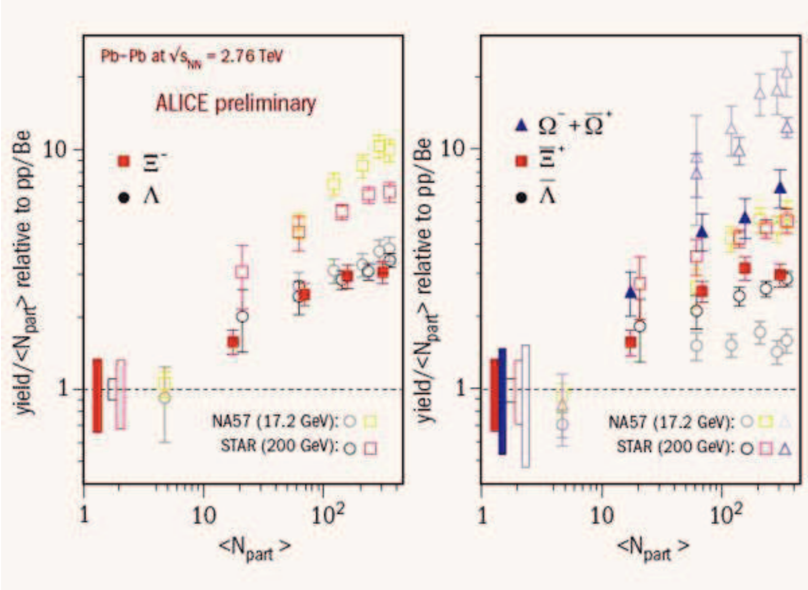

Figure 2.10: Enhancement of the multi-strange baryon yields as a function of the number of participants in *Pb-Pb* collisions at LHC compared with pp collisions, together with similar measurements at SPS (compared with pBe collisions) and RHIC.

J/Ψ suppression

J/Ψ particles are bound states formed by a charm and an anticharm quark ($c\bar{c}$). They are produced mostly by the hard scatterings in the first stage of the collision. When they are created in p+p collisions, they can freely escape from the collision region. On the other hand, the J/Ψ produced in nucleus-nucleus collisions crosses the QGP and feels screening effects in the medium. Although the J/Ψ meson is a tightly bound particle, in a quark-gluon plasma environment the charm-anticharm potential is screened, like in the analogous phenomenon called Debye screening in QED. As a consequence, the interaction between the $\bar{c}$ and c quark is strongly weakened when $r_{c\bar{c}} > \lambda_D$, with λ_D the Debye screening length. For sufficiently high density, λ_D is so small that the J/Ψ dissociates, leading to a suppression of the observed yield compared to p+p or p+nucleus collisions [29].

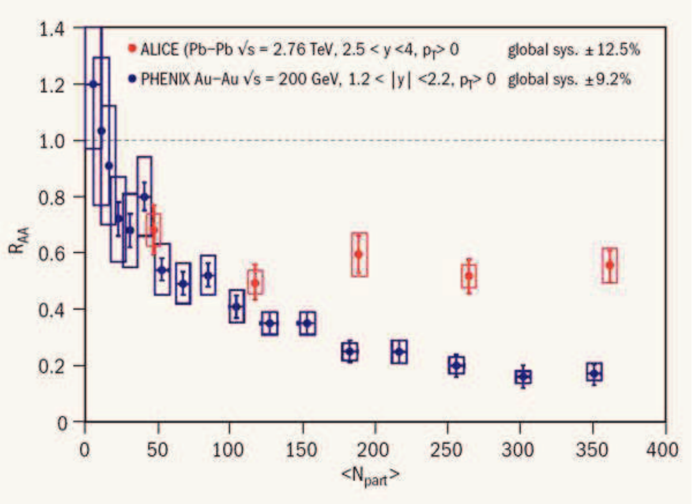

Figure 2.11: R_{AA} measurements for J/ψ at RHIC (PHENIX) and LHC (ALICE). Value under the unity reveals a suppression in the J/ψ production compared with pp collisions

But first runs at LHC gave a different result when compared with the observations from lower energies (see Fig. 2.11). While a similar suppression is observed also at LHC energies for peripheral collisions, when moving towards more head-on collisions the suppression no longer increases. Despite the higher temperatures attained at LHC, more J/ψ are produced in $Pb-Pb$ with respect to pp. The picture arises from these observations is consistent with the formation of a deconfined system that can suppress the J/ψ meson, followed by a regeneration process that ultimately give a J/ψ yield larger than that observed at lower energies.

Photons, and lepton pairs

During the evolution of a nuclear collision are created photons and dileptons that can be used to probe the QGP. The importance of this probes is due to the fact that they do not interact strongly and so there is a little possibility that they interact after their creation. Therefore these probes provide information of the phase of the evolution in which they are originated. There are many sources which can produces photons or dileptons, hence the analysis of this kind of observables is quite difficult. But very recent and upcoming data are likely to make accessible this probe sheding new light into the initial stage of the collision

Elliptic flow

In the hydrodynamic expansion following a heavy-ion collision, the matter develops a flow pattern. The flow pattern is related to the equation of state of the system through the pressure gradient, the temperature and the density. The phenomenon of this collective flow has been investigated over a wide range of energies, from tens of MeV per nucleon to the RHIC regime. To study the collective flow in experiments, it is important to determine the reaction plane, a reference plane, of the collision. In Cartesian coordinates, the $\hat{z}$ unit vector is in the beam direction. The $\hat{x}$ unit vector lies in the direction of the impact parameter vector and forms the reaction plane with the $\hat{z}$ vector. The $\hat{y}$ unit vector is normal to the reaction plane, see Figure 2.2
Particle rapidity, p_T and azimuthal angle with respect to the reaction plane can be determined from its motion. The azimuthal distribution of emitted particles in a given rapidity range can be characterized using the Fourier expansion

$$\frac{dN}{dp_T\, d\phi\, dy} = \sum_{n=0}^{\infty} 2\, v_n(p_T)\cos(n\phi) \tag{2.11}$$

where ϕ is the azimuthal angle with respect to the reaction plane.

- The v_0 coefficient describes the overall yield of particles in the given rapidity range. It is typically taken to be an overall normalization parameter allowing all the higher order coefficients to be given as a percent.

- The v_1 coefficient gives the strength of the directed flow in the reaction plane with preferred emission at $\phi = 0$ in the forward hemisphere and $\phi = \pi$ in the backward hemisphere. It is manifested by the reflection of incoming matter by the first produced regions of highly compressed nuclear matter. The magnitude of deflection probes the compressibility of the nuclear matter. It also carries information of the system at early time because the deflection takes place during the passing time of colliding nuclei. In the case of symmetric AA collisions, v_1 must be zero around midrapidity. The directed flow measured at midrapidity by RHIC is very small, of the order of 1%.

- The coefficient v_2 is called elliptic flow and can be determinated from the following formula

$$v_2(p_T, b) = \langle \cos(2\phi) \rangle = \langle \frac{p_x^2 - p_y^2}{p_x^2 + p_y^2} \rangle \tag{2.12}$$

The higher order Fourier moments can help match the simplistic Fourier expansion to the shape of the measured experimental distribution. However notice that by simmetry all odd v_n terms should be vanishing. For collisions with $\sqrt{s_{NN}} < 1.5\, GeV$ (see Appendix B), the elliptic flow corresponds to an out-of-plane squeeze-out with maximum emission at $\phi = \pi/2$ and $3\pi/2$. When $\sqrt{s_{NN}} > 1.5\, GeV$, the elliptic flow is oriented in the reaction plane with maximum emission at $\phi = 0$ and π [30]. The main reason of this pattern is the shadowing caused by the spectator that vanish at higer energies, because they quickly leave the central region of reaction. The most flow is generated from collisions that are not fully central but still have significant overlap. The shaded overlap region formed by the participants is initially an ellipsoid shaped somewhat like an almond with maximum compression along the broad flat

sides. The initial azimuthal anisotropy, with arrows indicating the direction of particle motion, is shown in Fig.(2.12). As the system expands and cools, its coordinate-space shape becomes more spherical. However, the momentum-space distributions retain the memory of the early pressure anisotropies (note that the coordinate space distributions are not directly experimentally observable). The comparison of different collision systems as a function of centrality is a good way to study the effect of the initial coordinate-space azimuthal anisotropy, measured by the eccentricity,on the observed momentum-space elliptic flow. The strongest elliptic flow effects in experiments [31] are seen for the more peripheral 45-85% collisions, roughly corresponding to $b \sim 12\, fm$, the weakest for the 0-10% most central events, corresponding to $b \sim 3\, fm$.
The eccentricity is defined as

$$\mathscr{E} = \frac{\sigma_y^2 - \sigma_x^2}{\sigma_y^2 + \sigma_x^2} \tag{2.13}$$

where σ_x and σ_y are the widths of the particle distributions in the $\hat{x}$ and $\hat{y}$ directions. In the most central collisions, $\sigma_y^2 \sim \sigma_x^2$ in a symmetric AA collision, resulting in a small eccentricity, while the eccentricity is larger in more peripheral collisions.

The observation of very large v_2 is the prominent indicator of low viscosity of the matter created in heavy-ion and collisions [32] [33]. Both hydrodynamical and parton cascade model calculations have shown that the generation of the elliptic flow saturates within the first 4-5 fm/c, and therefore such an observable is useful to study the QGP.
In Fig.(2.13) are shown the results for the elliptic flow obtained at RHIC as a function of the transverse momentum for different hadronics species compared to hydrodynamical calculations. From these figure it can be observed that in the region of low transverse momenta, $p_T \leq 2\, GeV$, the measured anisotropy is in agreement with an hydrodynamical descrip-

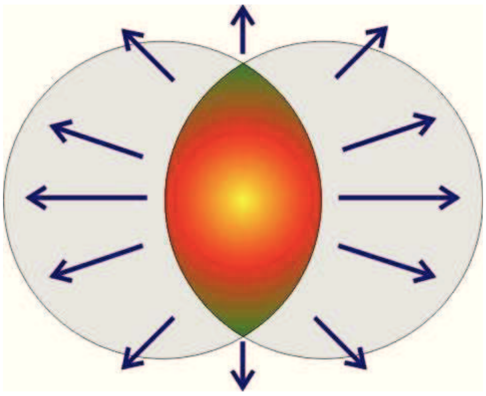

Figure 2.12: A semi-central collision of two equal size nuclei is shown in the transverse plane. The x and y unit vectors are on the page plane. The z axis (the beam axis) goes into the page. The shaded overlap region indicates the nucleon participants in the collision. The ellipsoid of hot participant matter left behind at midrapidity after the spectators have departed. The arrows indicate the direction of the expansion.

tion with negligible viscosity over entropy ratio. The failure of the hydrodynamic predictions for p_T greater than $1.5\,GeV$ indicates a breakdown of local thermal equilibrium for particles with high momenta, that is predicted by parton cascade model [34].

There is another important information that can be derived from the Fig.(2.13), i.e the different value of the elliptic flow measured for mesons and baryons. In particular these last species have a v_2 considerable larger with respect to mesons. This difference has not found an explanation in the hydrodynamical framework but can be explained by the coalescence model for hadronization. This model predicts that the v_2 of any hadron species follows the partonic flow scaled by the number n of (recombined) constituent quarks in the hadron, see Fig.(2.14) [39][40].

$$v_2^{hadron}(p_T) \approx n_q v_2^{quark}(p_T/n_q) \tag{2.14}$$

where $n_q = 2$ for mesons and $n_q = 3$ for baryons. In Fig.(2.14) is shown the quark number scaling of the elliptic flow. This scaling indicates that the flow is developed at the quark level, thus quarks are the degrees of freedom of the created matter.

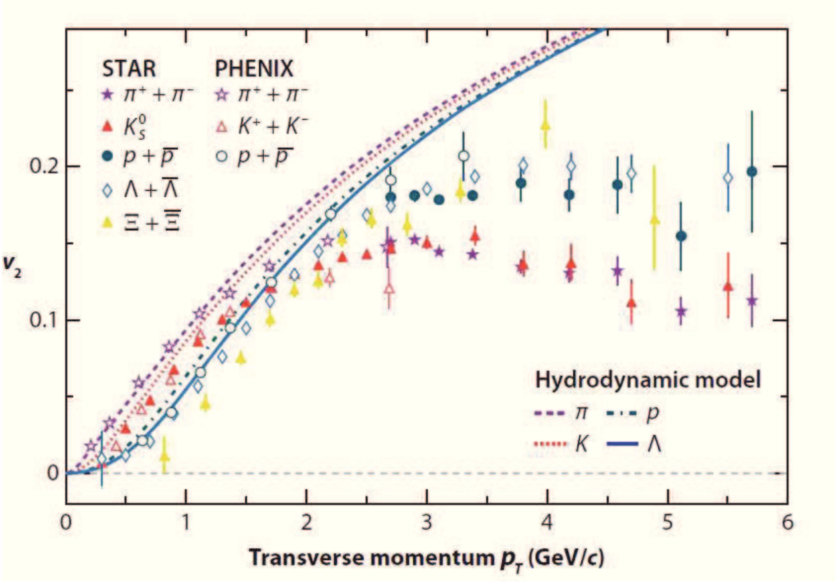

Figure 2.13: v_2 for several hadron species from a minimum-bias sample of Au + Au collisions at $\sqrt{S_{NN}} = 200GeV$ measured by the Solenoidal Tracker at the Relativistic Heavy Ion Collider (STAR) [35] and Pioneering High Energy Nuclear Interaction Experiment (PHENIX) [36] collaborations. The curves show the results from hydrodynamic model calculations [37] [38]. v_2 values also show that baryon production at intermediate p_T is enhanced in the in-plane direction, leading to larger baryon v_2. This observation is incompatible with the expectation of v_2 arising from parton energy loss.

However, at LHC, a breaking of quark number scaling has been observed, it is of the order of 20% in the peak region and is not yet clarified.

Nuclear modification factor and Jet quenching

In the first stage of a ultra-relativistic heavy ion collision are produced particles with high transverse momentum that propagate trough the plasma interacting with the bulk and losing energy. This particles can be be used to probe the QGP as proposed long ago in Ref.[41] [42] [43] [44] [45].

The production of high p_T partons can be theoretically predicted using the perturbative QCD (pQCD) frame-work thanks to the factorization

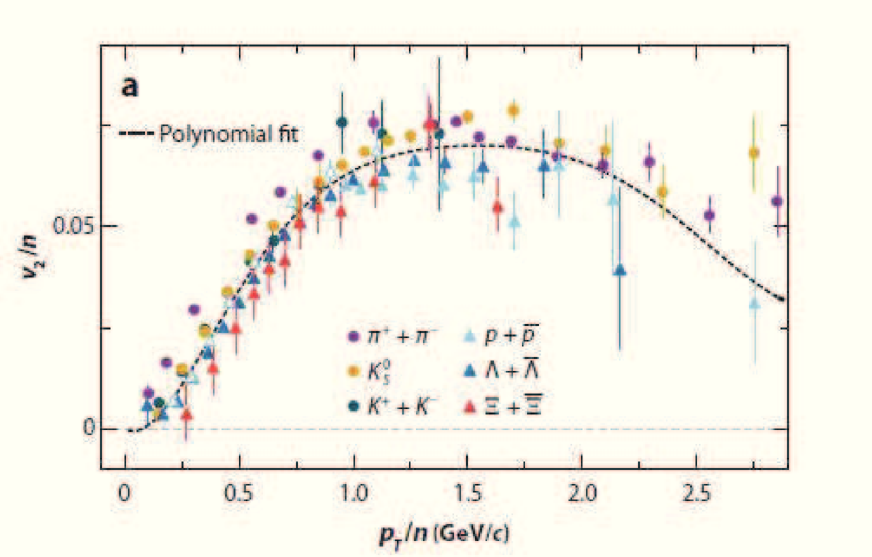

Figure 2.14: The elliptic anisotropy parameter v_2 scaled by quark number n and plotted against p_T/n.

theorem, see next chapter.

The high energy partons lose energy in the plasma through elastic scattering with the components of the bulk and also radiating gluons in a way similar to the bremsstrahlung photons emitted in QED. The main difference between the radiative energy loss in QED and in QCD, results from the fact that, due to the non-Abelian nature of QCD, the emitted gluons carries color charges and interact with the color charges that are in the medium (at variance with photons in QED). This emitted gluons travel a random walk inside the plasma causing a non-linear dependence of the energy loss on the thickness of the medium. In the evaluation of the radiative energy loss must be also considered the Landau-Pomeranchuk- Migdal effect (LPM) that takes into account the coherence effect, due to the interaction of the hard partons with more than one scattering center. At high parton energy the radiative mechanism is the main responsible for the parton energy loss. Many different approaches have been developed in order to estimate the energy loss suffered by high p_T partons in the expanding fireball created in the collisions [46]

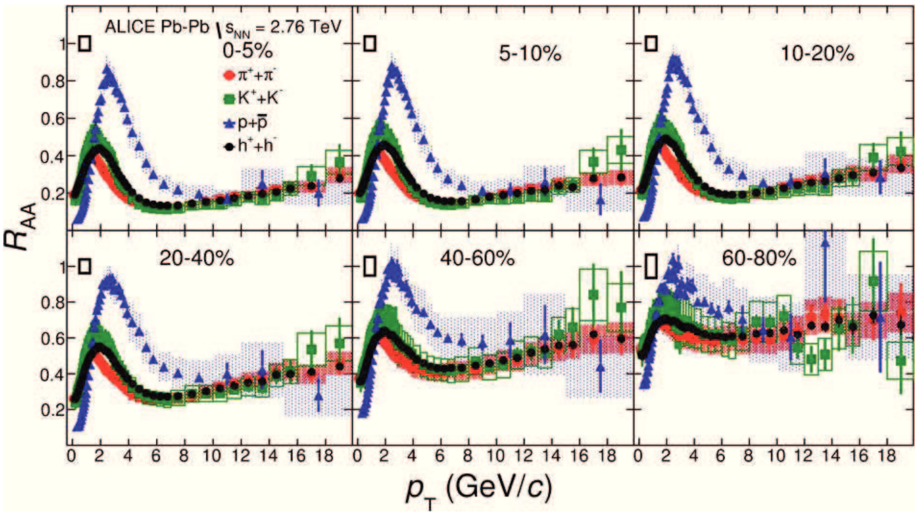

Figure 2.15: The nuclear modification factor R_{AA} measured at LHC Pb+Pb collisions at $\sqrt{s_{NN}} = 2.76 AGeV$ for charged hadrons, pions, protons and kaons at various centralities

[47] [48] [49] [50] [51] [52].

The energy loss of high p_T partons causes an attenuation or disappearance of the spray of hadrons, called jet, resulting from the fragmentation of these high partons. This phenomenon of suppression is called jet quenching and is one of the most important probe of the formation of the Quark Gluon Plasma. The suppression can be quantified by the nuclear modification factor R_{AA} that is given by the ratio between the spectrum of partons produced in ion-ion (AA) collision and that relative to proton-proton collision multiplied by the scaling factor N_{coll}

$$R_{AA}(p_T) \equiv \frac{d^2N^{AA}/dp_T d\eta}{N_{coll} \cdot d^2\sigma^{NN}/dp_T d\eta} \tag{2.15}$$

if R_{AA} is equal to one means that AA is only a superposition of pp collisions. In experiments at RHIC and LHC a very low value of R_{AA} (~ 0.2) has been measured, indicating that the medium created has a very large density. Several models associates an $R_{AA} \sim 0.2$ to initial density of $10-20\ GeV/fm^3$ in agreement with estimates coming from other observables. One of the open challenge regarding the jet quenching is to explain the difference in the suppression between the different hadron species. This is strongly related to the different energy loss experienced by quarks and gluons, but also to the inelastic collisions that change the relative abundances.

CHAPTER 3

HADRONIZATION

3.1 Introduction

In this chapter, we discuss the problem of the hadronization of the matter created in ultra-relativistic heavy ion collisions. Since no single quark or gluon are observed but only hadrons, the produced partons must due to confinement in a length scale of about $1\,fm$ before observation.

There are two different class of approaches to deal with the problem of hadronization of the QGP. One approach is based on the statistical model (see paragraph 3.3) in which the number of partons produced for each species and then spectra can be evaluated using the conservation laws (for Energy-momentum, intrinsic angular momentum, etc.).
This approach does not care about the microscopic mechanism that leads to the production of hadrons, because it assumes that whatever is the hadronization mechanism the number of hadrons and the spectra follows the kinetic and chemical equilibrium laws of statistical mechanics. The other class of approaches to deal with the hadronization instead

takes care about the miscroscopic mechanism of hadronization.
Within the microscopic approach there are two different ways in which partons can form hadrons: the fragmentation (see paragraph 3.2) and the coalescence (see paragraph 3.4).
In the first one each parton fragment into a jet of hadrons which carries a fraction of the momenta of the initial parton, while the second one consists in the recombination of two or three quarks that form respectively mesons or baryons.
The fragmentation is the dominant way to hadronize in ultra-relativistic proton-proton collisions at least at mid-rapidity.

3.2 Statistical Model

Particle production observed in heavy-ion collisions allows a systematic study of the thermal properties of the final state. In a wide energy range, from the SIS up to RHIC, the yields of produced particles have been shown to be consistent with the assumption that hadrons originate from a thermal source with a given temperature and a given baryon density. By using only two thermal parameters, a successful description of particle ratios measured in heavy-ion collisions over a wide range of center of mass energies could be made. The extracted chemical freeze-out parameters, the temperature T and the baryon chemical potential μ_B can be characterized by a constant average energy per hadron $\langle E\rangle/\langle N\rangle$. The extrapolation of this freeze-out curve towards vanishing μ_B is bounded by the critical phase transition temperature as calculated in Lattice Gauge Theory.

The equilibrium behavior of thermodynamical observables can be evaluated as an average over statistical ensembles (rather than as a time average for a particular state). The equilibrium distribution is thus

$\bar{h}/h$ Ratio		mixed Ratio	
π^+/π^-	$0.9998^{+0.0002}_{-0.0010}$	K^+/π^+	$0.180^{+0.001}_{-0.001}$
$\mathrm{K}^+/\mathrm{K}^-$	$1.002^{+0.008}_{-0.002}$	K^-/π^-	$0.179^{+0.001}_{-0.001}$
$\bar{\mathrm{p}}/\mathrm{p}$	$0.989^{+0.011}_{-0.045}$	p/π^-	$0.091^{+0.009}_{-0.007}$
$\bar{\Lambda}/\Lambda$	$0.992^{+0.009}_{-0.036}$	Λ/p	$0.473^{+0.004}_{-0.006}$
$\bar{\Xi}^+/\Xi^-$	$0.994^{+0.006}_{-0.026}$	Ξ^-/Λ	$0.160^{+0.002}_{-0.003}$
$\bar{\Omega}^+/\Omega^-$	$0.997^{+0.003}_{-0.015}$	Ω^-/Ξ^-	$0.186^{+0.008}_{-0.009}$

Table 3.1: Particle ratios in central Pb-Pb collisions at freeze-out conditions expected at the LHC: T = (170±5) MeV and $\mu_B = 1^{+4}_{-1}$ MeV.

obtained by an average over all accessible phase space.

In the analysis is used as statistical operator the Hamiltonian that lead to the full hadronic mass spectrum. In some sense this is synonymous with using the full QCD Hamiltonian. The only parameters in the statistical operator describing the grand-canonical ensemble are temperature T and baryon chemical potential μ_B. The charge chemical potential is constrained by the initial isospin asymmetry of the nuclei, whereas the strange chemical potential μ_S, depending on both T and μ_B, is determined by strangeness neutrality. Thus, any particle ratio is uniquely determined by only two parameters, T and μ_B at chemical freeze-out. The particle ratio expected at the LHC conditions are shown in Table 3.1.

The basic quantity required to compute the thermal composition of particle yields measured in heavy ion collisions is the partition function $Z(T,V)$. In the Grand Canonical ensemble,

$$Z^{GC}(T,V,\mu_Q) = Tr\left[e^{-\beta(H-\sum_i \mu_{q_i} q_i}\right] \tag{3.1}$$

where H is the Hamiltonian of the system, $q_j = (Q_j,N_j,S_j,C_j,B_j)$ are the conserved abelian charges (i.e. electric charge, baryon number, strangeness, charm and beauty) and μ_{Q_i} are the chemical potentials that guarantee that the charges q_i are conserved on the average in the whole system. Finally $\beta = 1/T$ is the inverse temperature.

In this approach, the multiplicity for each hadron species j is given by

$$\langle n_j \rangle = \frac{(2J_j+1)V}{(2\pi)^3} \int d^3p \left[e^{(\sqrt{p^2+m_j^2}+\mu\cdot q_j)/T} \pm 1 \right]^{-1} \tag{3.2}$$

where J_j and m_j are, respectively, the spin and the mass of the hadron j; the upper sign applies to bosons and the lower sign to fermions.

The light-flavoured multiplicities in Au-Au collisions at RHIC show a good agreement with the prediction of the model, as shown in Figure 3.1.

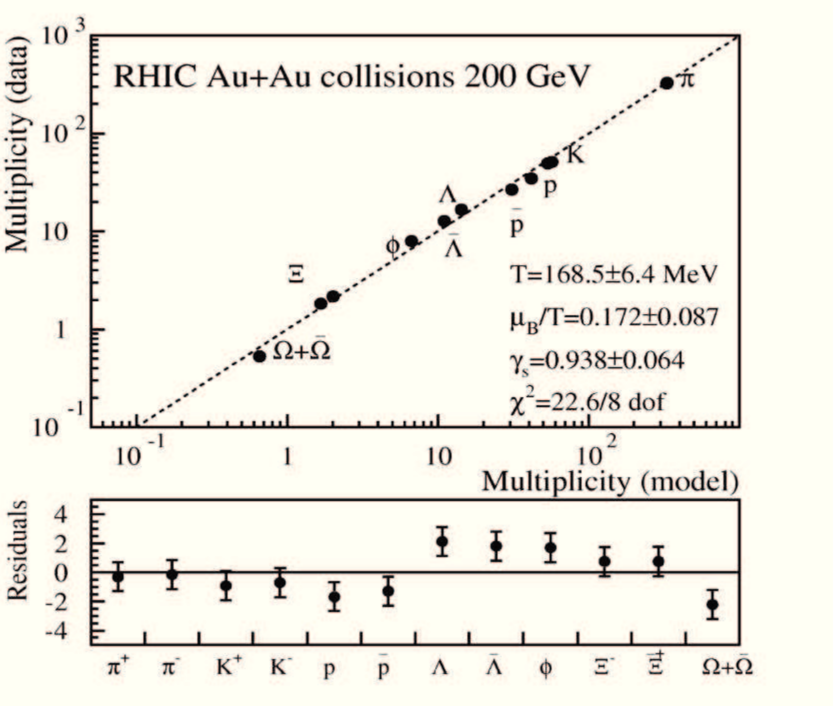

Figure 3.1: Upper panel: measured vs theoretical multiplicities of light-flavoured hadrons in Au-Au collisions at $\sqrt{s} = 200GeV$. Lower panel: fit residuals

A further interesting systematic behavior of thermal parameters has emerged from particle yields in heavy-ion collisions from SIS up to RHIC. With increasing collision energy, there is an increase of the chemical freeze-out temperature, T , and a corresponding decrease of the baryon

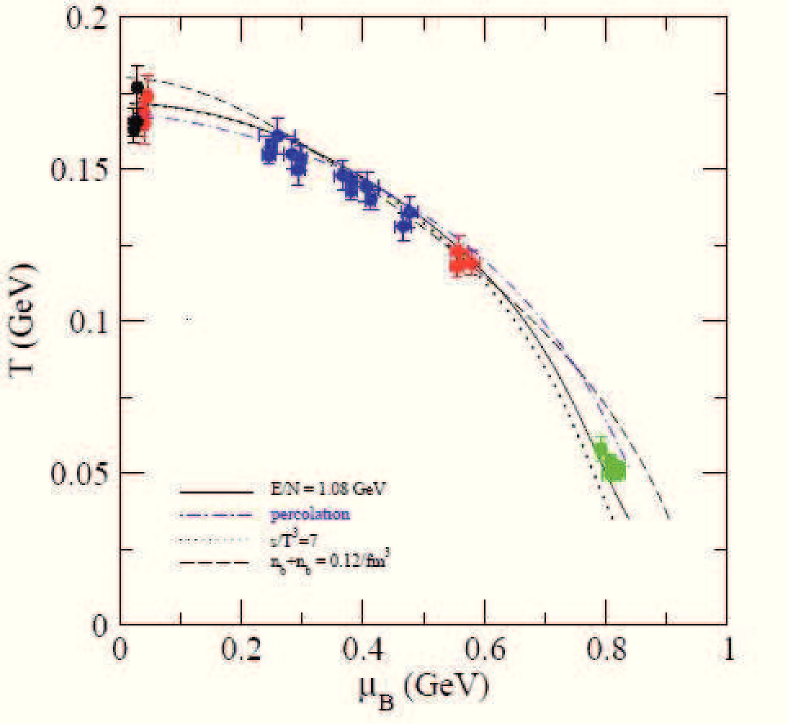

Figure 3.2: Description of chemical freeze-out by different criteria

through AGS, SPS and RHIC points, with a temperature at $\mu_B = 0$ that corresponds to the critical temperature expected for deconfinement in Lattice Gauge Theory.

There are properties of the thermal fireball at chemical freeze-out that are common to all collision energies. Such common properties provide unified chemical freeze-out conditions in heavy-ion collisions at all energies.

There are different criteria to quantify the chemical freeze-out criteria, the comparison of each of these with all known freeze-out parameter are shown in Figure 3.2.

The statistical model give, on a phenomenological level, quite satisfactory descriptions of the particle multiplicities and the relative abundances measured in heavy-ion collisions, and predict the relation between T and μ_B at freeze-out for different energies. This hadronization mechanism which stops the parton evolution and translates the fluid profile into hadron spectra can account correctly for bulk properties.

3.3 Fragmentation in pp collisions

In order to have a description of the collision it is necessary to consider both the hard scattering between partons of the different colliding hadrons, that can be treated perturbatively, and also the internal dynamics of hadrons that involve a long range interaction and therefore cannot be treated pertubatively.

This separation in two steps is called the factorization theorem, and consists in factorizing the cross section in two parts [53] [54] [55] : the short distance part which can be calculated in the framework of pQCD, and the long range part that involves hadronic wave functions, and leads to hadronization that cannot be calculate within pQCD. However these last non-perturbative quantities have important properties that allows to determine their matrix elements.

The first property is the possibility to calculate the matrix element for any momentum transfer scale Q^2, once they are known for a particular Q_0^2, towards the Doskshitzer-Gribov- Lipatov-Altarelli-Parisi (DGLAP) equations [56] [57] [58].

The second property is their universality, i.e they are independent from the specific process. This means that if they are measured in one process then they can be applied to another process, they should be the same in e^+e^-, pp, or $p\bar{p}$ collisions.

The perturbative QCD parton model is based on this factorization picture of hard process. Using this factorization picture the cross section of a typical hard process can be expressed as the convolution of the initial parton distributions, the perturbative parton scattering cross section, and the partons fragmentation function.

In Eq.(3.3) is shown schematically the cross section relative to a collision

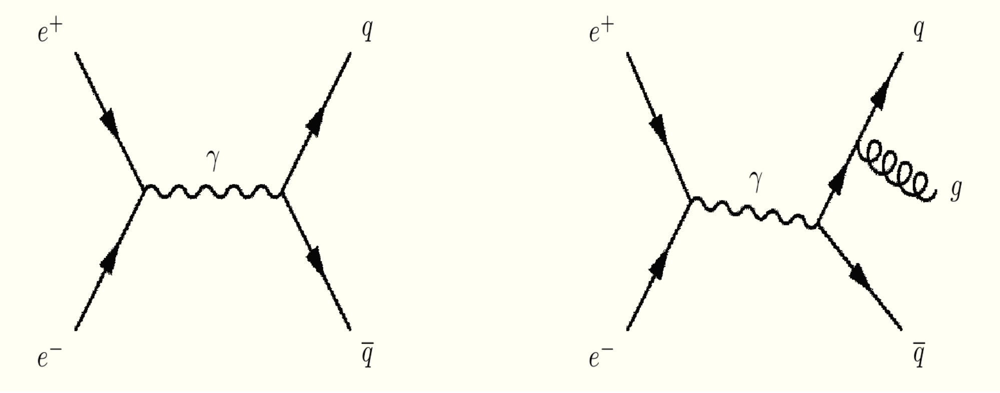

Figure 3.3: The diagrams for $e^+e^- \to q\bar{q}$ (left) and $e^+e^- \to q\bar{q}g$ (right).

between a nucleon A and a nucleon B.

$$d\sigma_{AB} = f_{a/A}(x_1,Q^2) \otimes f_{b/B}(x_2,Q^2) \otimes d\sigma_{ab}^{hard}(x_1,x_2,Q^2) \otimes D_{c\to h}(z,h) \quad (3.3)$$

where f are the parton distributions in the nuclei, that give the probability to find inside a nucleon a parton that has a fraction x of the momentum of the hadron; σ_{ab}^{hard} is the parton-parton cross section and finally D are the fragmentations functions, that give the probability that a parton c forms a hadron that carries a fraction z of the momenta of the parton ($z = p_{hadron}/p_{partons}$) [59] [60].

Fragmentation functions are not reliably calculable from first principles in QCD. However, they are observables and can be inferred experimentally and parametrizations using data mostly from $e^+ + e^-$ collisions are available from several groups [61] [62].

In order to discuss about fragmentation functions it is useful to start our discussion with collisions e^+e^- since electrons are point particles and they provide a clean initial state. Let us say that in an e^+e^- collision, a quark-antiquark pair is produced, $e^+e^- \to q\bar{q}$, as shown in Fig.3.3. After the quark is produced, it fragments into a hadron, h, which is ultimately observed in the detector.

If we identify the center-of-mass energy of the e^+e^- collision as Q, the electron beam energy, E_{beam}, is $Q/2$. The produced quark always has energy E_q equal to the beam energy of the electron or positron in the center-of-mass frame. Thus if the final-state hadron has energy E_h, the fraction of the quark energy it carries away is

$$z = \frac{E_h}{E_q} = \frac{2E_h}{Q} \tag{3.4}$$

The differential cross section for inclusive hadron production as a function of z is

$$\frac{d\sigma(e^+e- \to hX)}{dz} = \sum_q \sigma(e^+e- \to q\bar{q})[D_q^h(z) + D_{\bar{q}}^h(z)] \tag{3.5}$$

Note that a quark or antiquark of any flavour can produce the hadron. Like the parton densities, the fragmentation functions are subject to momentum and probability constraints. The sum of the energies of all produced hadrons has to add up to the energy of the parent quark,

$$\sum_h \int_0^1 zD_q^h(z)\,dz = 1 \tag{3.6}$$

The relation also holds if q is replaced by $\bar{q}$ in Eq.(3.6).
In addition, the multiplicity of h is given by the sum of probabilities for producing h from all possible parent quarks and antiquarks,

$$\sum_q \int_{z_{min}}^1 [D_q^h(z) + D_{\bar{q}}^h(z)]\,dz = n_h \tag{3.7}$$

The lower limit on the integral over z is the threshold energy for producing a hadron of mass m_h, $z_{min} = 2m_h/Q$, since the threshold energy is equal to the rest energy.

Fig.3.4 shows the KKP [62] fragmentation functions for charged pions, charged kaons and protons/antiprotons as functions of z for $Q = 3\,GeV$, a typical value for RHIC. Note that the charged pions from u and $\bar{u}$ are identical.

While production by gluons is greatest at small z, at higher z production by quarks and antiquarks soon dominates, particularly for kaons and

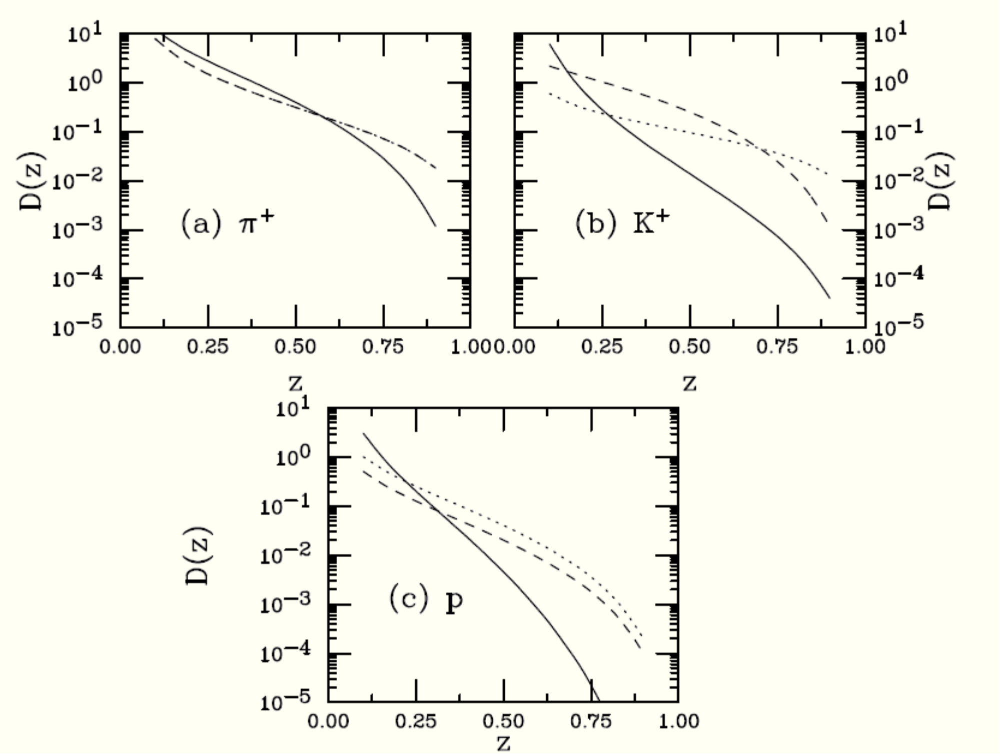

Figure 3.4: The KKP fragmentation functions [62] for (a) charged pions, (b) charged kaons and (c) protons and antiprotons as a function of z. The curves show the contribution from u quarks (dotted), $\bar{u}$ quarks (dashed) and gluons (solid) with initial momentum of 3 GeV.

protons. Thus, while gluon production may dominate parton production in hadronic collisions, production of final states by gluons may be smaller, especially in certain regions of phase space where z is large. While some changes are expected as a function of scale, the general trends do not change substantially. As we already mentioned, the fragmentation function parameterize properties intrinsic to the partons and are thus universal, regardless of the parton production mechanism. Then once the fragmentation functions are fixed in e^+e^- collisions, they can be applied to other collisions such as ep, pp and $p\bar{p}$. Thus, schematically, the production of hadron h in ep collisions as a function of z is

$$\frac{d\sigma(ep \to hX)}{dz} \propto \sum_q e_q^2 f_q^p(x) D_q^h(z) \tag{3.8}$$

where $f_q^p(x)$ is the parton distribution function for a quark q that carries a fraction x of the proton momentum. In pp collisions, the inclusive p_T distribution of produced hadron h is

$$\frac{d\sigma(pp\to hX)}{dp_T} = 2p_T \int_{\theta_{min}}^{\theta_{max}} \frac{d\theta_{cm}}{\sin\theta_{cm}} \int dx_1 \int dx_2 \\ \times f_i^p(x_1,Q^2) f_j^p(x_2,Q^2) \frac{D_q^h(z,Q^2)}{z} \frac{d\sigma_{ij}}{dt} \tag{3.9}$$

For an integral over all rapidity, $\theta_{min} = 0$ and $\theta_{max} = \pi$. The $2 \to 2$ hard scattering partonic cross sections are given by $d\sigma_{ij}/dt$.

3.4 Coalescence

Coalescence models were first suggested shortly after the theory of QCD was developed in the 1970s. These models successfully described hadron production in the very forward region of hadronic collisions [63]. The observed relative abundances of hadrons clearly deviate from expectations for fragmentation. This is known as the leading particle effect [64].

As an example, a clear asymmetry between D^- and D^+ mesons was found in fixed target experiments with π^- beams on nuclei by the Fermi National Accelerator Laboratory (FNAL) E791 collaboration [65]. The measured D^-/D^+ asymmetry goes to unity in the very forward direction, whereas fragmentation predicts that this asymmetry is very close to zero. This result can be explained by coalescence of the $\bar{c}$ from a $c\bar{c}$ pair produced in the collision with a d valence quark from the π^- beam remnants. This mechanism is enhanced compared to the $c+\bar{d}$ coalescence, which involves only a sea quark from the π^- [66].

We arrive at the important conclusion that the presence of any reservoir of partons leads to significant changes in hadronization. Vacuum fragmentation is no longer valid in this situation. The reservoir of partons in the case of the leading particle effect is the soft debris from the broken beam hadron. In heavy ion collisions it is the distribution of thermal partons.

First applications of the coalescence picture to nuclear collisions appeared in the early 1980s [67] [68], and they eventually led to the development of the algebraic coalescence rehadronization (ALCOR) model in the 1990s [69] [70] [71]. ALCOR focuses on hadron multiplicities and was successfully applied to hadron production at RHIC and to the lower energies at the Super Proton Synchrotron (SPS) at the European Laboratory for Particle Physics (CERN).

The idea is rather simple: quarks and antiquarks can combine with comoving partons to form mesons and baryons. Two or three comoving partons in the quark-gluon plasma combine their transverse momentum to produce a final-state meson or baryon with higher p_T than the partons themselves. In addition to the hard partons produced by initial interactions governed by perturbative QCD, the other partons in the medium have "soft" thermal distributions. The partons that combine can all be hard, all soft, or a mixture of the two [72]. There is thus a competition between the effects of fragmentation and coalescence. At central impact parameters, coalescence effects should be most important while, in more peripheral collisions, fragmentation should be a better description of hadronization. A schematic picture of the two effects, leading to the same p_T of the final-state hadron is shown in Fig.3.5. While fragmentation functions demand $z < 1$, reducing the parton momentum, the coalescence function, $\delta(p_{T_h} - p_{T_1} - p_{T_2})$ sums the momenta of two partons to obtain the final-state hadron momentum. For the production of a hadron with momentum P via fragmentation we need to start with a parton with momentum $P/z > P$. The fragmentation functions favor small values of z, *i.e.* the situation where the energy of the fragmenting parton is not concentrated in one hadron. On the other hand, the transverse momentum spectrum of partons is steeply falling with P_T. This

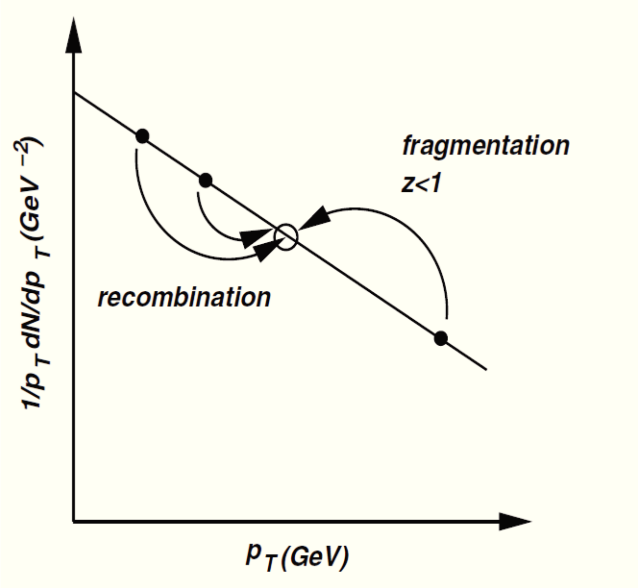

Figure 3.5: The competing effects of coalescence and fragmentation on a final-state p_T distribution [73]

makes it clear that fragmentation is a rather inefficient mechanism for the production of high P_T hadrons, since it has to overcome the limited availability of partons at even higher transverse momentum. As a result, the average $\langle z \rangle$ is larger than what is expected from the shape of the fragmentation functions.

An outgoing high energy parton is not a color singlet and will therefore have a color string attached. The breaking of the string will initiate the creation of quark-antiquark pairs until there is an entire jet of partons, which have to share the energy of the initial parton. They will finally turn into many hadrons. The creation of several hadrons from one fragmenting parton is the reason why fragmentation functions prefer small values of z.

If phase space is already filled with partons, a single parton description might not be valid anymore. Instead one would have to introduce multiple parton fragmentation functions. In the most extreme case, if partons are abundant in phase space, they might simply recombine into hadrons.

This means that a u and a $\bar{d}$ quark that are "close" to each other in phase space can bind together to form a π^+. The scale of being close will be set by the width of the pion wave function.

In this scenario the total pion momentum will be just the sum of the individual quark momenta. We immediately notice that this coalescence mechanism is very efficient for steeply falling spectra: in order to produce a 5 GeV pion we can start with two quarks having (on average) about 2.5 GeV/c transverse momentum and each being therefore far more abundant (on average) than a 10 GeV/c parton that could produce the pion via fragmentation. Of course the recombining partons must be close in phase space, *i.e.* coalescence will be suppressed if the phase space density is low.

For the coalescence of three quarks into a proton the momenta of three partons have to be added up, but only two momenta in the case of a pion.

The coalescence model is motivated by several unexpected observations, collectively known as the baryon puzzle. This term refers to measurements of baryon production in the intermediate transverse momentum region ($1.5 < p_T < 5\ GeV/c$). Both the yield and the elliptic flow of baryons exhibit strange features. In nucleon-nucleon collisions at $p_T = 3\,GeV/c$, only one baryon is produced for every three mesons (1:3), reflecting the larger mass and the requirement of a non-zero baryon number to form the baryon. In $Au+Au$ collisions at RHIC, however, baryons and mesons are created in nearly equal proportions (1:1) despite those differences.

The hadron spectra at high transverse momentum are dominantly produced from minijet partons originated from initial hard processes between colliding nucleons. The amount of energy loss of minijet partons, particularly gluons, is consistent with the scenario that they have traversed through a dense matter that consists of colored quarks and gluons. Conversions of minijet partons to high transverse momentum hadrons is usually modeled by fragmentation functions which describe how minijet partons combine with quarks and antiquarks from the vacuum to form hadrons as they separate.

In the coalescence model these minijet partons are allowed to recombinate with thermal quarks and antiquarks from the quark-gluon plasma created in the collisions to form hadrons. Using the minijet partons predicted from the perturbative QCD, this mechanism is important for production of hadrons with intermediate transverse momentum, leading to comparable antiproton and pion yields in this momentum region as observed experimentally. It further predicts that the antiproton to pion ratio would decrease as their transverse momenta become large. In this high transverse momentum region, independent fragmentations of minijet partons dominate particle production and lead to a very small antiproton to pion ratio.

In the same p_T region, hadron elliptic flows of identified particles have been measured, and except for pions they essentially follow the quark number scaling, i.e., the dependence of hadron elliptic flows on hadron transverse momentum becomes similar if both are divided by the number of constituent quarks in a hadron, i.e., two for mesons and three for baryons.

The scaling of hadron elliptic flows according to their constituent quark number has a simple explanation if hadronization goes through coalescence, in this model the anisotropy of constituent quarks at partonic level propagates at hadronic level according to

$$v_{2,M}(p_T) \approx 2\, v_{2,q}(p_T/2), \qquad\qquad v_{2,B}(p_T) \approx 3\, v_{2,q}(p_T/3) \tag{3.10}$$

in this way the coalescence mechanism tanslates the hydrodynamical behavior into higher p_T at hadronic level with the effect being larger for baryons.

The coalescence has the characteristic feature, for baryons, of a larger elliptic flow and a shift of the p_T at which the v_2 reaches the maximum value.

3.4.1 Basic Theory

Coalescence or recombination of particles is a very general process that occurs in a wide array of systems from the femtometer scale to astrophysics. In all these fields the first approach is to discard the details of the dynamical process in favor of exploiting an adiabatic approximation, in which a projection of the initial state onto the final clusterized state is considered. In the specific case of coalescence of partons, most of the work described in the literature uses an instantaneous projection of parton states onto hadron states. The expected number of hadrons h from a partonic system characterized by a density matrix ρ is given by

$$N_h = \int \frac{d^3P}{(2\pi)^3} \langle h;\mathbf{P} \,|\, \rho \,|\, h;\mathbf{P}\rangle \tag{3.11}$$

Here instantaneous means that the states are defined on a hypersurface, which is typically taken to be either at constant time, $t = constant$, or on the light cone, $t = \pm z$.

In this case information about the hadron bound state is schematically encoded in a wave function or a *Wigner function*.

This approach leads to very simple math, but it has the disadvantage in that only three components of the four-momentum are conserved in such a $2 \to 1$ or $3 \to 1$ coalescence process.

In this section, we focus on the instantaneous projection formalism.

All available models of instantaneous coalescence can be traced back to the following basic formula, which can be derived from Eq.(3.11). The number of mesons with a certain momentum $\mathbf{P}$ is [74]

$$\frac{dN_M}{d^3P} = \sum_{a,b} \int \frac{d^3R}{(2\pi)^3} \frac{d^3q\, d^3r}{(2\pi)^3} W_{ab}(\mathbf{R}-\frac{\mathbf{r}}{2}, \frac{\mathbf{P}}{2}-\mathbf{q}; \mathbf{R}+\frac{\mathbf{r}}{2}, \frac{\mathbf{P}}{2}+\mathbf{q}) \Phi_M(\mathbf{r},\mathbf{q}) \tag{3.12}$$

Here M denotes the mesons and a, b are its coalescing valence partons; W_{ab} and Φ_M are the Wigner functions of partons and of the meson respectively, while $\mathbf{P}$ and $\mathbf{R}$ are the momentum and the spatial coordinates

of the meson, and **q** and **r** are related to the relative momentum and position of the quarks. The sum runs over all possible combinations of quantum numbers of the quarks in the hadron, essentially leading to a degeneracy factor C_M.
Note that coalescence, just like its counterpart in exclusive processes, is based on the assumption of valence quark dominance, i.e., the lowest Fock states are the most important ones.
The corresponding formula for baryons containing three valence quarks can easily be given as well.
For a meson consisting of two quarks, its Wigner function is formally defined as

$$\Phi_M(\mathbf{r},\mathbf{q}) = \int d^3s \exp^{-i\mathbf{s}\cdot\mathbf{q}} \varphi_M(\mathbf{r}+\frac{\mathbf{s}}{2})\varphi^*_M(\mathbf{r}-\frac{\mathbf{s}}{2}) \tag{3.13}$$

where the two-quark meson wave function in position space ϕ_M can be represented as

$$\langle \mathbf{r}_1;\mathbf{r}_2 \mid M;\mathbf{P}\rangle = \exp^{-i\mathbf{P}\cdot(\mathbf{r}_1+\mathbf{r}_2)/2} \varphi_M(\mathbf{r}_1-\mathbf{r}_2) \tag{3.14}$$

To evaluate Eq.(3.12), expressions for the hadron wave functions and for the distribution of partons are used as input. Let us emphasize two common features of all implementations. First, the Wigner function for the multiparton distribution W_{ab} is usually approximated by its classical counterpart, the phase-space distribution of the partons on the hypersurface of hadronization. Second, Eq.(3.12) is made explicitly Lorentz covariant to account for the relativistic kinematics.

Our approach is based on the Wigner formalism [75] that allows a more direct connection with the dynamical phase-space description of heavy-ion collisions. In this formalism the transverse momentum spectrum of hadrons that consist of n (anti-) quarks is given by the overlap between the hadron wave function and the n quark phase-space distribution function $f_q(x_i,p_i)$:

$$\begin{aligned}\frac{dN_H}{d^2P_T} &= g_H \int \prod_{i=1}^{n} \frac{d^3p_i}{(2\pi)^3E_i} p_i \cdot d\sigma_i \, f_q(x_i,p_i) f_H(x_i..x_n,p_i..p_n) \\ &\qquad \delta^{(2)}\left(P_T - \sum_{i=1}^{n} p_{T,i}\right) \end{aligned} \tag{3.15}$$

where $f_H(x_i..x_n,p_i..p_n)$ is the Wigner distribution function and is the probability for n quark to form an hadron, $d\sigma$ denotes an element of a space-like hypersurface, g_H is the probability of forming a color neutral object with the spin of the hadron considered from n colored quarks (see Eq.(3.21)).

The function $f_q(x,p)$ is the covariant distribution functions of quarks (and antiquarks) in the phase space, and it is normalized to their numbers, i.e.

$$\int p \cdot d\sigma \, \frac{d^3p}{(2\pi)^3E} f_{q,\bar{q}}(x,p) = N_{q,\bar{q}} \tag{3.16}$$

In Eq.(3.15) it is already assumed that the n quark phase space distribution is approximated by the product of the single quark distribution function

$$f_q(x_i..x_n,p_i..p_n) = \prod_{i=1}^{n} f(x_i,p_i) \tag{3.17}$$

and therefore no quark-quark correlations are included.

As light hadrons wave function we have used a sphere in both space and momentum, with radii Δ_r and Δ_p, respectively, which in the Wigner formalism are related by $\Delta_r \cdot \Delta_p = 1$. The multidimesional integral Eq.(3.15) is evaluated in the full 6D phase space by the Monte Carlo method via test particle method.

In the case of meson we have that the number of particle formed from coalescence of quark and antiquarks can be written as

$$\begin{aligned} N_M &= g_M \int p_1 \cdot d\sigma_1 \, p_2 \cdot d\sigma_2 \, \frac{d^3p_1}{(2\pi)^3E_1} \frac{d^3p_2}{(2\pi)^3E_2} \\ &\times \; f_q(x_1;p_1) f_{\bar{q}}(x_2;p_2) f_M(x_1,x_2;p_1,p_2) \end{aligned} \tag{3.18}$$

g_M is the statistical factor for forming a colorless meson from spin 1/2 coloured quark and antiquark. For mesons considered here. i.e. π, ρ, K and K^*, the statistical factors are $g_\pi = g_K = 1/36$ and $g_\rho = g_{K^*} = 1/12$ The function $f_M(x_1,x_2;p_1,p_2)$ in Eq.(3.18) is the Wigner function and as already said is the probability for a quark and an antiquark to form a meson and it is linked to the meson wave function by Eq.(3.13). It describes the dynamic process of converting a quark and an antiquark to a bound state meson in the presence of a partonic matter. It depends on the overlap of the quark and antiquark wave functions with the wave function of the meson. Neglecting the off-shell effects and taking the wave functions of quark and antiquark to be plane waves, the coalescence probability function is then simply the covariant meson Wigner distribution function.

We take it to have a uniform distribution

$$\begin{aligned} f_M(x_1,x_2;p_1,p_2) &= \frac{9\pi}{2(\Delta_x\Delta_p)^3}\,\Theta(\Delta_x^2-(x_1-x_2)^2) \\ &\times\ \Theta(\Delta_p^2-(p_1-p_2)^2+(m_1-m_2)^2) \end{aligned} \tag{3.19}$$

where Δ_x and Δ_p are the covariant spatial and momentum coalescence radii. The factors before theta functions are introduced to obtain the correct normalization for the meson Wigner function in the nonrelativistic limit, i.e. $\int d^3x\, d^3p\, f_\pi(x,p) = (2\pi)^3$. Here we use $\hbar = c = 1$. For ultrarelativistic heavy ion collisions at RHIC, it is convenient to introduce rapidities variables y and η in the momentum and the coordinate space (see Appendix C).

$$y = \frac{1}{2}\ln\frac{E+p_z}{E-p_z}, \qquad \eta = \frac{1}{2}\ln\frac{t+z}{t-z}$$

In Eq.(3.18) the momentum volume element and the spatial volume elements are given by

$$\frac{d^3\mathbf{p}}{E} = dy d^2\mathbf{p}_T, \tag{3.20}$$

$$p \cdot d\sigma = \tau m_T \cosh(y-\eta)\, d\eta\, d^2\mathbf{r}_T \tag{3.21}$$

if a hypersurface of constant longitudinal proper times is adopted.

From Eq.(3.16), (3.20), (3.21), the quark and antiquark phase space distribution function is given by

$$f_{q,\bar{q}}(x,p) = \frac{(2\pi)^3}{\tau m_T \cosh(y-\eta)} \frac{dN_{q,\bar{q}}}{d\eta d^2\mathbf{r}_T dy d^2\mathbf{p}_T} \tag{3.22}$$

We substitute in Eq.(3.18) the space-momentum volume and the distributions calculated in Eq.(3.20), (3.21) and (3.22). Then inserting the identity $1 = \int d^2p_T \delta^{(2)}(p_T - p_{1T} - p_{2T})$, and differentiating both sides of the equation respect to p_T we obtain

$$\begin{aligned} \frac{dN_M}{d^2p_T} &= g_M \int d\eta_1\, d^2\mathbf{r}_{1T} d\eta_2\, d^2\mathbf{r}_{2T} dy_1 d^2\mathbf{p}_{1T} dy_2 d^2\mathbf{p}_{2T} \\ &\times \frac{dN_q}{d\eta_1 d^2\mathbf{r}_{1T} dy_1 d^2\mathbf{p}_{1T}} \frac{dN_{\bar{q}}}{d\eta_2 d^2\mathbf{r}_{2T} dy_2 d^2\mathbf{p}_{2T}} \\ &\times f_M(x_1,x_2;p_1,p_2)\delta^{(2)}(p_T - p_{1T} - p_{2T}) \end{aligned} \tag{3.23}$$

For central rapidities in relativistic heavy ion collisions (see Appendix C) is satisfied the Bjorken correlation for rapidity and pseudorapidity, i.e $\eta = y$.

The quark and antiquark phase space distribution functions in the rapidity range Δ_y can then be expressed as

$$\frac{dN_{q,\bar{q}}}{d\eta d^2\mathbf{r}_T dy d^2\mathbf{p}_T} = \frac{\delta(\eta - y)}{\Delta y} \frac{dN_{q,\bar{q}}}{d^2\mathbf{r}_T d^2\mathbf{p}_T}\Bigg|_{|y|\leq\Delta y/2} \tag{3.24}$$

In our calculation we will consider $-0.5 \leq y \leq 0.5$ and so $\Delta y = 1$. This is the rapidity interval at which the detectors are usually put in the experiments.

This leads to the following meson transverse momentum spectrum from coalescence of quarks and antiquarks

$$\begin{aligned}\frac{dN_M}{d^2p_T} &= \frac{g_M}{(\Delta y)^2}\int d^2r_{1T}\,d^2p_{1T}\,d^2r_{2T}\,d^2p_{2T} \\ &\times \left.\frac{dN_q}{d^2r_{1T}\,d^2p_{1T}}\right|_{|y_1|\le\Delta y/2} \left.\frac{dN_q}{d^2r_{2T}\,d^2p_{2T}}\right|_{|y_2|\le\Delta y/2} \\ &\times \int d\eta_1\,dy_1\,d\eta_2\,dy_2\,\delta(\eta_1-y_1)\delta(\eta_2-y_2) \\ &\times F_M(x_1,x_2;p_1,p_2)\delta^{(2)}(p_T-p_{1T}-p_{2T}) \qquad (3.25)\end{aligned}$$

To generalize the results to formation of baryons and antibaryons from the parton distribution functions, we take the baryon coalescence probability function as [75]

$$\begin{aligned}F_B(x_1,x_2,x_3;p_1,p_2,p_3) &= \frac{9\pi}{2\Delta_x^3\Delta_p^3}\,\Theta\left(\Delta_x^2-\frac{1}{2}(x_1-x_2)^2\right) \\ &\times \Theta\left(\Delta_p^2-\frac{1}{2}(p_1-p_2)^2\right) \\ &\times \frac{9\pi}{2\Delta_x^3\Delta_p^3}\,\Theta\left(\Delta_x^2-\frac{1}{6}(x_1+x_2-2x_3)^2\right) \\ &\times \Theta\left(\Delta_p^2-\frac{1}{6}\left[(p_1+p_2-2p_3)^2-(m_1+m_2-2m_3)^2\right]\right) \\ &\qquad (3.26)\end{aligned}$$

where we have taken for simplicity the same space and momentum coalescence radii for the relative Jacobi coordinates among three quarks. For boost-invariant dynamics with Bjorken spatial and momentum rapidities correlation, we obtain following baryon transverse momentum spectrum from coalescence

$$\begin{aligned}\frac{dN_B}{d^2p_T} &= \frac{g_B}{(\Delta y)^3}\int \prod_{i=1}^{3} d^2r_{iT}\,d^2p_{iT}\,\left.\frac{dN_q}{d^2r_{iT}\,d^2p_{iT}}\right|_{|y_i|\le\Delta y/2} \\ &\times \int \prod_{i=1}^{3} d\eta_i\,dy_i\,\delta(\eta_i-y_i)\,F_B(x_1,x_2,x_3;p_1,p_2,p_3) \\ &\times \delta^{(2)}\left(p_T-\sum_{i=1}^{3}p_{iT}\right) \qquad (3.27)\end{aligned}$$

In the above, g_B is the statistical factor for formation of a baryon from three quarks. For baryons and antibaryons considered in present study, i.e., p, Δ, $\bar{p}$ and $\bar{\Delta}$, the statistical factors are $g_p = g_{\bar{p}} = 1/108$ and $g_\Delta = g_{\bar{\Delta}} = 1/54$. The Eq.(3.27) can also be used for antibaryons by replacing quark momentum spectra by the momentum spectra of antiquarks.

3.4.2 Monte-Carlo Method

The multidimensional integrals in the coalescence formula, given by Eqs.(3.25) and (3.27) are evaluated by the Monte-Carlo method via test particles. Specifically, we introduce a large number of test partons with uniform momentum distribution. To take into account the large difference between numbers of partons at different momenta we associate different probability to each parton and such probability is proportional to the parton momentum distribution, e.g., dN_q/d^2p_T for quarks, with the proportional constant determined by requiring that the sum of all parton probabilities is equal to the parton number. With test partons, the coalescence formulas, Eqs.(3.25) and (3.27), can be rewritten as

$$\begin{aligned} \frac{dN_M}{d^2p_T} &= g_M \sum_{i,j} P_q(i) P_{\bar{q}}(j) \delta^{(2)}(p_T - p_{iT} - p_{jT}) \\ &\times f_M(x_i, x_j; p_i, p_j). \end{aligned} \tag{3.28}$$

and

$$\begin{aligned} \frac{dN_B}{d^2p_T} &= g_B \sum_{i \neq j \neq k} P_q(i) P_q(j) P_q(k) \\ &\times \delta^{(2)}(p_T - p_{iT} - p_{jT} - p_{jT}) \\ &\times f_M(x_i, x_j, x_k; p_i, p_j, p_k). \end{aligned} \tag{3.29}$$

$P_q(i)$ and $P_{\bar{q}}(j)$ are probabilities carried by i-th test quark and j-th test antiquark. The Monte-Carlo method introduced here allows us to treat the coalescence of low momentum partons on the same footing as that of high momentum ones. We find that despite a decrease of eight orders-of-magnitude in real particle spectra, about equal numbers of test hadrons are formed at all momenta.

CHAPTER 4

PARTICLE SPECTRA AT RHIC AND LHC

In this chapter are shown calculations based on the coalescence plus fragmentation hadronization approach as described in the previous chapter, and the results obtained are compared with the experimental data at RHIC and at LHC.
We have evaluated the coalescence integral for the main produced particles (π, K, p, $\bar{p}$, Λ, ϕ) using the method described in Eq.(3.28) and Eq.(3.29)
In order to reproduce the spectra of such particle the contribution coming from the decay of some resonances (ρ, Δ, $\bar{\Delta}$, K^*, Σ) has been added, higher state resonances have not been included because they would give their main contribution to the yield at low transverse momentum $p_T \lesssim 1\,GeV$ which is not the focus of our study.
The approach used to describe hadron production in uRHIC's is based on a fireball where the bulk of the particles is a thermalized system of gluons and u, d, s quarks and antiquarks at the temperature $T_c = 165\,MeV$ which is about the temperature for the cross-over transition in the realistic lattice QCD calculation.

4.1 Parton Distribution and Fireball

Numerically we solve the coalescence integrals (for pions, protons and kaons) by using the Monte-Carlo method in which we assume a probability for each test-particle, as described in the paragraph 3.4.2.
The main features of our model can be sketched as follows:
Test-particles are spatial distributed inside a cylindrical fireball. The distribution is uniform on the plane transverse to beam direction. The z-coordinate is assigned by $z = \tau \sinh y$, where the rapidity y is uniform in the interval $[-0.5, 0.5]$ ($\eta \simeq y$ in the Bjorken approximation).
Then momentum coordinates are assigned. The module is randomly extracted in the range from zero to a maximum momentum value. The azimuthal angle (ϕ) distribution is determined by the elliptic flow and the higher order momentum anisotropy v_n. In this way the quark transverse momentum distribution is given by

$$\frac{dN_q}{d^2p_T} = \frac{dN_q}{p_T dp_T d\phi} = \frac{dN_q}{p_T dp_T}\left[1 + 2\sum_{n=1}^{n_{max}} v_n(p_T)\cos(n\phi)\right]. \tag{4.1}$$

The partons are boosted to take into account for the quark-gluon plasma collective flow. We assume for partons a velocity with the following radial profile $\beta_T = \beta_{max}\frac{r}{R}$, where R is the transverse radius of the fireball and β_{max} is the maximum collective flow velocity of the quark-gluon plasma.
In the following subsections will be described the parton distributions used as input for our coalescence model and the shape of the fireball, that provides the spatial limits of the coalescence integral.

4.1.1 Thermal Distribution

For partons in the quark-gluon plasma we take a thermal distribution for transverse momenta up to $p_0 = 2-3\,GeV$. Therefore for light quarks and antiquarks transverse momentum spectra are given by

$$\frac{dNq,\bar{q}}{d^2r_T\,d^2p_T} = \frac{g_{q,\bar{q}}\tau m_T}{(2\pi)^3}\exp\left(-\frac{\gamma_T(m_T - p_T\cdot\beta_T \mp \mu_q)}{T}\right) \tag{4.2}$$

where $g_q = g_{\bar{q}} = 6$ are the spin-color degeneracy of light quarks and antiquarks, and the minus and plus signs are for quarks and antiquarks, respectively. The slope parameter T, as said before, is $T = 165\,MeV$. Masses of light quarks and antiquarks are $m_{u,d,\bar{u},\bar{d}} = 330\,MeV$ and $m_{s,\bar{s}} = 450\,GeV$, similar to the masses of constituent quarks. The quark chemical potential μ_q used has a value such that light antiquark to quark ratio leads to the antiproton to proton ratio observed at midrapidity in heavy ion collisions experiments, which means $\mu_q = 10MeV$ at RHIC while at LHC we have approximated μ_q to zero. For gluons the spin-color degeneracy is $g_g = 16$, for the mass we take it to be similar to that of light quarks in order to take into account non-perturbative effects in the quark-gluon plasma. This implies a number of quarks per unit of rapidity within the fireball at RHIC is $dN/dy_{u,d} \sim 230$, $dN/dy_{\bar{u},\bar{d}} \sim 210$ and$dN/dy_{s,\bar{s}} \sim 150$, while at LHC there are $dN/dy_{u,\bar{u},d,\bar{d}} \sim 530$ and $dN/dy_{s,\bar{s}} \sim 360$.

4.1.2 Minijet Distribution

Partons at high transverse momenta (greater than $p_0 = 2-3\,GeV$) are mainly from the minijets produced in initial hard collisions among nucleons. The transverse momentum distribution of minijet partons in the midrapidity can be obtained from an improved perturbative QCD calculation [76]. We have considered the initial p_T distribution according to the pQCD and the thickness function of the Glauber model to go from pp collisions to AA ones.Then we have quenched the spectra to have a nuclear suppression factor $R_{AA}(p_T)$ as observed experimentally up to $p_T \approx 10GeV$ for pions. These spectra can be parametrized at RHIC as

$$\frac{dN_{jet}}{d^2p_T} = A\left(\frac{B}{B+p_T}\right)^n \tag{4.3}$$

the parametrization at LHC is

$$\frac{dN_{jet}}{d^2p_T} = \frac{A_1}{\left[1+\left(\frac{p_T}{A_2}\right)^2\right]^{A_3}} + \frac{A_4}{\left[1+\left(\frac{p_T}{A_5}\right)^2\right]^{A_6}} \tag{4.4}$$

with the values given in the Tables (4.1), (4.2)

	A[1/GeV^2]	B[GeV]	n
g	$3.2\cdot10^4$	0.5	7.1
u,d	$9.8\cdot10^3$	0.5	6.8
$\bar{u},\bar{d}$	$1.9\cdot10^4$	0.5	7.5
s	$6.5\cdot10^3$	0.5	7.4
$\bar{s}$	$8.0\cdot10^3$	0.5	7.6

Table 4.1: Parameters for minijet parton distributions given in Eq.(4.3) at midrapidity from Au+Au at $\sqrt{s} = 200\,GeV$

	A_1	A_2	A_3	A_4	A_5	A_6
g	23.46	4.84	8.08	2.78	2.79	2.31
quark	24.68	5.11	8.01	0.55	5.65	2.56

Table 4.2: Parameters for minijet parton distributions given in Eq.(4.4) at midrapidity from Pb-Pb at $\sqrt{s} = 2.7\,TeV$

We note that the separation into a thermal spectrum at $p < p_0$ and a power law spectrum from the hard parton process at higher p_T is merely a first-order approximation. In fact, the parton radiating in the QGP medium creates a parton shower that can lead to a coalescence process or an in-medium modification of the fragmentation function that is not accounted for in our approach. One can expect this to be particularly relevant in the region of p_T around $2-3\,GeV$ at parton level that means a $p_T \approx 5\,GeV$ in the hadronic spectra.

In the next chapter, we will discuss the extension of coalescence plus fragmentation model coupling it to transport simulation which naturally supply parton distribution function from the thermalized region ($p_T \sim T$) up to high $p_T \gg \Lambda_{QCD}, T$.
Our present work based on a simplified underlying parton distribution allows one indeed to spot, especially for baryons, the importance of considering a more realistic gluon radiation and splitting in the intermediate p_T region. In fact, we will see that in our approach we find a systematic lack of yield in such a p_T region. This aspect is currently under investigation also by other groups [77]

4.1.3 Fireball Parameters

The energy density of Quark Gluon Plasma fireball is related to the charged particle multiplicities and the transverse energy of particles. The volume $V = \pi R^2 \tau$(in one unit of rapidity) and the radial flow β_{max}, are constrained imposing the total multiplicity dN/dy and the total transverse energy dE_T/dy to be equal to the experimental data, and they could be in general considered as parameters evaluated accordingly to the typical value of lifetime of the QGP and, assuming a constant acceleration, we connect the radial expansion with the radial flow $R_\perp = R_0 + 0.5\beta_{max}\tau$. The charged particles multiplicity per unit of rapidity and the transverse energy at RHIC and at LHC are

$$\begin{aligned} \frac{dN_{ch}}{dy} &\simeq 680, \qquad \frac{dE_T}{dy} \simeq 760\, GeV \qquad \text{(RHIC)} \\ \frac{dN_{ch}}{dy} &\simeq 1800, \qquad \frac{dE_T}{dy} \simeq 2200\, GeV \qquad \text{(LHC)} \end{aligned} \tag{4.5}$$

standard fireball modelling lead to estimate the relation between the τ_0 at LHC and RHIC that is $\tau_0^{LHC} \sim 2 \cdot \tau_0^{RHIC}$. Coupling this to a radial uniform expansion to values of β_{max}, $R_\perp$ and τ as shown in Tab.(4.3), in quite good agreement also with simulations in hydrodynamical or kinetic transport approaches. Such values correspond in one unity of rapidity to a volume of $V \sim 1100 fm^3$ at RHIC, while at LHC corresponds to $V \sim 2500 fm^3$, which means an increase of a bit more than a factor of two in agreement with the estimate from pion HBT interferometry.

	$R_\perp$	τ	β_{max}
RHIC	8.7 fm	4.5 fm/c	0.37
LHC	10.2 fm	7.8 fm/c	0.60

Table 4.3: Parameters for radial flow and fireball dimension at RHIC and LHC

4.2 Spectra and ratio of hadrons at RHIC

We start with comparing the results obtained using the coalescence model with the spectra of pions, protons,antiprotons, kaons and Lambdas at RHIC in Au+Au collisions at $\sqrt{s} = 200\, GeV$. We consider collisions in the class of centrality 0-10%. As already seen in paragraph 3.4.1, the main parameters of our model are the widths of Wigner function. Here for mesons we choose $\Delta_p = 0.187\, GeV$ as momentum coalescence radius. Instead in the case of baryons we use a momentum coalescence radius $\Delta_p = 0.355\, GeV$. To include the important contribution to hadron production that is given by the fragmentation process we use the Kniehl, Kramer and Pötter fragmentation function (KKP) [62], fundamental to reproduce measured high transverse momentum spectrum.

Are also considered contribution from resonances (shown in Tab.(4.4)) which has allowed to improve the description of the spectra especially at low p_T, but the presence of resonance decay does not affect significantly the intermediate p_T region and, consequently, the baryon/meson ration around the peak.

In Fig.4.1, we show the transverse momentum spectrum of pions. The data from PHENIX experiment for charged pion are shown by cir-

$\pi(I=1,J=0)$	k^*	$(I=1,J=\frac{1}{2})$	$\longrightarrow k\pi$
	ρ	$(I=1,J=1)$	$\longrightarrow \pi\pi$
	Δ	$(I=\frac{3}{2},J=\frac{3}{2})$	$\longrightarrow N\pi$
$p(I=\frac{1}{2},J=\frac{1}{2})$	Δ	$(I=\frac{3}{2},J=\frac{3}{2})$	$\longrightarrow N\pi$
$k^{\pm}(I=0,J=\frac{1}{2})$	k^*	$(I=1,J=\frac{1}{2})$	$\longrightarrow k\pi$
$\Lambda(I=0,\ J=\frac{1}{2})$	$\Sigma_0(1193)$	$(I=1,J=\frac{1}{2})$	$\longrightarrow \Lambda\gamma$
	$\Lambda(1405)$	$(I=0,J=\frac{1}{2})$	$\longrightarrow \Sigma\pi$
	$\Sigma(1385)$	$(I=1,J=\frac{3}{2})$	$\longrightarrow \Lambda\pi\ B.R.=88\%$
			$\longrightarrow \Sigma\pi\ B.R.=11.7\%$

Table 4.4: Contribution from resonances decay channel to particle spectra

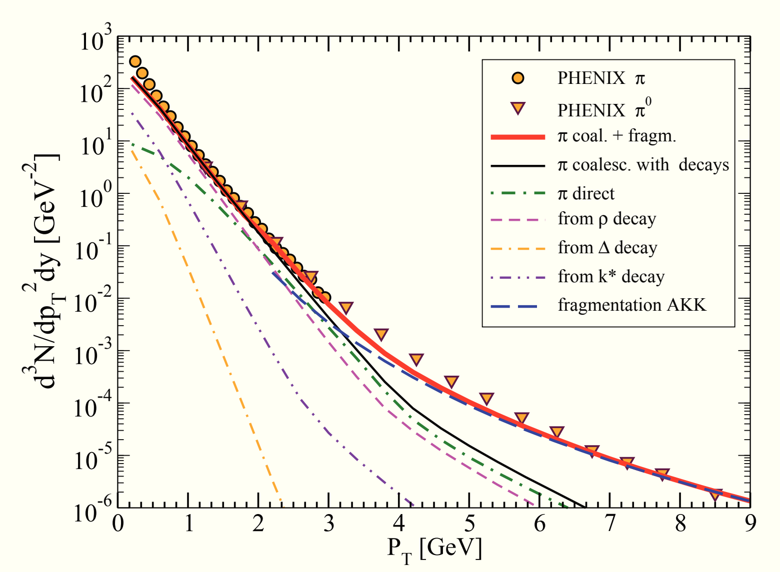

Figure 4.1: Pion transverse momentum spectrum at RHIC in Au+Au collisions at $\sqrt{s} = 200\,GeV$. Pion production from coalescence (dashed line). Pion from minijet fragmentation (dot-dashed line) . Sum of both hadronization processes (red solid line). Experimental data from PHENIX [78] [79].

cles [78] and for π^0 are shown by triangles [79]. The black solid curve is the spectrum formed from parton coalescence, including the pions from resonances. Pions from fragmentations of minijet partons are shown by the dashed blue curve. The solid red curve is the sum of coalescence and fragmentation.

We can also see the contribution for the decay into pions coming from resonances, which shows that contribution from $\rho \to \pi\pi$, dashed magenta line, dominates up to about $p_T \sim 3\,GeV$ which is about the region where anyway the fragmentation is starting to take over. The contribution from K^* (dashed double-dotted violet line) and Δ (double-dashed dot orange line) are instead quite less relevant and only contribute to some little improvement of the description at very low p_T.

Of course for the pions it is known more or less all the hadrons contribute to the feed-down but in the region we are interested in the resonances included are sufficient to have a good description of the pion spectra at $p_T \geq 1 GeV$.

Instead, at high transverse momenta the main contribution is that of fragmentation of quenched minijets. The two different type of hadroniza-

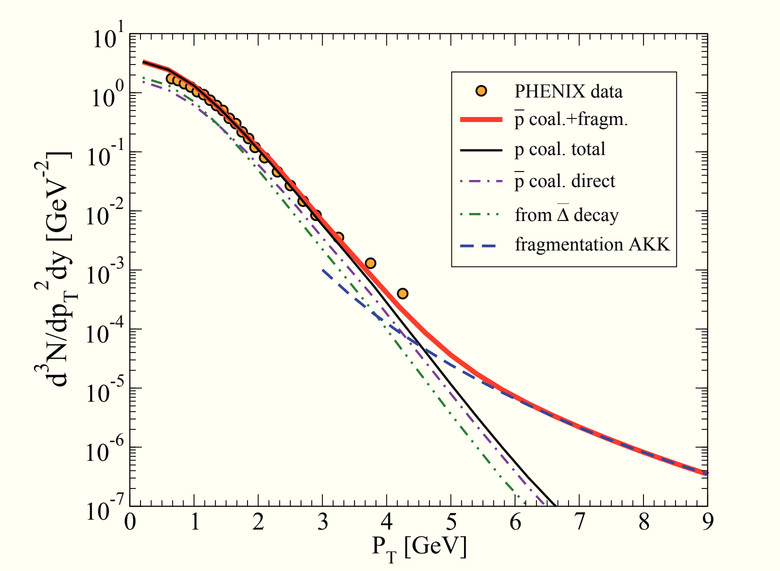

Figure 4.2: Antiproton transverse momentum spectrum at RHIC in Au+Au collisions at $\sqrt{s} = 200\,AGeV$, $0-10\%$ centrality. Antiproton production from coalescence thin solid line. Direct antiproton are shown by the violet dash-dotted line; from Δ decay are the dash double-dotted line. Antiproton from minijet fragmentation are the dashed line. Sum of both hadronization processes shown by thick solid line. Experimental data from PHENIX [78].

tion become comparable in the region near $p_T \simeq 3.5\,GeV$. We observe that as the momentum decreases coalescence become determining to reproduce data and for $p_T \approx 2\,GeV$ the spectrum of pions coming only from fragmentation of minijets is almost one order of magnitude lower than spectrum experimentally observed. For high momenta instead the impact of coalescence becomes negligible and fragmentation alone can explain the experimental data.

In Fig.4.2 we show the anti-proton transverse momentum spectrum at RHIC including coalescence and fragmentation by thick solid red line together with the available experimental data (circles) from Ref. [78]. Again the description appears to be quite good; we show also the relative contribution from coalescence and fragmentation by thin solid black line and by dashed blue line respectively. We notice that for anti-protons the two mechanism become comparable at $p_T \simeq 5\,GeV$ which means that

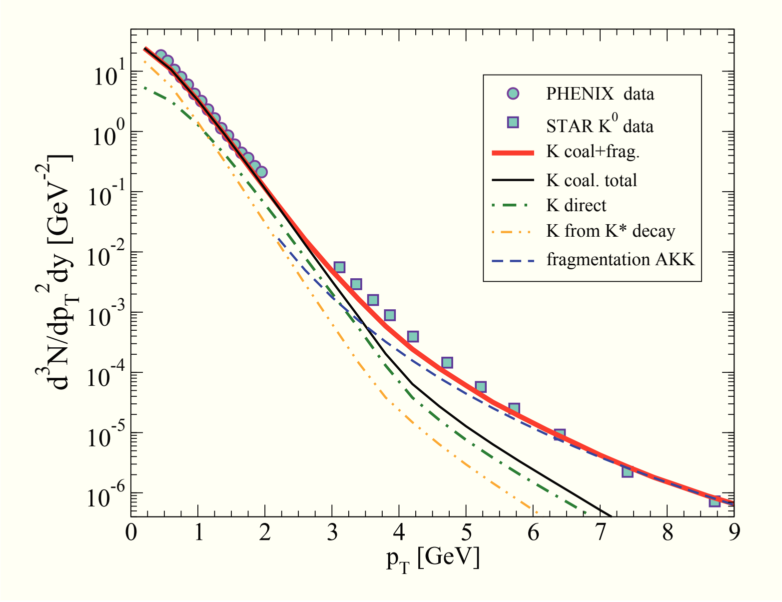

Figure 4.3: Kaon transverse momentum spectrum at RHIC in Au+Au collisions at $\sqrt{s} = 200\,AGeV$, $0-10\%$ centrality. Kaon production from coalescence is the thin solid. Direct kaons are shown by the dash-dotted line. Kaons from K^* decay are the dash-dotted line. Kaon from mini-jet fragmentation is the dashed line. Sum of both hadronization processes is shown by thick solid line. Experimental data from PHENIX [78] are shown by the circles, STAR [80] data are shown by the squares.

the coalescence contribution for protons extends in a region at higher momentum with respect to pions.

In Fig.4.3 we can see that also for Kaons the agreement with experimental data from PHENIX [78] at low p_T, circles, and STAR [80], squares, is fairly good in all the range of p_T . By dash double dotted orange line in Fig.4.3, we see that at low p_T the contribution from K^* decay becomes important and contributes to have the correct slope of the spectrum as measured experimentally. One can notice as in the case of pions that there is some lack of yield at $p_T \simeq 4GeV$ where the fragmentation, the dashed blue line, is starting to be dominant. We anticipate that such a systematic is observed also at LHC and from the ratio baryon/meson we will see that it is even more marked for baryons and in particular for Lambda.

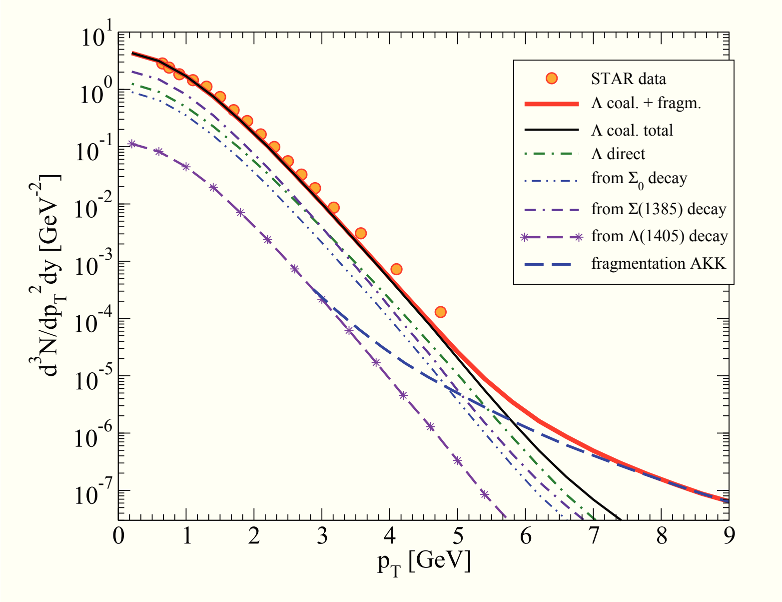

Figure 4.4: Λ transverse momentum spectrum at RHIC in Au+Au collisions at $\sqrt{s}$ = 200 GeV, 0 – 10% centrality. Λ production as sum of both hadronization processes is shown by thick solid line; from coalescence only by thin solid line. Direct Λs are shown by the dash-dotted line. Λ from resonance decay are: Σ^0 (dashed double dotted line), Σ(1385) (double dashed dotted line), Λ(1405) (dashed line with $*$ symbols). Λ from mini-jet fragmentation is the dashed line. Experimental data from STAR [81].

The p_T distribution for $\Lambda(1116)$ is shown in Fig.4.4 by thick solid red line along with the experimental shown by circles [81]. For the Λ there are indeed several hadronic states that have a significant contribution (see Table 4.4). Also for the Lambda the coalescence plus fragmentation model appear to be able to correctly described the experimental data in a wide range of p_T . We also find similarly to the anti-proton that the contribution from independent fragmentation according the AKK parametrization becomes dominant at $p_T \geq 6 GeV$.

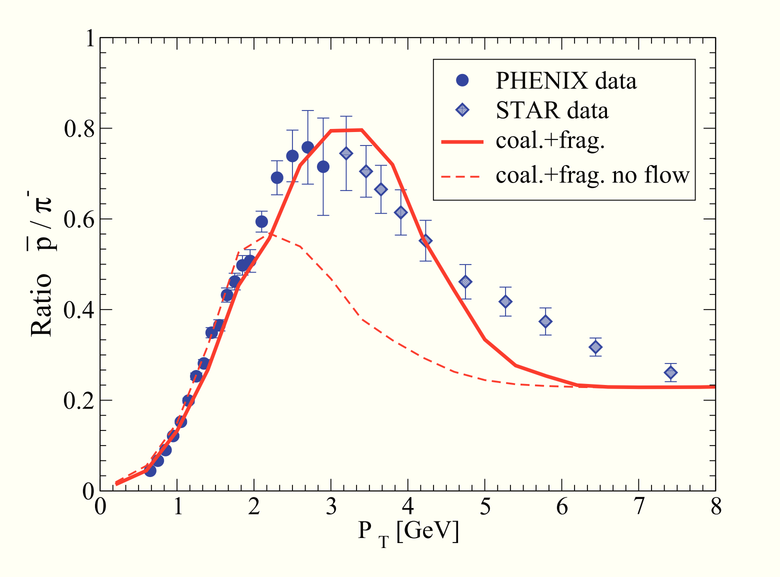

Figure 4.5: Particles ratio at RHIC from Au+Au collisions at $\sqrt{s} = 200\, GeV$.
(Left) Proton to positive pion ratio (blue solid line), antiproton to negative pion ratio (orange solid line). PHENIX [78] data are shown by circles, STAR [80] data by triangles. Data in pp collision are shown by the corsses and the x symbols
(Right) Antiproton to proton ratio (solid line), PHENIX [78] data (rhombuses), STAR [80] data (star symbols)

The coalescence mechanism has had the merit to naturally predict a baryon/meson enhancement at intermediate transverse momentum, especially in the region $p_T \simeq 2-4 GeV$ where the p/π^+, $\bar{p}/\pi^-$, $\Lambda/2K_s^0$ reaches a value of the order of unity which is a strong systematic enhancement with respect to the one observed in pp collisions [83]. We therefore show

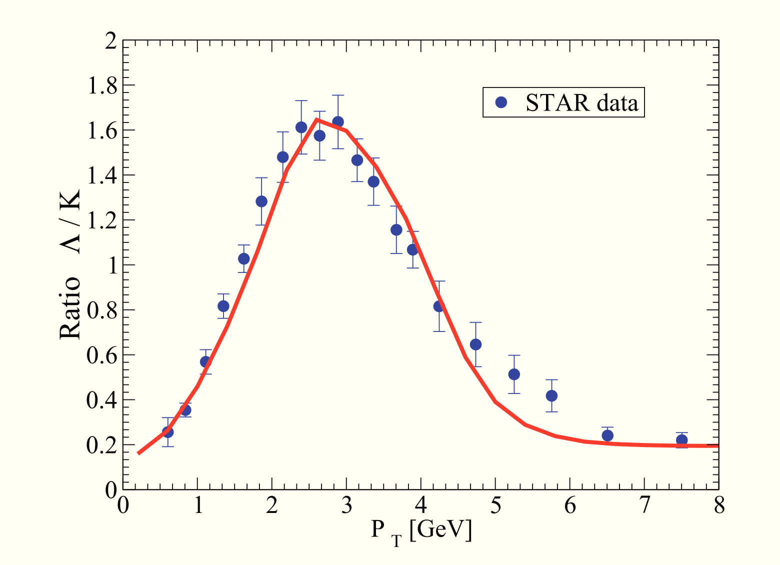

Figure 4.6: Lambda to kaon ratio at RHIC from Au+Au collisions at $\sqrt{s} = 200$ AGeV. The model prediction is the solid line. STAR data by circles [82].

the p/π^+, Λ/K_s^0 in the Fig.s 4.5 and 4.6. We can see that the ratio is quite well predicted from its rise at low p_T up to the peak region and then the falling-down behavior. However in both cases it is clear that in the region of $p_T \simeq 5-7\,\mathrm{GeV}$ there is a lack of baryon yield. This is a feature that could not be observed when the coalescence plus fragmentation model was applied a decade ago to hadronization at RHIC because there were no data available for proton (anti-proton) at $p_T \gtrsim 4\,\mathrm{GeV}$, nonetheless it appears systematically, we will see it also at LHC energy.

4.3 Spectra, ratio at LHC

In this section we show the results of our model for some observables measured at LHC in ALICE experiment.

We have considered Pb+Pb collisions at $\sqrt{s} = 2.7\,TeV$, in the class of centrality 0-10%. The fireball condition and the parton distribution varies as already described in paragraph 4.1.3, we remind that the radial flow and volume of the hadronizing fireball that as described above is self-consistently constrained but the total transverse energy and the multiplicity that at LHC $\sqrt{s} = 2.76\,ATeV$is about a factor 2.4 and 2.7 larger with respect to RHIC $\sqrt{s} = 200\,AGeV$. As widths of Wigner function we used the same of those assumed at RHIC as due to their physical meaning they should not change at varying the collision energy but are properties of the baryons.

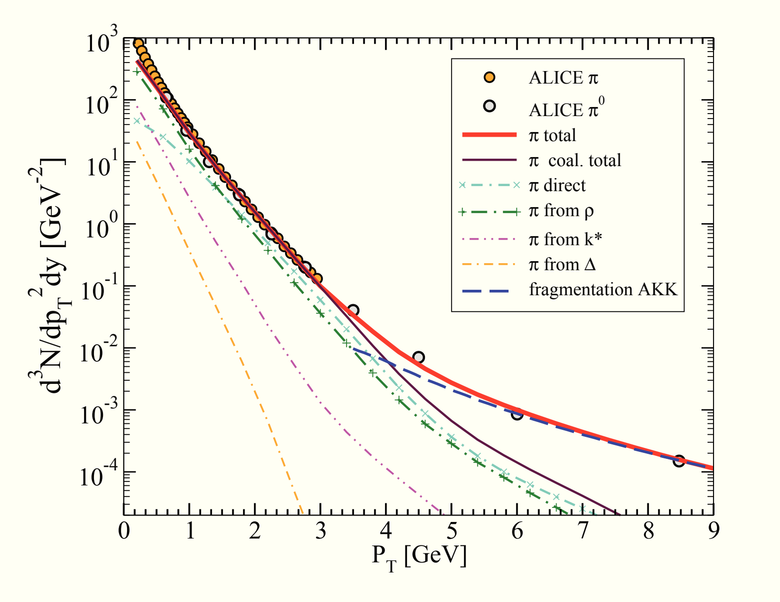

Figure 4.7: Pion transverse momentum spectrum from Pb+Pb collisions at $\sqrt{s} = 2.7\,TeV$. The dashed curve includes contributions from coalescence process. The solid line is the sum of coalescence and fragmentation contributions. The filled circles are the experimental data from ALICE experiment [84] [85]. The dot-dashed curve shown the pion transverse spectrum at RHIC.

In Fig.4.7 we show the sum of coalescence and fragmentation contribution to pion spectrum by thick solid red line which is in quite good agreement with the experimental data from ALICE Collaboration [84] [85] in all the p_T range, except some lack of yield at $p_T \lesssim 0.5\,GeV$ due to absence of all the resonance decays feed-down. By the thin solid orange and the dashed blue line we show the contribution from coalescence and fragmentation respectively. We notice that the two yields cross at $p_T \simeq 4\,GeV$ which is a shift of about 1 GeV with respect to RHIC, see

Fig. 4.1. Such a shift is due to the larger collective flow present at LHC that shifts to larger p_T the hadrons from coalescence . The very good agreement of the p_T distribution at LHC already shows that the model is able to correctly predict the evolution of the absolute yield and especially its p_T shape correctly, in fact no parameter of the coalescence process, essentially the Wigner wave function width Δ_p of the hadrons, has been modified with respect to those used in the previous Section for RHIC.

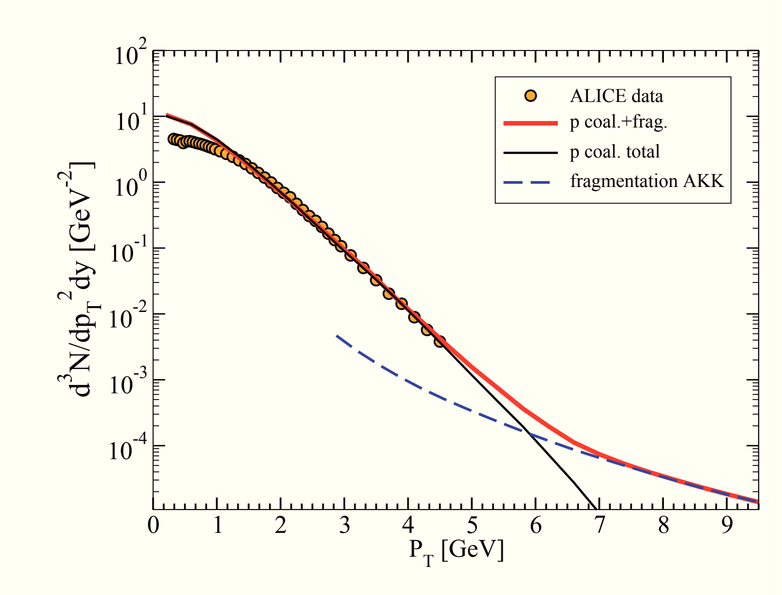

Figure 4.8: Proton transverse momentum spectrum from Pb+Pb collisions at $\sqrt{s} = 2.7\,TeV$. The dashed curve shows the contribution from coalescence process. The solid line is the sum of coalescence and fragmentation process. The filled circles are the experimental data from ALICE experiment [84].

In Fig.4.8 it is shown the proton spectrum at LHC by thick solid red line and compared to the experimental data [84]. The agreement also in this case is very good for $p_T > 1\,GeV$ up to $5\,GeV$ that is the maximum value with available data. At very low p_T as said in before we should not expect the approach to really apply. Still we can notice that the coalescence over predict the yield. The effect was partially present also at RHIC, see Fig. 4.2.

In Fig.4.8 we can also see that the yield of the fragmentation process, shown by the dashed blue line, becomes comparable to the one from coalescence (thin black line), at a $p_T \simeq 6\,GeV$ which is about a 50% larger with respect to the pions and also a shift of about $1.5 GeV$ with respect to RHIC. This is what one would expect due to the larger flow at LHC and the fact that baryon are more affected by it.

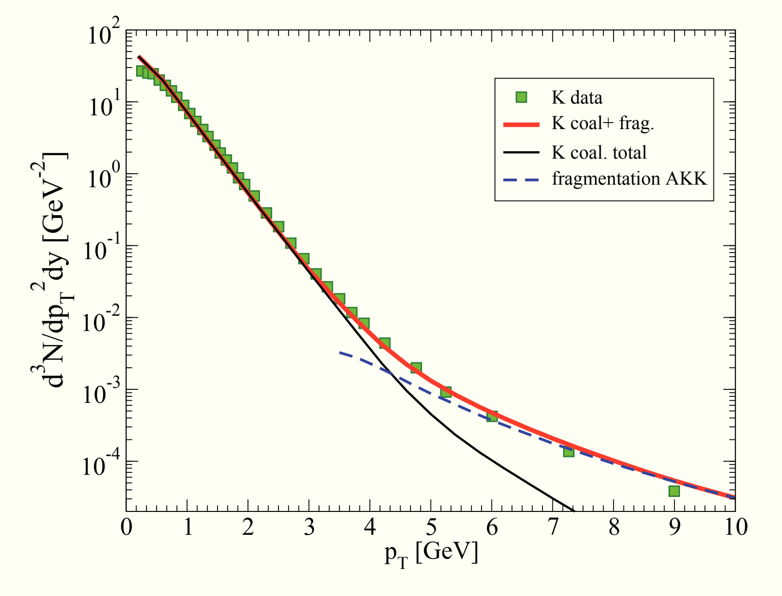

Figure 4.9: Kaon transverse momentum spectrum from Pb+Pb collisions at $\sqrt{s}$ = 2.7 TeV, 0 – 10% centrality. The dashed curve includes contributions from coalescence process. The thick solid line is the sum of coalescence and fragmentation contributions. Kaons from mini-jet fragmentation are the dashed line. The squares are the experimental data from ALICE experiment [84, 86, 87].

In Fig.4.9 the p_T distribution for K^+ is shown by thick solid line and again one can see the good agreement with the experimental data [84] [86][87] in the entire range of p_T. We can notice that at RHIC for both pions and kaons there was some lack of yield in the region where the fragmentation takes over, while at LHC energy for both cases the agreement appears quite better. This can be expected because the independent fragmentation function picture should be better constrained at energies of the order of TeV. In Fig.4.10 the experimental data for the

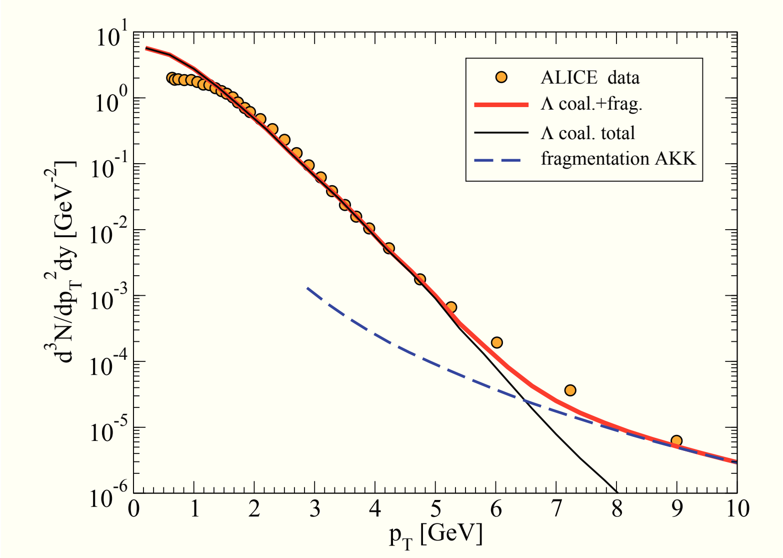

Figure 4.10: Λ transverse momentum spectrum from Pb+Pb collisions at $\sqrt{s}$ = 2.76 TeV, $0-10\%$ collisions. The thin solid curve includes all contributions from coalescence process.Λ from mini-jet fragmentation is the dashed line. The sum of coalescence and fragmentation contributions is shown by the thick solid line. The circles are the experimental data from ALICE experiment [86] [87].

transverse momentum spectrum of Λ is shown by circles together with the results from the coalescence plus fragmentation shown by thick solid red line. The different contribution from excited state have been calculated and have a similar relative contribution as at RHIC, see Fig.4.4 We can see also for this case the good agreement for $p_T > 1\,GeV$, but while for p and $\bar{p}$ the data are available only up to 4-5 GeV, in this case we have the availability of data up to 9 GeV and this allows us to see that in the p_T region where the fragmentation starts to dominate, $p_T \simeq 6-7\,GeV$ there is some lack of yield. At both RHIC and LHC such a lack of yield appears where coalescence becomes less important therefore one can say that it seems that the spectrum from AKK fragmentation function appears too flat. This may very well be because the fragmentation function for baryons in general and in particular for Λ are known to be not very well constrained. On the other hand we notice that the fragmentation contribution has been calculated for all hadrons considered with the same $Q^2 = (p_{had}/2z)^2$ and this gives a global good description of the spectra for π, K at $p_T > 5\,GeV$ and for $p, \bar{p}, \Lambda$ for $p_T > 8\,GeV$. Some improvement for the baryons can be achieved if one set a harder scale for them, however the issue of some lack of yield at intermediate p_T persists. It is likely that studies of in-medium fragmentation function can solve it [88, 89] or it could be that coalescence contribution should extend to large p_T with respect to the present modeling having simple spheres in momentum space as Wigner function and no dynamical role of the interaction that could lead to an extension of the coalescence to pair with larger relative momentum.

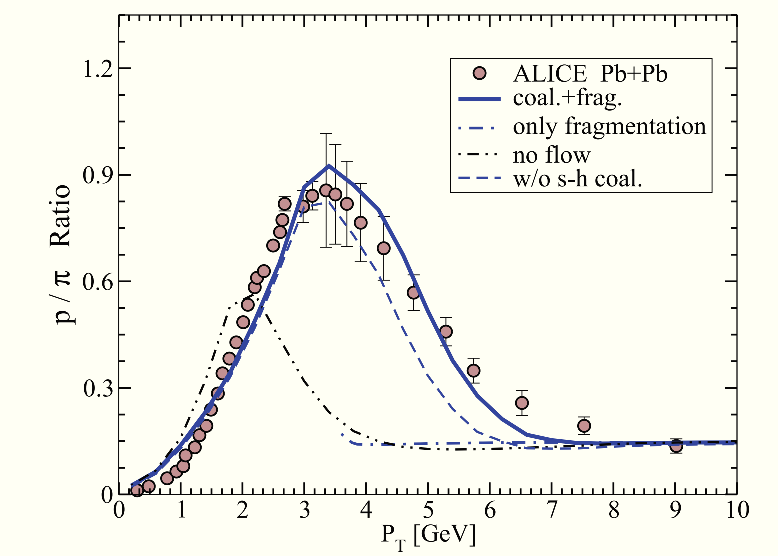

Figure 4.11: Proton to pion ratio in Pb+Pb collisions at $\sqrt{s} = 2.7\,TeV$. The solid line is the prediction of our model. The empty circles are data from ALICE experiment in collision Pb+Pb at 0-5% centrality. The filled circles are data from p+p collisions

We mention that recently it has been developed a process that within the coalescence plus fragmentation approach could be quite important in solving this issue [88]. The idea is to describe the in-medium fragmentation as a quark recombination of shower partons taking into account also the gluon splitting into quark pairs that recombine.

In Fig.4.11 we compare the p/π ratio vs p_T shown by solid line with the experimental data of the ALICE Collaboration [90] shown by open circles. The description is overall quite good with some quite limited lack of proton yield at $p_T \sim 6\,GeV$. In Fig.4.11 it is also shown by dashed line the p/π ratio if the coalescence between soft partons from the QGP and a mini-jet. We can see that the contribution is significant for $p_T > 3\,GeV$. The impact of radial flow of the soft partons is shown by dashed double-dotted line. In Fig. 4.12 we show the results for the Λ/K ratio in comparison with the experimental data shown by circles [86]. We can see generally a good overall description of the ratio especially in the region of the peak. Comparing the dashed-dot line with the thick solid line we can see that in the peak region a quite good agreement with the experimental data is reached thanks to a recombination of thermal soft partons with a mini-jet parton. The relevance of such a process is present also in the EPOS approach Ref.[89], ad it is an idea that can be traced back to ref.[91] However as discussed above at $p_T \sim 6\,GeV$ there

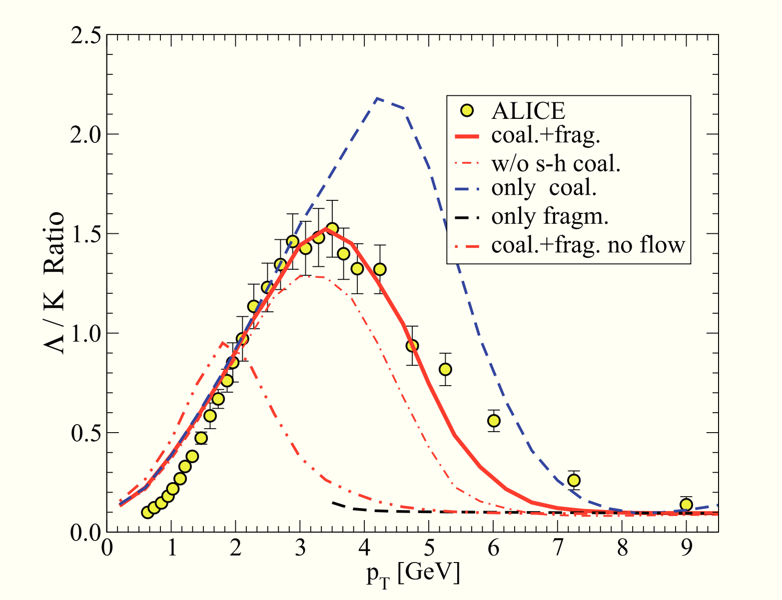

Figure 4.12: Lambda to kaon ratio in Pb+Pb collisions at $\sqrt{s} = 2.7\,TeV$. The solid line is the prediction of our model. The circles are data from ALICE experiment in collision Pb+Pb at 0-5% centrality. [86]

is a significant lack of Λ yield that here in a linear scale appears quite large. A tendency to underestimate the yield is visible also in [89] even if quite smaller thanks to a different fragmentation scheme with respect to AKK. The low ratio is only slightly low because of the large K yield in this p_T range,see Fig.4.9, and most of the disagreement with the data comes from the lack of yield in the $\Lambda's$ distribution from fragmentation that appears too soft in this p_T range. In Fig.4.12 we also show the behavior of the Λ/K ratio if only coalescence is considered, dashed line, or if only fragmention is included.

In Fig. 4.13 we show also the ϕ meson spectra obtained rescaling the width parameter Δ_{meson} , according to harmonic oscillator width $\sqrt{m_q/m_s}$. It is often discussed whether the p_T spectra of ϕ meson would have a slope close to the one of the proton like in a hydropicture or would behave like other mesons being formed by two quarks. We briefly mention that indeed also in a coalescence process one can and should expect that there is a radial flow mass effect like in a hydropicture. In fact for a proton there is a combination of three quarks flowing each with a mass of about $330 MeV$ while for a ϕ meson there are two quarks flowing each with a mass of about 550 MeV. The difference between these two cases is of course only marginal; in fact we can see in Fig. 4.13 that at low p_T the slope of ϕ (orange thin solid line) is quite similar to the one of the proton. In the inset we show more in detail the p/ϕ ratio including only coalescence for ϕ (solid line). We can see that at $p_T \lesssim 2 GeV$ the ratio is nearly flat. At higher p_T there is a peak at about 4 GeV which signals that the slope of the ϕ is stiffer; on the other hand as we see for the other mesons at such a p_T there is a significant contribution from fragmentation. Unfortunately there are no ϕ AKK (or KKP) fragmentation functions and it is not possible to perform a solid prediction at higher p_T . However, considering that the prediction for the ϕ in a coalescence

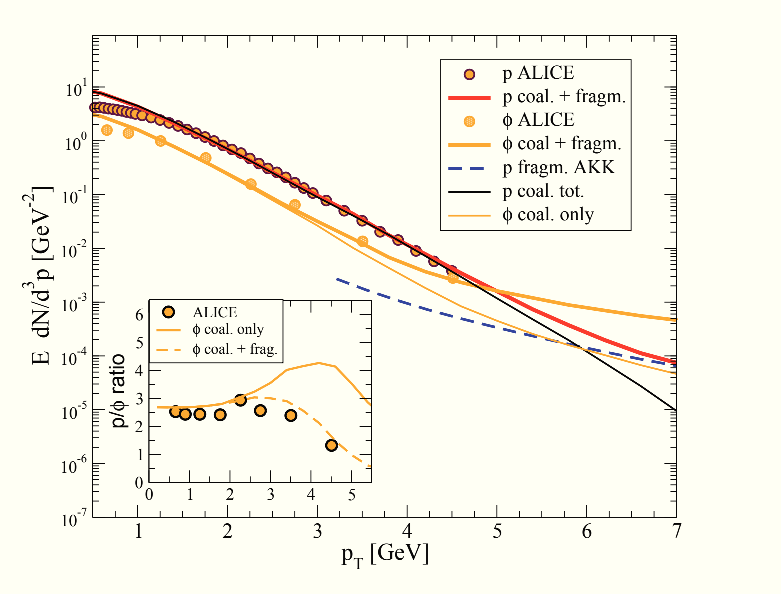

Figure 4.13: Proton and ϕ transverse momentum spectrum from $Pb+Pb$ collisions at $\sqrt{s}=2.76\,TeV$, 0% – 10% centrality. The solid thick line is the sum of coalescence and fragmentation process; for ϕ see the text. The solid thick orange line is the total ϕ spectrum and the light thin line is the contribution from only coalescence (see text). The circles are the experimental data from ALICE experiment [84, 92]. In the inset the p/ϕ ratio is shown

plus fragmentation approach is particularly awaited, we show in the inset (dashed line) and in the main panel (thick solid line), what would be the p_T distribution of ϕ if one adds a fragmentation corresponding to the same fragmentation over the coalescence ratio as for the K^+ meson. We can see that as for the other ratios we have quite good agreement with the data by ALICE shown by circles [92].

CHAPTER 5

HEAVY QUARKS

Heavy quarks (*charm* and *bottom*) and their bound states (*charmonia* and *bottomonia*) are recognized as particularly suitable probes of the medium produced in ultrarelativistic heavy-ion collisions. In particular heavy quark states are created essentially in the early stage of the collisions and since their masses are much larger than the temperature of the medium, their thermal production is marginal. A puzzling relation between Heavy Quarks nuclear modification factor R_{AA} and the elliptic flow v_2 has been observed both at RHIC and LHC energies. In fact different models if succeed in correctly predict R_{AA} than the associated v_2 is generally quite smaller with respect to experimental data. The hadronization mechanism, and specifically coalescence, can modify the relation between these two observables. In this chapter we show our study of the impact of coalescence for the results for R_{AA} and v_2 of D meson.

5.1 Introduction

In discussing the heavy quarks physics in QGP we refer exclusively to the charm and bottom flavours. The top quark that has a mass of

$174 GeV$ has a lifetime of about $10^{-24} s$ and decays directly in $t \rightarrow bW$ without creating bound states. Therefore its lifetime is too small with respect to the QGP lifetime and they cannot be observed directly and till now are not considered as a probe of the plasma dynamics. The charm quark has a mass of $1.3\, GeV$, the bottom quark has a mass of $4.5\, GeV$. These masses are significantly larger than the Λ_{QCD} and thus, their dynamics should be reasonable well described in a perturbative regime. Indeed next-to-leading order calculation have successfully predicted charm and bottom production in pp collisions at RHIC and LHC energy. However experimental results have shown that for charm quarks perturbative interaction is too small to reproduce the observed nuclear modification factor. This means that after they are produced their coupling to the bulk QGP medium is quite strong.

Another peculiar characteristic of heavy quarks is that their masses are well above the typical temperature of the system, (i.e. $m_Q \gg T$). Therefore, their thermal production is negligible, and the production of heavy quark pairs $\bar{Q}Q$ is related with the initial collisions of nucleons. The successive interactions with the evolving and expanding medium would not change the number of heavy quark, with no contribution of thermal excitation of the vacuum to produce $\bar{c}c$ or $\bar{b}b$.

The thermal relaxation time for light quark and gluon is $\tau_{q,g} \simeq 0.3 - 1 fm/c$ that is smaller than the estimated QGP lifetime of $\tau_{QGP} \simeq 5 fm/c$ in central $Au - Au$ collisions. But for heavy quark the thermalization time is expected to be larger by a factor $\sim m_Q/T \approx 8 - 30$. So, τ_{HQ} is of the same order or larger than τ_{QGP} for charm quark and significantly larger in the bottom quark case. Thus, heavy quarks are not expected to reach thermal equilibrium. But their re-interactions should create noticeable modifications on the initial momentum spectrum, so the final spectra may therefore carry a sort of "memory" of the interaction history throughout the evolving fireball.

The typical thermal momentum of a heavy quark $p_{th}^2 \simeq 3m_Q T \gg T^2$ is much larger than the momentum transfer from the medium, $Q^2 \sim T^2$. So the interaction of heavy quarks can be treated as a Brownian motion in a bath of light quarks and because of the momentum transfer smallness, a Fokker-Planck description of the diffusion is possible.

The heavy flavour investigation started at RHIC Au+Au collisions at $\sqrt{s_{NN}} = 200\,GeV$ per nucleon by the measurement of single nonphotonic high p_T electrons originated by the semi-leptonic decay of heavy mesons with no possibility to distinguish between electrons coming from D or B meson. The spectra depends from the differential distribution of produced heavy quarks, the branching ratio for semi-leptonic decay of heavy meson, and from the fragmentation function of HQ into open heavy flavoured meson, used here with the parametrization given by the Peterson's function [93].

$$D(HQ \to h_{HQ})(z) \propto \frac{1}{z\left[1-\frac{1}{z}-\frac{\epsilon}{1-z}\right]} \tag{5.1}$$

where z denotes the fraction of the heavy quark momentum carried by the heavy flavoured hadron and ϵ is the mass squared ratio between the light quark (antiquark) and the heavy antiquark (quark) forming the bound mesonic state.

Among the several physical quantities we have already discussed for probing QGP properties, there are principally two main observables for the investigation of heavy flavour sector both at RHIC and LHC. The nuclear modification factor R_{AA} and the elliptic flow v_2.

First predictions of a $R_{AA} \approx 0.6$ for charm quarks and $R_{AA} \approx 0.8-0.9$ for bottom quarks in central collisions at intermediate transverse momentum associated with a small value of elliptic flow with regard to the equivalent for light quarks were soon retracted by the measures of such observables. The measured values of R_{AA} for single non-photonic electrons at RHIC and for D mesons at LHC are respectively of 0.5 and 0.4

at $p_T \approx 5GeV$ while the corresponding v_2 at RHIC shows a characteristic bump at $p_T \approx 2GeV$.

These indications reveal a quite strong interactions between heavy quarks and the medium which is substantially beyond the expectations coming from perturbative QCD.

Several theoretical efforts have been made to reproduce the R_{AA} and the v_2 observed in experiments within the Fokker Planck approach [94][95] [96] [97][98][99][100] and the relativistic Boltzmann approach [101][102] [103][104]. However all the approaches show some difficulties to describe simultaneously R_{AA} and v_2.

In our research group, has been thoroughly studied the differences between Fokker-Planck and Boltzmann approach, the first one in fact is an approximation of the Boltzmann equation, valid when the momentum transferred is smaller than the heavy quark momentum. The results of these studies have shown that the Fokker-Planck approximation is not provides a good description of the integrated observables, like the R_{AA} but is less efficient to reproduce more differential observables , like the elliptic flow. In particular, it seems that the Fokker-Planck slightly underestimates the elliptic flow [103].

In this work the heavy quark dynamics is obtained solving the full Boltzmann collision integral.

5.2 Transport equation for heavy quarks

In heavy quarks scenario hydrodynamics is not applicable by the fact that they are produced in the early out-of-equilibrium stage of QGP formation. Furthermore their relaxation time is comparable to τ_{QGP} and as a consequence they do not evolve as a probe in thermal equilibrium. Heavy quarks probe the QGP because they collide with the bulk constituents, thus enclosing the heavy quarks interaction in the collision integral of the Boltzmann equation appears to be a suitable way to tackle the problem. The relativistic collision integral for two-body collisions can be written in another form in order to show explicitly the collision rate

$$C_{22}(x,p_1) = \int d^3\vec{q}\,[w(p_1+q,p_1)f(x,p_1+q) - w(p_1,q)f(x,p_1)] \tag{5.2}$$

where $w(p_1+q,p_1)$ and $w(p_1,q)$ are respectively the rate of gain term for which particle changes momentum from p_1+q to p_1 and the rate of loss term which changes momentum form p_1 to p_1-q by the transfer of the same amount of momentum q.

The total collision rate is the sum of three contribution which represent each one the collision rate for $HQ+q$, $HQ+\bar{q}$ and $HQ+g$ scattering processes. Hence

$$w(p_1,q) = w_q(p_1,q) + w_{\bar{q}}(p_1,q) + w_g(p_1,q) \tag{5.3}$$

and for example $w_g(p_1,q)$ is defined as

$$w_g(p_1,q) = \gamma_g \int \frac{d^3\vec{l}}{(2\pi)^3} f_g(\vec{l})\, v_{rel}\, \sigma_{HQ+g\to HQ+g} \tag{5.4}$$

where γ_g is the degeneracy factor for gluons ($\gamma_g = 2\cdot 8$), v_{rel} is the relative velocity between the heavy quark and the gluon and $\sigma_{HQ+g\to HQ+g}$ is the total cross section for the elastic heavy quark-gluon scattering.

A successful way to account for non-perturbative dynamics is a quasi-particle approach, in which the interaction is encoded in the quasi-particle masses [105]. The mass of the particles can be viewed as arising from the energy contained in a strongly coupled volume determined by the correlation range of the interaction. Once the interaction is accounted for in this way, the quasi-particles behave like a free gas of massive constituents. The T-dependent quasi-particle masses are included in the following way

$$m_q = \frac{1}{3}g_s^2(T)T^2 \qquad\qquad m_g = \frac{3}{4}g_s^2(T)T^2 \tag{5.5}$$

To successfully reproduce the thermodynamics of Lattice QCD the strong coupling constant $g_s(T)$ is evaluated by making a fit of the energy density obtained by lattice QCD calculations and can be parametrized as

$$g^2(T) = \frac{48\pi^2}{\left(11N_c - 2N_f\right)\ln\left[\lambda\left(\frac{T}{T_c} - \frac{T_s}{T_c}\right)\right]^2} \tag{5.6}$$

In order to deal with the hadronization mechanism we use the model of coalescence and fragmentation treated for light quark hadronization in Chapter 4.

We assume that in our system the collisions between light quarks and heavy quarks are stopped when the temperature of a cell drops below the critical temperature, that here has been setted at $T = 150\,MeV$.

Fragmentation is the predominant hadronization mechanism for heavy quark with high momentum transferred, while the coalescence mechanism become predominant when the quarks have low momenta.

5.3 Comparison with the experimental observables

We present in this section results for nuclear modification factor R_{AA} and for elliptic flow v_2, and the comparison with experimental data. We calculate R_{AA}, using our initial $t = 0$ and final $t = t_f$ heavy meson distribution as $R_{AA}(p) = \frac{f(p,t_f)}{f(p,t_0)} = \frac{dN/d^2p_T dy|_{t=t_f}}{dN/d^2p_T dy|_{t=t_0}}$.

The anisotropic momentum distribution is calculated by means of the elliptic flow v_2, that is the second harmonic in azimuthal distribution:

$$v_2 = \left\langle \frac{p_x^2 - p_y^2}{p_T^2} \right\rangle \tag{5.7}$$

We have carried out simulation of Au + Au collisions at $\sqrt{s} = 200\,GeV$.

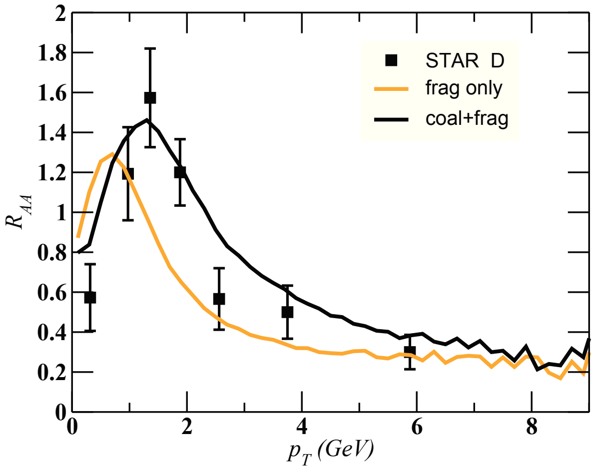

Figure 5.1: D meson R_{AA} in $Au+Au$ collisions at $\sqrt{s} = 200 GeV$ and centrality $0-10\%$ compared to STAR data [106]

The initial condition for the bulk in coordinate space are given by the standard Glauber condition. While in the momentum space a Boltzmann-Juttner distribution function is used, up to $p_T = 2GeV$, and mini-jet distributions at larger momenta, the last one are calculated by pQCD at NLO.

Initial maximum temperature at the center of the fireball is setted at $T_0 = 340 MeV$, and the initial time is $\tau_0 = 0.6 fm/c$.

Initial distribution of charm quarks are taken from Ref. [107] and given by $f(p,t=0) = (a+bp)^{-n}$ with $a = 0.70$, $b = 0.09$ and $n = 15.44$. The above function gives a good description of D meson spectra in pp collision at highest RHIC energy.

To describe the bulk evolution we have developed an approach in which fixed η/s the cross-section is evaluated [108] [109]. Chapman-Enskog approximation is used in order to evaluate locally the cross section from η/s. In this way we are able to simulate the dynamical evolution of a fluid with specified shear viscosity by means of the Boltzmann equation, in analogy with hydrodynamical simulations.

The bulk dynamical evolution is constrained by an $\eta/s = 1/4\pi$, in such

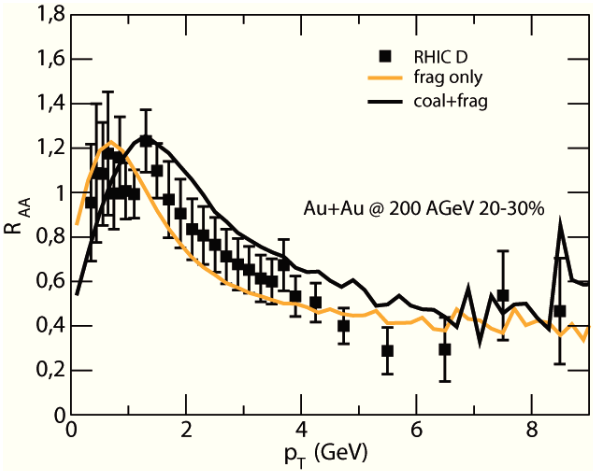

Figure 5.2: D meson R_{AA} in$Au+Au$ collisions at $\sqrt{s}=200GeV$ and centrality $20-30\%$ compared to STAR data [106]

way the model reproduces experimental data for bulk elliptic flow .

When the system reaches locally the critical temperature the one body distribution function of heavy quark is frozen and momentum distribution, nuclear modification factor and elliptic flow of D mesons are evaluated after the hadronization process.

In Fig.5.1 and Fig.5.2 the nuclear modification factor as a function of p_T in $Au+Au$ collisions at $\sqrt{s}=200GeV$ for centralities 0-10% and 20-30% is depicted and compared with experimental data observed at STAR [106].

In this figures we compare the impact of coalescence on R_{AA}, showing the nuclear modification factor obtained considering only fragmentation (orange line) with results for R_{AA} obtained including coalescence mechanism, that are indicated with the black line. We can observe that coalescence implies an increasing of R_{AA} for momenta larger than $1GeV$, thus a reduction of the suppression. This is due to the hadronization mechanism which implies that a D mesons with a given momentum is the results of the coalescence of one light quark and a charm quark having a smaller momentum with respect to the D mesons. This along with the fact that charm spectrum decreases with p_T implies that the final spectrum of D meson does not scale with the spectrum of the original charm and an increasing in the number of particle in the region of $p_T > 1\,GeV$ is observed. The impact of coalescence decreases with transverse momentum because at higher p_T the D meson spectrum is dominated by the fragmentation mechanism of hadronization.

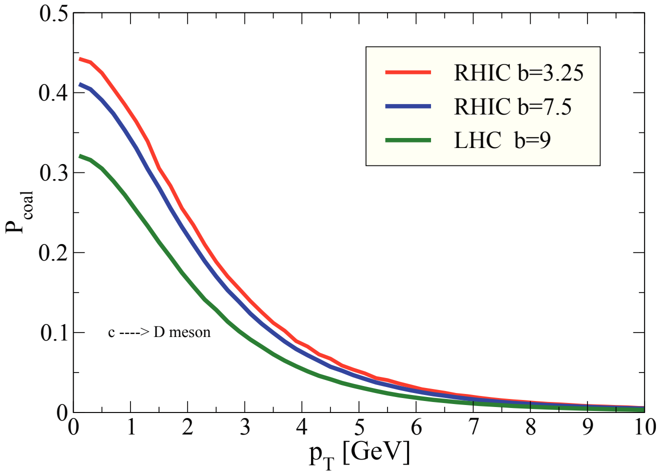

Figure 5.3: Coalescence probability as a function of transverse momentum

As shown in Fig.5.3 where the probabilty of a charm quark to hadronize through coalescence is plotted as a function of p_T, coalescence probability decreases fast, and becomes negligible starting from intermediate transverse momentum region $(4-5\,GeV)$.

In Fig.5.4 is shown the D meson elliptic flow in $Au+Au$ collisions at $\sqrt{s} = 200\,GeV$ and centrality $20-30\%$ compared to STAR data [110]. The different lines allow us to show the impact of coalescence on the generation of the elliptic flow. The thin solid red line indicates the original charm quark elliptic flow without considering any hadronization mechanism, while the dashed double dot black line indicates the D mesons v_2 obtained considering fragmentation as the only hadronization mechanism. Contributions from D and D_s that comes only from the coales-

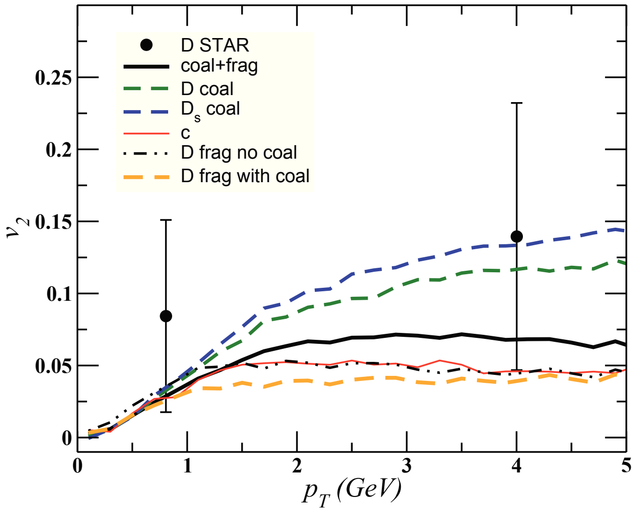

Figure 5.4: D meson elliptic flow in $Au+Au$ collisions at $\sqrt{s} = 200\,GeV$ and centrality $20-30\%$ compared to STAR data [110]

cence are shown with dashed blue and green line. Coalescence mechanism gives a D meson elliptic flow that is larger than charm quark elliptic flow. The explanation is that D meson comes from coalescence of a charm quark and a light quark and thus the final anisotropy in momentum space reflects both heavy quark and light quark anisotropies in momentum space, with the latter that is larger than the first.

The dashed orange line is the elliptic flow that comes from fragmentation of quarks that have not undergo coalescence. In this case the elliptic flow is smaller than that obtained when fragmentation is the only hadronization mechanism, indicated by dashed double dotted black line. This result is an indirect consequence of the phase space selection that coalescence mechanism entails. In fact a charm quark will couple with a light quark to form a D meson if quark momenta are similar (and if they are close in the phase space in a way that satisfy conditions imposed by Wigner function widths). Since probability to find a light quark with a given momentum is not isotropic in transverse plane, as explicitly indicated by the non zero elliptic flow, thus also coalescence probability is not isotropic. As a consequence all heavy quarks undergoing coalescence

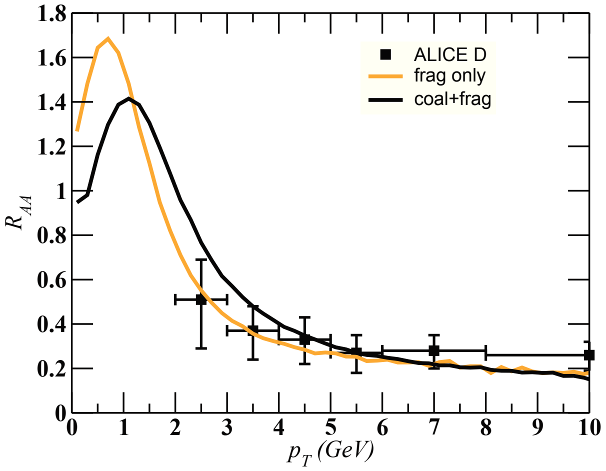

Figure 5.5: D meson R_{AA} in $Pb+Pb$ collisions at $\sqrt{s} = 2.7TeV$ and centrality $0-20\%$ compared to ALICE data [111]

have an elliptic flow that tends to be similar to that of light quark, the final effect is that coalescence tends to remove those heavy quarks which have high elliptic flow. So the elliptic flow of that heavy quarks which do not coalescence results to be smaller than the elliptic flow calculated initially for all charm quarks. The solid black line is the weighted mean of coalescence and fragmentation contribution.

In Fig.5.5 are shown the results for D meson R_{AA} in $Pb+Pb$ colli-

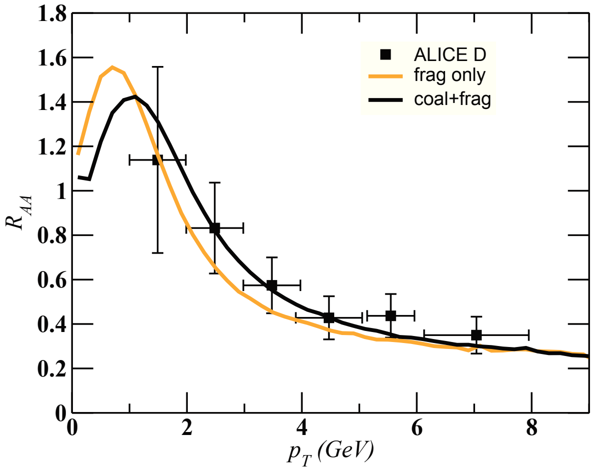

Figure 5.6: D meson R_{AA} in $Pb+Pb$ collisions at $\sqrt{s} = 2.7TeV$ and centrality $30-50\%$ compared to ALICE data [111]

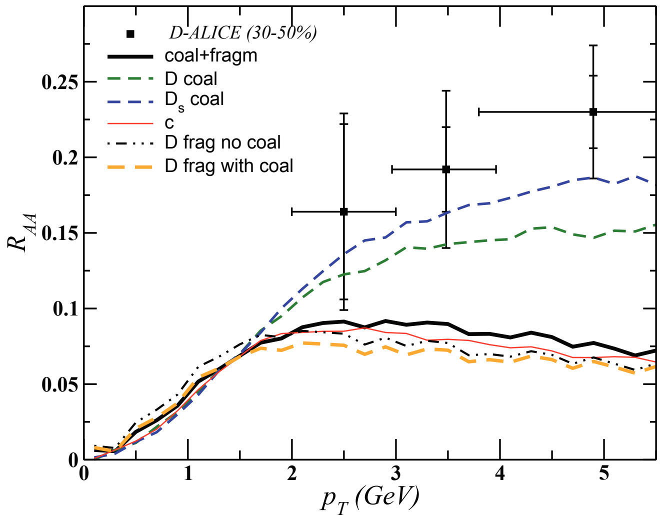

Figure 5.7: D meson elliptic flow in $Pb+Pb$ collisions at $\sqrt{s} = 2.7\,TeV$ and centrality $30-50\%$ compared to ALICE data [111]

sions at $\sqrt{s} = 2.7\ TeV$ and centrality $0-20\%$ compared to ALICE data [111]. In this case the initial maximum temperature in the center of the fireball is $T_0 = 510\,MeV$ and the initial time for the simulations is $\tau_0 \sim 1/T_0 = 0.3\,fm/c$. In Fig.5.6 and Fig.5.7 are plotted the results for D meson R_{AA} and elliptic flow in $Pb+Pb$ collisions at $\sqrt{s} = 2.7\ TeV$ and centrality $30-50\%$ compared to ALICE data [111].

For both centralities, coalescence (solid black line) implies an increasing of the nuclear modification factor for momenta larger than $1\,GeV$, however the effect seem to be smaller than at RHIC.

In Fig.5.7 are shown the different contributions from coalescence, fragmentation and initial charm elliptic flow. The final effect of coalescence here, is analogous as in the case of RHIC but is smaller in magnitude. The impact of coalescence at LHC is smaller than at RHIC, because the spectra of charm quarks has less prominent slope, moreover the model predicts a larger relative production of D mesons coming from charm quark fragmentation at LHC with respect to RHIC.

The nuclear modification factor and elliptic flow are related one to another. A key result of our study is that when R_{AA} increases, elliptic flow decreases and viceversa. Generally in order to get the same R_{AA} that we have without including coalescence is necessary to further increase the interaction, which causes an additional increase of the elliptic flow. Coalescence inverts this relation, implying a contemporary increase of both these two observables. Finally we can state that, in light of these outcomes, hadronization via coalescence is fundamental to reproduce the experimental data.

CHAPTER 6

DYNAMICAL COALESCENCE COUPLED TO BOLTZMANN TRANSPORT THEORY

In this chapter we discuss the Transport Boltzmann equation starting from the classical equation to the relativistic generalization. The Transport Theory is particularly suited to deal with the hadronization process because is constructed on a one-body distribution function, and thus allows for a direct treatment of hadronization. Moreover the transport approach can describe non-equilibrium states treating in a unified way short range interactions, due to collisions between particles, and long range interactions, associated to mean field dynamics that drives the equation of state.

6.1 Classical Boltzmann Equation

The general idea in order to describe the macroscopic properties of a dilute gas is to define a "grid" in phase space consisting of volume elements d^3x and d^3p in position and momentum space, which are infinitesimally small on a macroscopic scale over which the bulk properties

like the density of gas particles and the momentum-distribution of particles change.
Hence, instead of describing the system of N particle writing down every single equation of motion, taking in account of $3N$ position coordinates and $3N$ momentum coordinates and follow their trajectories in the $6N$ dimensional phase space with time, we study the properties and the evolution of the single particle distribution $f(x,p,t)$ which is defined such that

$$dN = d^3x\, d^3p\, \frac{g}{(2\pi\hbar)^3}\, f(x,p,t) \tag{6.1}$$

is the number of particles contained in the portion of phase-space volume considered at the instant of time, t.
We assume that the gas is sufficiently dilute that only binary collisions need to taken into account.

From one single particle distribution function is possible to get the spatial density $\rho(x)$ by performing on integration over momenta

$$\frac{N}{V} = \int d^3p\, f(x,p) = \rho(x) \tag{6.2}$$

The average value of any physical observable $O(x,p)$ can be evaluated as

$$\langle O(x,p)\rangle = \frac{1}{\rho(x)} \int d^3p\, O(x,p) f(x,p) \tag{6.3}$$

In the simple case when there are no collisions, for a single particle after a time $t+\delta t$ the coordinates (x,p) transforms in $(x+v\delta t, p+F\delta t)$, where F is an external force applied to the particle and $v = p/m$ is its velocity. Therefore, without collisions, all the particles in the initial volume element $d^3x\, d^3p$ will be after a time δt in the volume $d^3x'\, d^3p'$ centered in $(x+v\delta t, p+F\delta t)$. This is equivalent to say that

$$f(x+v\delta t, p+F\delta t, t+\delta t) = f(x,p) \tag{6.4}$$

By making a first order expansion δt we obtain the equation of motion for the distribution function

$$\left(\frac{\partial}{\partial t}+\frac{p}{m}\cdot\nabla_x+F\cdot\nabla_p\right)f(x,p)=0 \tag{6.5}$$

When the collisions between particles are also considered, the equation 6.5 is modified by additional terms that is a functional of the distribution function and is called collision integral $\mathscr{C}[f]$ because

$$f(x+v\delta t,p+F\delta t,t+\delta t)=f(x,p)+\mathscr{C}[f] \tag{6.6}$$

it brings the information about the change of the distribution function due to collisions. By making a first order expansion in δt, as we did previously for the case without collisions, the following expansion is obtained

$$\left(\frac{\partial}{\partial t}+\frac{p}{m}\cdot\nabla_x+F\cdot\nabla_p\right)f(x,p)=\mathscr{C}[f] \tag{6.7}$$

.

An explicit form for the collisional integral can be obtained assuming that particles interact through binary collisions and there are no external forces.

The number of transitions $12\to 1'2'$ in a volume element d^3x at r, owed by collisions during the time interval δt is

$$dN_{12}\,dP_{12\to 1'2'}\,\delta t$$

Where dN_{12} is the initial number of colliding pairs with momenta (p_1,p_2) and can be written as

$$dN_{12}=\hat{f}(x,p_1,p_2,t)\,d^3x\,d^3p_1\,d^3p_2 \tag{6.8}$$

introducing the two-particle correlation function $\hat{f}$. The other quantity which is necessary in order to define the number of transitions is the collision probability $dP_{12\to1'2'}$. A collision is a transition from the initial state to a set of final states. For final states in the infinitesimal momentum-space element $d^3p'_1\, d^3p'_2$ we have

$$dP_{12\to1'2'} = d^3p'_1\, d^3p'_2\, \delta^4(P_f - P_i)|T_{fi}|^2 \tag{6.9}$$
$$\delta^4(P_f - P_i) \equiv \delta^3(\mathbf{P_f} - \mathbf{P_i})\, \delta(E - E')$$

where T_{fi} is the transition amplitude for the scattering process and $\delta^4(P_f - P_i)$ is the energy-momentum conservation, which restricts the final allowed phase space states only to those accessible by elastic on-shell process.

An explicit form for $\mathscr{C}[f]$ can be obtained considering that during the time interval δt some particles in the volume element at (r,p,t) will be removed by collision. The volume element is so small that any collision that a particle suffers will knock it out of the volume element. These particles will not be in the volume element at $(r + v\delta t, p + F\delta t, t + \delta t)$. On the other hand, there are particles outside the initial volume element which, through collisions, will get into it during the time interval δt. Therefore the number of particles in the final volume element at $t + \delta t$, as $\delta t \to 0$, equals the original number of particles in the initial volume element at time t plus the net gain of particles due to collisions during the time interval δt. This statement may be expressed in the form

$$\mathscr{C}[f]\delta t = (\bar{R} - R)\delta t \tag{6.10}$$

where $R(\bar{R})\delta t d^3r\, d^3p$ is the number of collisions occurring during the time between t and $t + \delta t$ in which one of the initial (final) particles is in $d^3r\, d^3p$ about (r,p).

To proceed further, we assume that the gas is dilute, so that we may consider only binary collisions and ignore the possibility that three or more particles may collide simultaneously. Using Eq.(6.8) the rates can be written as

$$R\, \delta t\, d^3r\, d^3p_1 = \delta t\, d^3r\, d^3p_1 \int d^3p\, dP_{12\to1'2'}\, \hat{f}(x, p_1, p_2, t) \tag{6.11}$$

and using Eq.(6.9)

$$R = \int d^3p_2\, d^3p'_1\, d^3p'_2\, \delta^4(P_f - P_i)|T_{fi}|^2\, \hat{f}(x, p_1, p_2, t) \tag{6.12}$$

and similarly

$$\bar{R} = \int d^3p_2\, d^3p'_1\, d^3p'_2\, \delta^4(P_i - P_f)|T_{if}|^2\, \hat{f}(x, p'_1, p'_2, t) \tag{6.13}$$

The δ functions in Eq.(6.12) and Eq.(6.13) are identical, and $|T_{fi}| = |T_{if}|$. So Eq.(6.10) becomes

$$\mathscr{C}[f] = (\bar{R} - R) \int d^3p_2\, d^3p'_1\, d^3p'_2\, \delta^4(P_f - P_i)|T_{fi}|^2\, (\hat{f}_{1'2'} - \hat{f}_{12}) \tag{6.14}$$

where $\hat{f}_{1'2} = \hat{f}(x, p'_1, p'_2, t)$. The expression obtained is exact for a sufficiently dilute gas. But the correlation function f is unknown. Now we can consider the "assumption of molecular chaos", that says that the momenta of two particles in the volume element d^3r are uncorrelated, so that the probability of finding them simultaneously is given by the product of the probability of finding each alone. This means that we assume that

$$\hat{f}(x, p'_1, p'_2, t) \approx f(x, p_1, t) f(x, p_2, t) \tag{6.15}$$

Substituting in Eq.(6.7) we obtain the Boltzmann transport equation

$$\left(\frac{\partial}{\partial t} + \frac{p_1}{m} \cdot \nabla_x + F \cdot \nabla_{p_1}\right) f_1 = \int d^3p_2\, d^3p'_1\, d^3p'_2 \delta^4(P_f - P_i)|T_{fi}|^2 (f'_2 f'_1 - f_2 f_1) \tag{6.16}$$

which is a non-linear integro-differential equation for the distribution function.

6.2 Relativistic Transport Equation

In relativistic kinetic theory, macroscopic quantities are defined thanks to a scalar distribution function $f(x, p)$ which depends on space-time coordinates $x = x^\mu = (t, \mathbf{x})$ and four momentum $p = p^\mu = (p^0, \mathbf{p})$ which satisfies the mass-shell relation $p^0 = \sqrt{\mathbf{p}^2 + m^2}$.

The spatial density of Eq.(6.2) is not a Lorentz scalar but it transforms as the time component ($\mu = 0$) of the following four-vector:

$$N^\mu(x) = \int \frac{d^3p}{p^0}\, p^\mu f(x,p) \tag{6.17}$$

while $\mu = 1,2,3$ are the components of the current $\mathbf{j}$. The transport equation derivation in the relativistic case is similar to the classical case except for appropriate formal changes. In the following we will derive the transport equation for a system of N relativistic particles non interacting. In this case the distribution function can be written as:

$$f(x,p) = \sum_{i=1}^{N} \delta^4(x_i(t) - x)\,\delta^4(p_i(t) - p) \tag{6.18}$$

where $x_i(t)$ and $p_i(t)$ coordinates and momenta of the i-th particle at time t.

The time evolution of the phase space density is described by the Liouville Theorem: if there are no dissipative forces, the phase space density is a conserved quantity, i.e. $df(x,p)/dt = 0$.

Using the Liouville theorem, it is possible to obtain the equation of motion for $f(x,p)$:

$$\begin{aligned} \frac{d}{dt} f(x,p) &= \sum_{i=1}^{N} \left[\frac{dx_i^\mu}{dt} \frac{\partial}{\partial x^\mu} + \frac{dp_i^\mu}{dt} \frac{\partial}{\partial p^\mu} \right] \delta^4(x_i(t) - x)\,\delta^4(p_i(t) - p) = \\ &= \left(\frac{p^\mu}{m} \frac{\partial}{\partial x^\mu} + F^\mu(x) \frac{\partial}{\partial p^\mu} \right) f(x,p) \end{aligned} \tag{6.19}$$

where $F^\mu(x)$ represents an external force.

In this way, the condition $df(x,p)/dt = 0$ becomes

$$\left(\frac{p^\mu}{m} \frac{\partial}{\partial x^\mu} + F^\mu(x) \frac{\partial}{\partial p^\mu} \right) f(x,p) = 0 \tag{6.20}$$

Eq.(6.20) is the relativistic *Vlasov equation* which in the classical limit gives the Boltzmann transport equation in Eq.(6.16).

The Vlasov equation can describe systems with conservative forces while it does not permit to take into account dissipative effects. In presence of two body scatterings in fact the phase space density is no more a conserved quantity ($df(x,p)/dt \neq 0$) but changes as a consequence of the collisions. It is possible to derive the equation of motion for $f(x,p)$ adding the collision term $\mathscr{C}[f]$ on the right hand side of Eq.(6.20), where $\mathscr{C}[f]$ has to be specified. Without external forces we have

$$p^{\mu}\partial_{\mu}f(x,p) = \mathscr{C}[f](x,p) \tag{6.21}$$

which is the equation that we solve numerically for the determination of characteristics of the Quark-Gluon Plasma.

A more general expression is obtained by considering the role of an effective mass which allows one to take into account for a mean scalar field. We write below such expression

$$\{p^{\mu}\partial_{\mu} + m^{*}(x)\partial_{\mu}m^{*}(x)\partial^{\mu}\}f(x,p) = \mathscr{C}[f](x,p) \tag{6.22}$$

An equilibrium solution of the Boltzmann equation is the so called Maxwell-Juttner distribution which is the relativistic extension of the Maxwell distribution and is defined as

$$f_{eq} = \exp\left[-\frac{p^{\mu}u_{\mu}(x) - \mu(x)}{T(x)}\right] \tag{6.23}$$

f_{eq} is equal to the classical limit $T \to \infty$ of the Bose and Fermi distributions.

Taking into account only two body collisions the collision integral is denoted by $\mathscr{C}_{22}[f]$. The collision term can be approximated as

$$\mathscr{C}[f] \simeq \frac{f - f_0}{\tau_r} \tag{6.24}$$

where τ_r is the relaxation time of the system, i.e. the time scale required to the system to approach the equilibrium state described by f_0. This is the so called Relaxation Time Approximation.

The explicit expression for the collision integral without approximation in terms of distribution functions is indicated below

$$
\begin{aligned}
\mathscr{C}_{22} = \frac{1}{2E_1}\int \frac{d^3p_2}{(2\pi)^3\,2E_2}\,\frac{1}{\nu}\int \frac{d^3p'_1}{(2\pi)^3\,2E'_1}\frac{d^3p'_2}{(2\pi)^3\,2E'_2}\,f'_1 f'_2 \\
\times |T_{1'2'\to 12}|^2\,(2\pi)^4\,\delta^4(p'_1+p'_2-p_1-p_2)+ \\
-\frac{1}{2E_1}\int \frac{d^3p_2}{(2\pi)^3\,2E_2}\,\frac{1}{\nu}\int \frac{d^3p'_1}{(2\pi)^3\,2E'_1}\frac{d^3p'_2}{(2\pi)^3\,2E'_2}\,f_1 f_2 \\
\times |T_{12\to 1'2'}|^2\,(2\pi)^4\,\delta^4(p_1+p_2-p'_1-p'_2)
\end{aligned}
\qquad (6.25)
$$

where $\nu = 2$ if we are considering indistinguishable particles, otherwise $\nu = 1$. $T_{f\to i}$ is the transition amplitude scattering. The two terms in $\mathscr{C}_{22}$ are respectively the gain term in the phase space considered, due to a collision of type $1'2' \to 12$ which enriches the number of particles in the state 1, while the loss term describes the inverse scattering $12 \to 1'2'$ which brings particles out of the volume of phase space considered.

6.3 Numerical implementation

In this section we discuss the numerical implementation of the Transport equation. In particular we discuss the test-particles method, used to sample the distribution function and to solve the Vlasov equation of sampling the distribution function, and the stochastic method, used to evaluate the collision integral.

6.3.1 Test-particle method

In order to solve the transport equation we use the test particle method, introduced by Wong [112] and used in almost all transport calculations [113][114][115]. The test particle method consists in sampling the phase space distribution function by a large number of test particles. Usually the test particles are chosen point-like, i.e. δ function in coordinate and momentum space,hence the phase space distribution can be written as a sum of the δ test particle distribution:

$$f(x,p,t) = A\sum_{i=1}^{N_{test}} \delta^3(x - x_i(t))\,\delta^3(p - p_i(t)) \tag{6.26}$$

where $x_i(t)$ and $p_i(t)$ are respectively the position and the momentum of the i-th test particle; N_{test} is the total number of test particles while A is a normalization factor that is related to the total number of particles in a way that the integral over the phase space of the distribution function is equal to the total number of particles:

$$\int d^3x \int \frac{d^3p}{(2\pi)^3} f(x,p,t) = \frac{A}{(2\pi)^3} N_{test} = N_{particles} \tag{6.27}$$

where $(2\pi)^3/A$ is equal to the number of test particles per real particles. Once the test particles have been introduced, the solution of the transport equation reduces to solve the classical equation of motion for the test particles. The i-th test particles in momentum space belongs to the mass-shell hypersurface $p^\mu p_\mu = m^2$. It can be shown, using the Liouville theorem, that the phase space distribution given as a collection of point-like test particles is a solution of the Boltzmann-Vlasov equation (6.22) if the positions and momenta of test particle obey the relativistic Hamilton equations

$$\dot{x}_i = \frac{p_i}{E_i}; \qquad \dot{p}_i = -\nabla_x E_i + coll \tag{6.28}$$

where the term $coll$ indicates the effect of the collision integral, whose numerical implementation will be described in the next subsection. The equation of motion that are solved numerically are

$$\begin{aligned} p_i(t+\Delta t) &= p_i(t-\Delta t) - \nabla_x E_i + coll \\ x_i(t+\Delta t) &= x_i(t-\Delta t) - 2\Delta \frac{p_i(t)}{E_i(t)} \end{aligned} \tag{6.29}$$

where index i refers to i-th test particle and Δt is the time discretization. The partonic cascade code we used to perform our tasks is composed of four routines written in FORTRAN programming language.

- The head of the code is a main routine, named i.e. "*cascade*" which reads the input files and calls the other routines which compose the body of the simulation.

- In the "*init*" routine all initial particles spectra in coordinate and momentum space are set up in the centre of mass frame of the system. Test particles of each flavour are randomly sampled in every cell, and their motion and momentum variation can than be followed during the whole simulation.

- In the "*prop*" routine test particle positions and momenta coordinates are changed at each mesh time δt by solving the equation of motion Eqs. (6.28) which are thus numerically implemented like

$$\begin{cases} \vec{p}_i(t+\delta t) = \vec{p}_i(t-\delta t) - 2\delta t \cdot \left(\dfrac{\partial \vec{p}_i}{\partial t}\right)_{coll} \\ \vec{r}_i(t+\delta t) = \vec{r}_i(t-\delta t) - 2\delta t \cdot \left(\dfrac{\vec{p}_i}{E_i(t)}\right) \end{cases}$$

  The jump to the new trajectory point is evaluated by knowing at first the momentum and energy at time t and the variation of their values after a time step δt. A key point of the code operation is that all test particles must satisfy on-shell condition $E_i(t) = \sqrt{|\vec{p}_i(t)|^2 + m_i^2}$ which is checked at every period interval. The variation of particles momentum is evaluated by a third important routine which solves numerically the collision integral $\mathscr{C}[f]$.

- In the "*coll*" routine the numerical implementation of the collision integral $\mathscr{C}[f]$ of Boltzmann equation is pursued. In order to solve numerically the collision integral we make use of the stochastic method employed for the first time by Greiner and Xu in their partonic cascade code BAMPS [23]. In contrast to more widespread algorithms which face the problem of collisions in a geometrical approach and which has been proven not conserve Lorentz covariance entailing a violation in the causality. The stochastic model, instead, appears to be a good algorithm for overcoming such problem, as thoroughly studied in ref.[23].

6.3.2 Simulation of quark dynamics

In this subsection we will discuss the numerical implementation of the collision integral based on the stochastic method. In this method a probability collision P_{22} is associated to pairs of particles: if probability is grater than a random number between 0 and 1 the collision takes place. The P_{22} can be derived from the collision term of the Boltzmann-Vlasov equation. The probability in unit volume $\Delta^3 x$ and unit time Δt can be defined as the ratio between the number of collisions that happen in such volume $\Delta^3 x$ during the time Δt and the total number of pairs present in the same unit volume

$$P_{22} = \frac{\Delta N_{coll}^{2\to 2}}{\Delta N_1 \Delta N_2} \tag{6.30}$$

where $\Delta N_{coll}^{2\to 2}$ coll is simply derived from the collision integral that in discretized form can be written as

$$\begin{aligned} \frac{\Delta N_{coll}^{2\to 2}}{\Delta t \frac{1}{(2\pi)^3} \Delta^3 x \Delta^3 p_1} &= \frac{1}{2E_1} \frac{\Delta^3 p_2}{(2\pi)^3 2E_2} f_1 f_2 \frac{1}{v} \int \frac{d^3 p'_1}{(2\pi)^3 2E'_1} \frac{d^3 p'_2}{(2\pi)^3 2E'_2} \times \\ &\times \; |T_{12\to 1'2'}|^2 (2\pi)^4 \delta^4(p_1 + p_2 - p'_1 - p'_2) \end{aligned} \tag{6.31}$$

Let us introduce the definition of cross section for a particle of mass m_i

$$\sigma_{22} = \frac{1}{4F} \frac{1}{v} \int \frac{d^3 p'_1}{(2\pi)^3 2E'_1} \frac{d^3 p'_2}{(2\pi)^3 2E'_2} |T_{12\to 1'2'}|^2 (2\pi)^4 \delta^4(p_1 + p_2 - p'_1 - p'_2) \tag{6.32}$$

where $F = \sqrt{(p_1 \cdot p_1) - m_1^2 m_2^2}$ is the so called invariant flux and from which the relative particle velocity comes out

$$v_{rel} = \frac{F}{E_1 E_2} = \frac{\sqrt{[s - (m_1 + m_2)^2][s - (m_1 - m_2)^2]}}{2E_1 E_2} \tag{6.33}$$

introducing the Mandelstam variable $s = (p_1 + p_2)^2$ which is equivalent to the square of total centre of mass energy of the collision. Using the definition of cross section the collision rate $\Delta N^{2\to 2}_{coll}$ becomes

$$\Delta N^{2\to 2}_{coll} = \left(\frac{\Delta^3 p_1}{(2\pi)^3} f_1\right)\left(\frac{\Delta^3 p_2}{(2\pi)^3} f_2\right)\Delta^3 x\, \Delta t\, \sigma_{22}\, v_{rel} \tag{6.34}$$

The total number of pair present in a unit volum is given by

$$\Delta N_1 \Delta N_2 = \left(\frac{\Delta^3 p_1 \Delta^3 x}{(2\pi)^3} f_1\right)\left(\frac{\Delta^3 p_2 \Delta^3 x}{(2\pi)^3} f_2\right) \tag{6.35}$$

The definition of probability P_{22}, finally becomes

$$P_{22} = v_{rel}\, \sigma_{22}\, \frac{\Delta t}{\Delta^3 x} \tag{6.36}$$

If one uses the test particle method the probability has to be multiplied by $1/N_{test}$. In the limit $\Delta t \to 0$ and $\Delta^3 x \to 0$, P_{22} is a Lorentz invariant and the stochastic method converges to the exact solution of the Boltzmann equation. The space-time discretization has to be chosen smaller than the typical scales of spatial and temporal inhomogeneities of particles densities. Only particles being in the same cell can collide each other, and the collision probability has to be calculated for each pair inside the cell and compared with a random number extracted between 0 and 1. If the random number is less than the collision probability the collision will occur and the momenta of the particles after the collision is sampled according to the differential cross section. This approach reproduces the proper collisions rate. Strictly speaking, such collisions have not to be considered as real collisions but as a way to map the evolution of the phase space induced by the matrix element $T_{i\to f}$ (sampled stochastically).

6.4 Coalescence

The coalescence model described in 3.4.2 is able to describe well both spectra and ratio at RHIC and LHC, as shown in Chapter 4. Furthermore we have also said that a colescence approach to hadronization can explain the behaviour of particles elliptic flow observed at RHIC. In particular a naïf approximation leads to a perfect quark number scaling (see Eq.3.10). But a more realistic approach to coalescence in three dimensions with radial flow correlations, finite hadronic wave function widths, and resonance decays shows that about a 10% breaking has to be expected at intermediate p_T , and quite a larger one at low p_T. At LHC energy experimental data show a larger breaking of the scaling with respect to the one observed at RHIC or predicted by more realistic coalescence models.

However, we note that these data are based on event-by-event analysis that shows the presence of higher harmonics like v_3, v_4, v_5 which also have a quite large variance. This can be expected to further break the naïf quark number scaling of the $v_2(p_T)$. A quantitative approach to this problem requires an extension of the present model.

The coalescence implementation described so far is obtained by a "freezing snapshot" of our system, all the informations are encoded in a distribution function created by fixing an hypersurface in space-time. Within this approach only averaged or integrated quantities such as the parton transverse momentum distribution and elliptic flow profile in p_T can be taken into account.

These intrinsic limitations do not come from the model itself but are due to implementation.

It is natural, with the purpose of a more realistic and deep analysis, to apply the coalescence model to a Boltzmann Transport Equation, therefore extending our approach to an event-by-event Monte Carlo one.

An approach of this kind can allow new considerations. Such as to study the effect, on final particles, of transport coefficient of QGP, such as shear viscosity, or spacial and time informations that regard particles formation of different species. Moreover this approach can allow one to study the consequence of initial fluctuations in phase-space, or other possible effects due to presence of correlations between particles that are currently ignored, or the effect of space-momentum correlation on the final v_2 of mesons and baryons.

The basic idea is that, when the energy density of a fluid cell drops below the critical energy density value, a freeze-out occurs and all the informations about quarks in that cell, i.e. position, proper time, momentum and energy, are stored and are not allowed to change further. Once the freeze-out occurs for all the test-particles, than the coalescence integral is evaluated.
Fixing the i-est test-particle, probability to coalesce into a test-meson is obtained counting all the j-est test-particle whose coordinates and momenta satisfy the conditions given by the Wigner function widths.
So coalescence integrals in Eqs.(3.28), (3.29) are evaluated with the distributions described in Eq.(6.18) as $P_q(i)$.
The generic meson coalescence integral in Eq.(3.18)

$$\begin{aligned} N_M &= g_M \int p_1 \cdot d\sigma_1 \, p_2 \cdot d\sigma_2 \, \frac{d^3p_1}{(2\pi)^3 E_1} \frac{d^3p_2}{(2\pi)^3 E_2} \\ &\times \; f_q(x_1;p_1) f_{\bar{q}}(x_2;p_2) f_M(x_1,x_2;p_1,p_2) \end{aligned}$$

using Eq.(3.19) becomes

$$\begin{aligned} N_M =& \frac{g_M}{N_{test}^2} \sum_{i,j}^{N_{test}} f_M(x_i,x_j;p_i,p_j) = \\ =& \frac{g_M}{N_{test}^2} \frac{9\pi}{2(\Delta_x \Delta_p)^3} \sum_{i,j}^{N_{test}} \Theta\left(\Delta_x^2 - (x_i - x_j)^2\right) \Theta\left(\Delta_p^2 - (p_i - p_j)^2 + (m_i - m_j)^2\right) \end{aligned} \tag{6.37}$$

The factor $1/N_{test}^2$ in the equation above is necessary to normalize to the real pion number. Proceeding in a similar way we get also the number of baryons produced.

$$
\begin{aligned}
N_B =& \frac{g_B}{N_{test}^3} \sum_{i,j,k}^{N_{test}} f_B(x_i, x_j, x_k; p_i, p_j, p_k) = \\
=& \frac{g_B}{N_{test}^3} \left(\frac{9\pi}{2(\Delta_x \Delta_p)^3} \right)^2 \sum_{i,j}^{N_{test}} \Theta\left(\Delta_x^2 - \frac{1}{2}(x_i - x_j)^2 \right) \Theta\left(\Delta_p^2 - \frac{1}{2}(p_i - p_j)^2 \right) \\
& \times \Theta\left(\Delta_x^2 - \frac{1}{6}(x_i + x_j - 2x_k)^2 \right) \\
& \times \Theta\left(\Delta_p^2 - \frac{1}{6}\left[(p_i + p_j - 2p_k)^2 - (m_i + m_j - 2m_k)^2 \right] \right)
\end{aligned}
\tag{6.38}
$$

We can also obtain the mesons and baryons momenta distribution since we have all the informations about momenta, rapidity and position.

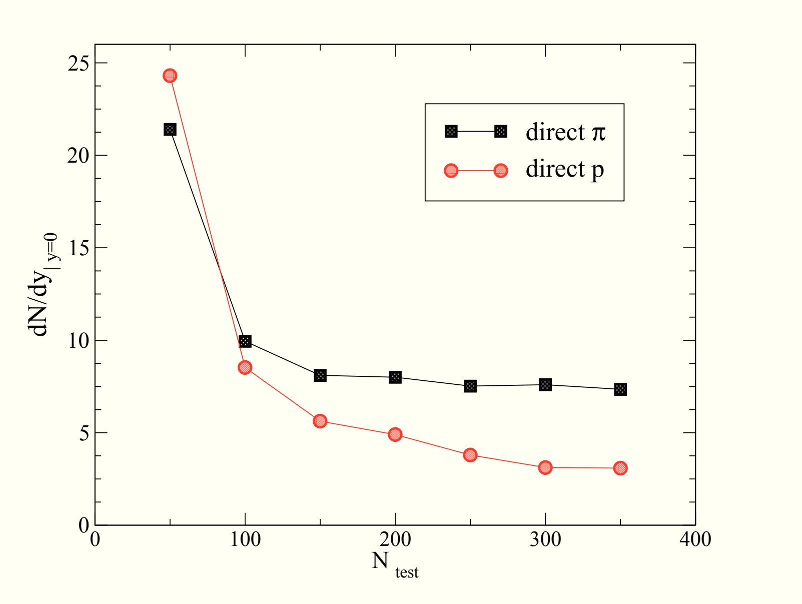

Figure 6.1: Pions and protons multiplicity at zero rapidity for different values of N_{test}

After numerical implementation, it is important to check if results converge varying the number of test-particles used to sample the phase space. In Fig.6.1 are shown the multiplicity dN/dy with $y = 0$, as a function of test-particle number. We can see a satisfying stability in the number of pions (black squares) and protons (red circles) produced for

n_{test} values around 300.

Another interesting test is the percentage of particles subjected to freeze-out with respect to the total number of particles. As shown in Fig.6.2 RHIC and LHC have a different lifetime of the fireball. Where at RHIC energies at $5-6\, fm/c$ the percentage of particle available for the hadronization is almost the total number. A different time can be needed to reach a satisfying percentage when the system dimensions change, as shown by the LHC energies where in this case we have that the lifetime is about $9-10\, fm/c$. Hence this quantity is affected by the system size, and can change varying the energy density at which hadronization occurs. An higher value of freeze-out energy density is expected to give a faster rise in the in the number of particle subjected to freeze-out.

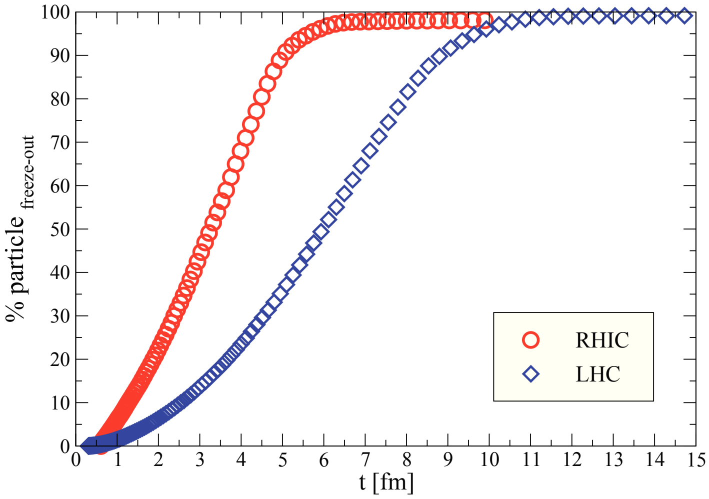

Figure 6.2: Percentage of test particles subjected to freeze-out for a single quark flavour at RHIC (red circles) and at LHC (blue diamond)

6.4.1 Results

Some preliminary results about pions, kaons and protons transverse momentum distribution in $Au+Au$ collision $\sqrt{s}=200\,GeV$ at centrality $0-5\%$ are shown in this section. In our calculation the initial conditions

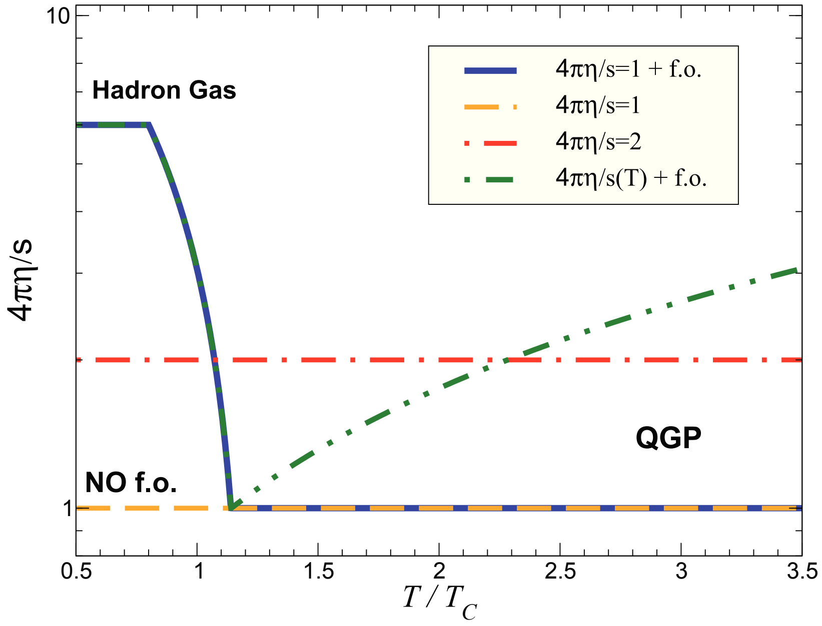

Figure 6.3: Different η/s parametrization as a function of T/T_c

are longitudinal boost invariant with the initial parton density $dN/dy =$ 1400 (2500) at RHIC (LHC). The partons are initially distributed in coordinate space according to the Glauber model while in the momentum space we have a thermalized spectrum with a maximum temperature in the center of the fireball $T = 340\ MeV = 2T_c$ at RHIC and $T = 510\ MeV = 3T_c$ at LHC. We have massive quarks, with masses set at $m_{u,d,\bar{u},\bar{d}} = 330\ MeV$ and $m_{s,\bar{s}} = 450\ MeV$, as used in the previous model. We start our simulation at $t_0 = 0.6\ fm/c$ at RHIC and at $t_0 = 0.3\ fm/c$ in the LHC case, similarly to hydrodynamical initial conditions.

We have performed calculations with two values for the viscosity, $4\pi\eta/s =$ 1 (dashed orange line in Fig.6.3) and $4\pi\eta/s = 2$ (dot-dashed red line) and the viscosity is maintained fixed during the whole evolution of the system. Moreover we have performed simulations with an η/s that changes with temperature and assumes a value $1/4\pi$ in QGP phase and increases in the cross over region towards the estimated value for hadronic matter $4\pi\eta/s = 6$, this case is depicted in Fig.6.3 by solid blue line. Another case, shown by double dotted-dashed green line, has been considered in which the viscosity in the QGP phase is expected to have a minimum of $4\pi\eta/s = 1$ close to T_c, while at high temperature $\eta/s \propto T$ as suggested by quasi-particle models [105].

The spectra obtained are comprehensive of contributions that come from resonance decays with the same method discussed in Chapter 4.

In Fig.6.4 the pion spectrum at viscosity $4\pi\eta/s = 1$ and all the contributions from resonances decay are shown for $Au+Au$ collision $\sqrt{s} = 200\,GeV$ at centrality $0-5\%$ in comparison with data by PHENIX [78] [79]. We find a really good agreement in the intermediate transverse momentum region. There is a lack of yield in the region below $p_T \sim 1\,GeV$. This region, as said in Chapter 4, is dominated by the resonances and in this calculation we take into account only pion coming from ρ, K* and Δ.

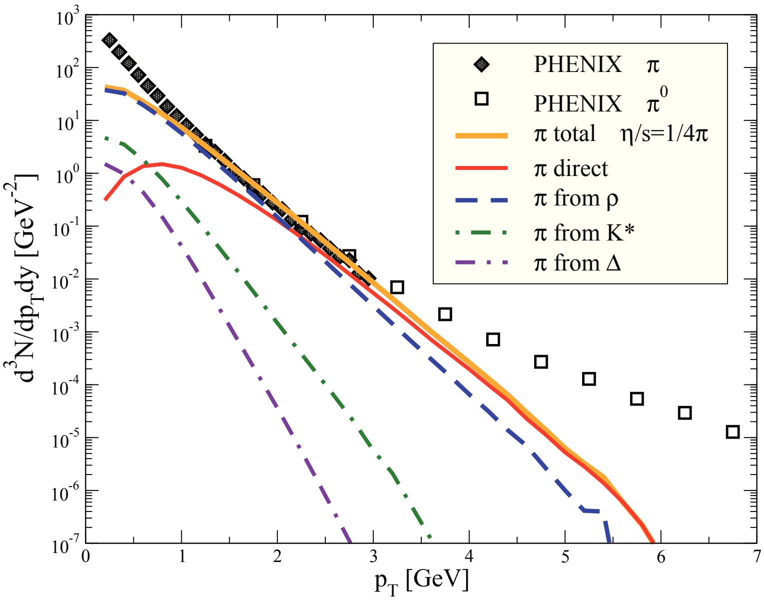

Figure 6.4: Pion transverse momentum distribution at viscosity $4\pi\eta/s = 1$ including contribution from resonances in $Au+Au$ collision $\sqrt{s} = 200\,GeV$ at centrality $0-5\%$, data by PHENIX [78] [79]. Direct pions are shown by the solid red line, pions from ρ resonance are indicated by the dashed blue line, pions from K* are the dot-dashed green line and pions from Δ are shown by the double dashed-dot violet line. The total pion spectrum is shown by the solid orange line

In Fig.6.5 pions, kaons and protons spectra at viscosity $4\pi\eta/s = 1$, inclusive of all the contributions from resonances decay are depicted for $Au+Au$ collision $\sqrt{s} = 200\,GeV$ at centrality $0-5\%$, in comparison with PHENIX [78] [79] and STAR [80] data. The dashed lines represent the contribution from the fragmentation, such contribution became relevant for momenta higer than $3\,GeV$ since in the region at lower momenta coalescence is the predominant hadronization mechanism. The final fragmentation hadronic spectrum comes from

$$\frac{dN_H}{d^2p_T} = \int_0^1 dx\, x \sum_f \frac{dN_f}{d^2p_T} D_f^H(x,Q^2) \tag{6.39}$$

where $x = p_T^H/p_T^f$ is the fraction of the f parton carried by the hadron H and $Q = p_T^f/2$ is the energy scale, and dN_f/d^2p_T are the spectra obtained from the parton Boltzmann Transport Equation.

The thick solid lines are the sum of coalescence and fragmentation

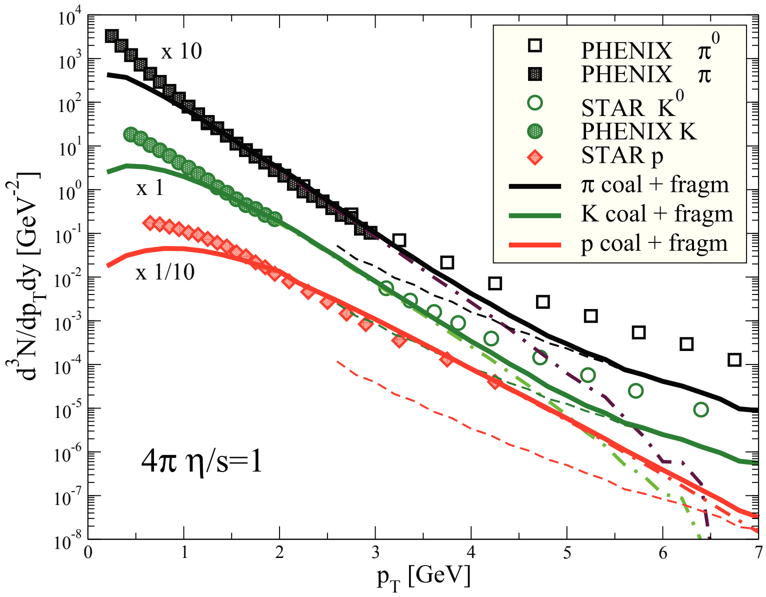

Figure 6.5: Total pion, proton and kaon spectra in $Au+Au$ collision $\sqrt{s} = 200\,GeV$ at centrality $0-5\%$. Data are from PHENIX [78] [79] and STAR [80] experiment

distribution. As already discussed our results describe reasonably well the region at low and intermediate momenta, while for higher momenta ($p_T > 4-5\,GeV$) we underestimate the experimental data, however this is not due to the hadronization process but it has to be ascribed to the partonic spectrum, that is oversuppressed in the region at high p_T. In fact our approach of fixing the viscosity to get the interaction is effective to reproduce the correct dynamics in the low momentum region ($p_T < 4\,GeV$), but overestimates the interaction for higher momenta. Moreover one ingredient which is necessary to describe this region of momenta, i.e. the radiative mechanism, have not been taken into account in the present Boltzmann transport approach.

The total distribution obtained by the sum of coalescence and fragmentation are represented by the solid thick lines, we can see how also for kaons and protons our results are in good agreement with the experimental data.

In Fig.6.6 pions, kaons and protons spectra at viscosity $4\pi\eta/s = 1$, inclu-

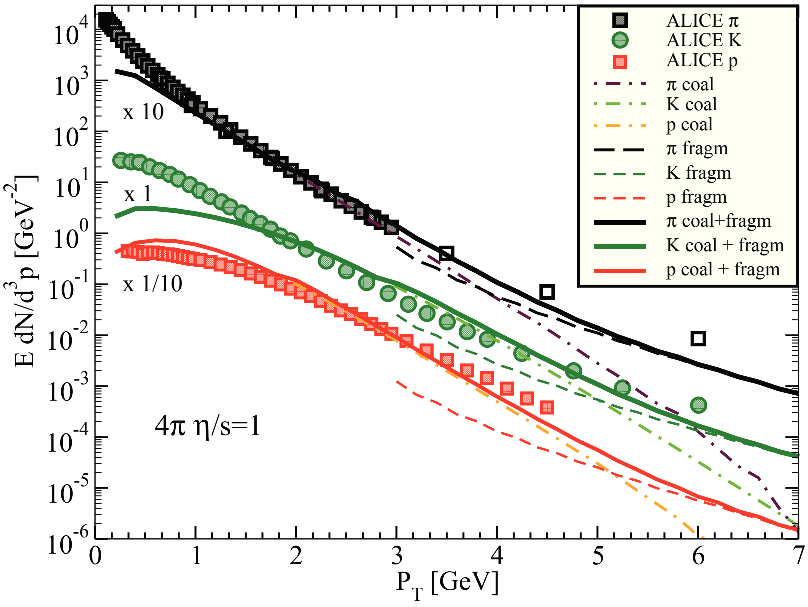

Figure 6.6: Total pion, proton and kaon spectra in $Pb+Pb$ collision $\sqrt{s} = 2.76\,TeV$ at centrality $0-5\%$. Data are from ALICE experiment [84–87]

sive of all the contributions from resonances decay and fragmentation are shown for $Pb+Pb$ collision $\sqrt{s}=2.76\,TeV$, in comparison with ALICE experiment [84–87] data. Also at LHC energy our results give a good description of experimental data, similar to RHIC case we have a lack of yield in the low momentum region due to missing of all resonances contribution.

It is interesting to investigate the effect of shear viscosity to entropy density ratio.
In Fig.6.7 we show pion spectra obtained with different values of viscosity. Viscosity temperature dependence leads to not negligible differences in the spectra, especially in the region of intermediate and high momentum. It is interesting to note that in this approach coalescence give an higher production in a zone that is dominated by fragmentation.
In Fig.6.8 are shown pion spectra with different viscosity for $Pb+Pb$

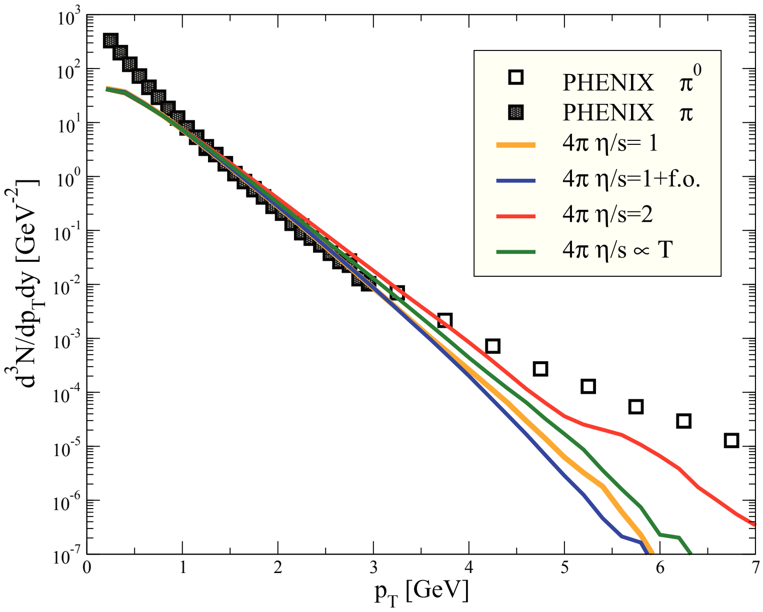

Figure 6.7: Total pion spectra for different η/s scenarios dependence in $Au+Au$ collision $\sqrt{s}=200\,GeV$ at centrality $0-5\%$

collision $\sqrt{s}=2.76\,TeV$ at centrality $0-5\%$. As shown we have a good description of the experimental data, for viscosity $4\pi\eta/s\sim 2$ which is a

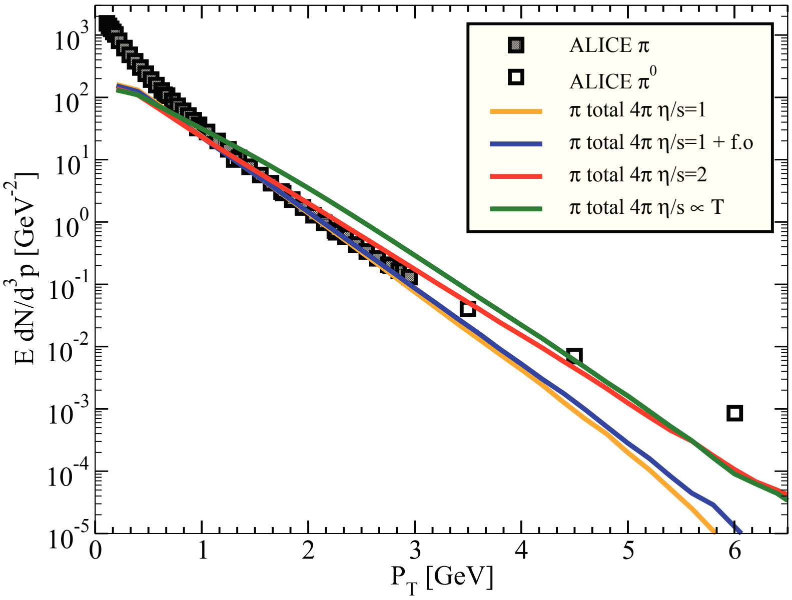

Figure 6.8: Total pion spectra for different η/s scenarios dependence in $Pb+Pb$ collision $\sqrt{s} = 2.76\,TeV$ at centrality $0-5\%$ ALICE experiment [84] [85]

factor two larger than the η/s extracted at RHIC energies. Therefore the comparison between our results with experimental data at RHIC and LHC suggest that they are consistent with a temperature dependent η/s in agreement with the one obtained by viscous hydrodynamical calculations [116].

In order to study the effect of the kinetic freezeout on the generation of the elliptic flow we have performed three kind of calculations that are shown in Fig.6.9, one with a constant $4\pi\eta/s = 1$ during all the evolution of the system (orange line), another with $4\pi\eta/s = 2$ (red solid line), and the last one with $\eta/s \propto T$ at higher temperature and an increasing η/s in the cross over region towards the estimated value for hadronic matter $4\pi\eta/s = 6$ (green solid line).

In a similar way as observed in previous studies [117], the effect of η/s ratio is a reduction of the elliptic flow of pions of about 10% for both energies. In fact at RHIC energies, the life time of the fireball is smaller

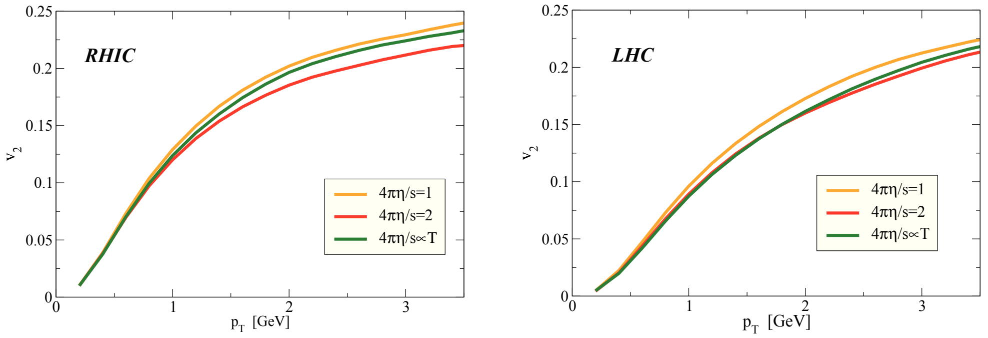

Figure 6.9: Differential $v_2(p_T)$ at midrapidity and for (20-30)% collision centrality. The comparison is between the two systems: $Au+Au$ at $\sqrt{s}=200\,GeV$ (left) and $Pb+Pb$ at $\sqrt{s}=2.76\,TeV$ (right). The orange line refer to the case with a constant $4\pi\eta/s=1$ during all the evolution. The red lines refer to the case with $4\pi\eta/s=2$ while the green lines refer to the case with$\eta/s\propto T$ at higher temperature and with an increasing η/s ratio at lower temperature.

than that at LHC energies, that are approximatively 5 fm/c at RHIC and about $9-10\,fm/c$ at LHC (see Fig.6.2).

As a consequence at RHIC the elliptic flow has not enough time to fully develop in the QGP phase. Whereas at LHC we have that the v_2 can develop almost completely because the fireball spend more time in the QGP phase.

As we can see in Fig.6.9, at RHIC the pion elliptic flow is essentially not sensitive to the dependence of η/s on temperature in the QGP phase (see Fig.6.3), in fact in the left panel, the line with $4\pi\eta/s=1$ (orange) and the line with η/s with temperature dependence (green) are very close.

At LHC energies the build-up of v_2 is more affected by the η/s in the QGP phase and on average it is reduced of about a 10% and tends to the line at higher viscosity.

In Fig. 6.10 and Fig.6.11 we compare the elliptic flow of pions at midrapidity for 20-30% centrality class with the experimental data from PHENIX [118] and ALICE[119](open circles).

In the figures are shown the elliptic flow of pions produced via coalescence (orange solid line), the v_2 at partonic level (green dashed line), and the elliptic flow obtained with both coalescence and fragmentation

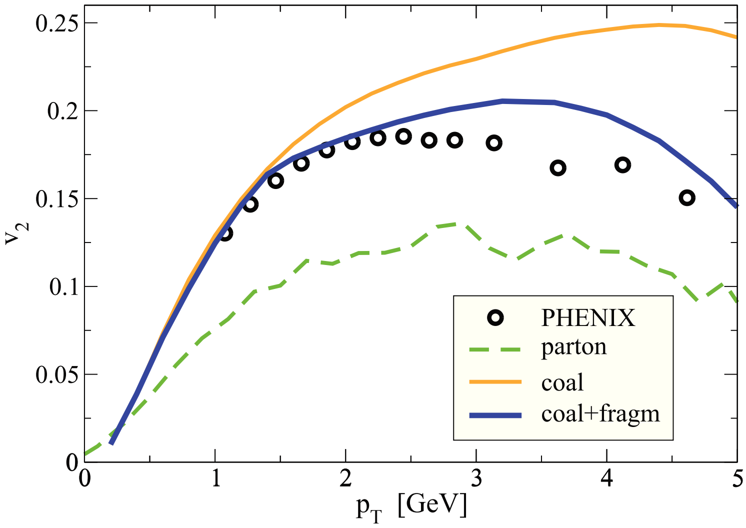

Figure 6.10: Elliptic flow of pions in function of transverse momentum in Au+Au collisions at $\sqrt{s} = 200\,GeV$. Elliptic flow of partons is given by the dashed green line. The solid orange line shown the elliptic flow of pion produced by coalescence. The solid blue line represent the elliptic flow obtained with both coalescence and fragmentation. Experimental data by PHENIX experiment are shown by circle[118]

(blue solid line).

The comparison with experimental data of the elliptic flow obtained with only coalescence overestimate the v_2 observed experimentally in the momentum region above $2\,GeV$, on the other hand the elliptic flow of partons is about two times smaller than the experimental data.

As said before the fragmentation process play a relevant role in the region at higher momenta ($p_T > 3\,GeV$), therefore in order to get the elliptic flow of pion at high p_T it is necessary to take into account the contribution due to the fragmentation process. Assuming that the particle produced by the fragmentation are emitted collinearly with respect to the initial direction of the initial parton, thus the elliptic flow of the produced hadrons will results substantially unchanged with respect to the partonic elliptic flow. The final elliptic flow is given by the weighted average of partonic and coalescence elliptic flow where the weight is the transverse momentum distribution.

Our model is the first attempt to combine a microscopic partonic approach with a coalescence model, this at difference with the other coalescence models allow us to evaluate the elliptic flow while in standard approaches the partonic v_2 is just an input determined to reproduce the pion one and predict the elliptic flow of other hadrons and in particular of baryons. Although the elliptic flow that we obtain does not exactly reproduce the experimental data it gives important indication that an approach in which the elliptic flow is obtained only via coalescence overestimates the experimental data, on the other hand in the region of intermediate momentum the elliptic flow of the partonic medium is substantially below the experimental data. Instead a model that take in account of both coalescence and fragmentation is able to give a reasonable description of the elliptic flow behaviour in a quite large range of momenta.

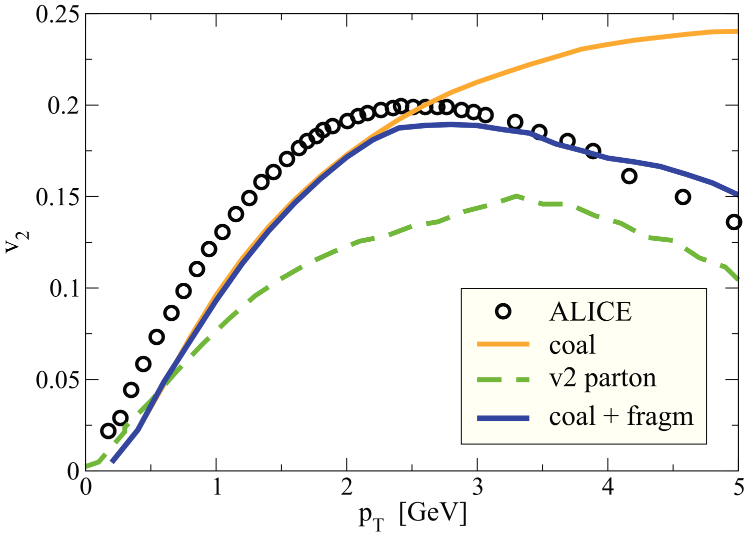

Figure 6.11: Elliptic flow of pions in function of transverse momentum in Pb+Pb collisions at $\sqrt{s} = 2.7 TeV$. Elliptic flow of partons is given by the dashed green line. The solid orange line shown the elliptic flow of pion produced by coalescence. The solid blue line represent the elliptic flow obtained with both coalescence and fragmentation. Experimental data by ALICE [119] experiment are shown by circle.

Ultimately, preliminary study about the implementation of a coalescence approach to hadronization coupled to a Transport Equation seems to give satisfying results in the description of final particle momentum distribution. We note that the approach developed will allow in the upcoming future to investigate the quark number scaling of the elliptic flow in a coalescence approach that is at an higher level of sophistication. In fact the coupling of hadronization to distribution function coming from realistic simulation allows to study the impact of realistic hypersurface and event-by-event fluctuations of a naïf quark number scaling. This would provide an appropriate framework to scrutinize the sources of the quark number scaling violations observed experimentally at LHC energy.

CONCLUSIONS AND OUTLOOKS

In this thesis we have developed a numerical code to implement an hadronization model based on a quark coalescence mechanism.
Our first purpose has been to reproduce the transverse momentum spectra and the particle ratio at RHIC and LHC for pions, kaons, protons and Lambda with an implementation based on a coalescence model applied for a fixed hyper-surface. At RHIC, we obtain a good description of transverse momentum spectrum in the whole range of momenta. At low momenta we show that the coalescence process is dominant, and we have seen that in the region below $1\,GeV$ a significant contribution comes from the decay of the resonance produced. Instead the fragmentation from minijets becomes dominant in the region of higher momenta. For the intermediate transverse momentum, between 3 and $5\,GeV$, the two contribution are comparable and combining both coalescence and fragmentation hadronization process results necessary for a correct description of the experimental data.
Furthermore our model reproduces experimental data for both proton to positive pion ratio and Lambda to kaons ratio specially in the inter-

mediate transverse momenta region where an anomalous large value is observed. The features of these ratios was one component of the so-called "baryonic puzzle".

We can see that the ratio is quite well predicted in its rise at low transverse momenta up to the peak region as well as in the falling-down region. However in both cases it is clear that in the region of $p_T \approx 5{-}7\,GeV$ there is a lack of baryon yield.

We find a good agreement of the transverse momentum distribution at LHC, the model is able to correctly predict the evolution of the absolute yield and especially its p_T shape correctly, is important to notice that no parameter of the coalescence process has been modified with respect to those used for RHIC. In the p_T region where the fragmentation starts to dominate, $p_T \simeq 6-7\,GeV$ there is some lack of yield. At both RHIC and LHC such a lack of yield appears where coalescence becomes less important therefore one can say that it seems that the spectrum from AKK fragmentation function appears too flat. It is likely that studies of in-medium fragmentation function, with the idea to describe the in-medium fragmentation as a quark recombination of shower partons taking into account also the gluon splitting into quark pairs that recombine, can solve it or it could be that coalescence contribution should extend to large p_T with respect to the present modelling.

The baryon to meson ratios at LHC present similar features of that at RHIC, but with a shift in the peak of about $0.5\,GeV$, and this is well predicted by our coalescence plus fragmentation model, most of the disagreement with the data comes from the lack of yield in the distribution from fragmentation that, as said, appears too soft in this p_T range.

Ultimately we show also the ϕ meson spectra, it is often discussed whether the p_T spectra of ϕ meson would have a slope close to the one of the proton like in a hydropicture or would behave like other mesons being formed by two quarks. We briefly mention that indeed also in a coalescence process one can and should expect that there is a radial flow mass effect like in a hydropicture. In fact for a proton there is a combination of three quarks flowing each with a mass of about $330\,MeV$ while for a ϕ meson there are two quarks flowing each with a mass of about $550\,MeV$. We can see that as for the other ratios we have quite good agreement with the data.

Then we have studied the hadronization effect with a coalescence model applied in the heavy quark sector. At both RHIC and LHC energies the relation between Heavy Quarks nuclear modification factor R_{AA} and the elliptic flow v_2 observed which indicate a quite strong interactions between heavy quarks and the medium which is substantially beyond the expectations coming from perturbative QCD. Several theoretical efforts have been made to reproduce the R_{AA} and the v_2 observed in experiments but all the approaches show some difficulties to describe them simultaneously.

Comparing the D meson nuclear modification factor obtained considering only fragmentation with results for R_{AA} obtained including coalescence mechanism we can observe that coalescence implies an increasing of R_{AA} for momenta larger than $1\,GeV$, thus a reduction of the suppression. The impact of coalescence decreases with transverse momentum because at higher p_T the D meson spectrum is dominated by the fragmentation mechanism of hadronization. At the same time coalescence gives a D meson elliptic flow that is larger than charm quark elliptic flow. We obtain analogous results at both RHIC and LHC, but at LHC the final effect of coalescence is smaller in magnitude.

A key result which emerges from our study is that in order to get the same R_{AA} that we have without including coalescence is necessary to further increase the interaction, which causes an additional increase of the elliptic flow. Coalescence inverts this relation, implying a contemporary increase of both these two observables and this is fundamental to reproduce the experimental data.

In the final part we have presented a more realistic implementation of coalescence model, in which we have developed a model self-consistently applied to the freeze-out hypersurface of a Boltzmann Transport equation. Comparing the transverse momentum distribution of pions, kaons and protons with the experimental data at RHIC and LHC we find a really good agreement in the intermediate transverse momentum region. While for higher momenta we slightly underestimate the experimental data, however this can be ascribed to the partonic spectrum that results over-suppressed in the region at high p_T.

Finally we have studied the elliptic flow for pions and we have obtained that the coalescence overestimate the v_2 observed experimentally in the momentum region above $2\,GeV$, on the other hand in the same region the elliptic flow of fragmentation is about two times smaller than the experimental data. But the final elliptic flow is given by the weighted average of fragmentation and coalescence elliptic flow and although the elliptic flow that we obtain does not exactly reproduce the experimental data it gives important indication that an approach that take in account of both coalescence and fragmentation is able to give a reasonable description of the elliptic flow behaviour in a quite large range of momenta.

The results of our work can be a starting point for further investigations. We note that the approach developed will allow in the upcoming future to investigate the quark number scaling of the elliptic flow in a coalescence approach that is at an higher level of sophistication. In fact the coupling of hadronization to distribution function coming from realistic simulations will allow to study the impact of realistic hypersurface. In particular it will be possible to study the role of the initial state fluctuations on the final anisotropic flows of hadrons (π,p, k, ...) extending the possibility to study the higher order harmonics like v_3, v_4, v_5 that can be expected to break the naive quark number scaling of the $v_2(p_T)$. This provides an appropriate framework to scrutinize the sources of the quark number scaling violations observed experimentally at LHC energy.

APPENDIX

Appendix A: Dirac Matrices

Dirac γ matrices satisfy

$$\{\gamma^\mu, \gamma^\nu\} \equiv \gamma^\mu \gamma^\nu + \gamma^\nu \gamma^\mu = 2\eta^{\mu\nu}$$

Therefore $\gamma_0^2 = 1$ and, for each i, $(\gamma^i)^2 = -1$; γ^0 is hermitian while, for each i, γ^i is antihermitian,

$$(\gamma^0)^\dagger = \gamma^0, \qquad (\gamma^i)^\dagger = -\gamma^i$$

or, more compactly, $(\gamma^\mu)^\dagger = \gamma^0 \gamma^\mu \gamma^0$.

The matrix γ^5 is defined as

$$\gamma^5 = +i\gamma^0\gamma^1\gamma^2\gamma^3,$$

and satisfies

$$(\gamma^5)^2 = 1, \qquad (\gamma^5)^\dagger = \gamma^5, \qquad \{\gamma^5, \gamma^\mu\} = 0.$$

Two particularly useful representations of the γ matrix algebra are

$$\gamma^0 = \begin{pmatrix} 0 & 1 \\ 1 & 0 \end{pmatrix}, \qquad \gamma^i = \begin{pmatrix} 0 & \sigma^i \\ -\sigma^i & 0 \end{pmatrix}, \qquad \gamma^5 = \begin{pmatrix} -1 & 0 \\ 0 & 1 \end{pmatrix}$$

(here 1 denotes the 2 × 2 identity matrix), which is called the chiral or Weyl representation, and

$$\gamma^0 = \begin{pmatrix} 1 & 0 \\ 0 & -1 \end{pmatrix}, \qquad \gamma^i = \begin{pmatrix} 0 & \sigma^i \\ -\sigma^i & 0 \end{pmatrix}, \qquad \gamma^5 = \begin{pmatrix} 0 & 1 \\ 1 & 0 \end{pmatrix}$$

which is called the ordinary, or standard, representation.

The Pauli matrices (σ^i) are

$$\sigma^1 = \begin{pmatrix} 0 & 1 \\ 1 & 0 \end{pmatrix}, \qquad \sigma^2 = \begin{pmatrix} 0 & -i \\ i & 0 \end{pmatrix}, \qquad \sigma^3 = \begin{pmatrix} 1 & 0 \\ 0 & -1 \end{pmatrix}$$

and satisfy

$$\sigma^i \sigma^j = \delta^{ij} + i\epsilon^{ijk}\sigma^k.$$

Appendix B: Laboratory frame and centre-of-mass frame

Consider the following reaction with a two-body initial state:

$$a + b \to c + d + e + ...$$

and call a the projectile and b the target particle. In the *laboratory frame* the target is at rest and the projectile strikes it with an energy E^{lab} and a momentum p^{lab}. After the collision, the particles in the final state, $c, d, e, ...$, are usually moving. In the *center-of-mass frame*, which actually means the *center-of-momentum frame*, the sum of the momentum vectors of all particles in the initial state and that in the final state vanish. Namely, the two frames are defined as follows:

- Laboratory frame

$$p_b^{lab} = 0, \qquad E_b^{lab} = m_b$$

- Centre of mass frame

$$p_a^{cm} + p_b^{cm} = p_c^{cm} + p_d^{cm} + p_e^{cm} + ... = 0$$

where m_b is the rest mass of particle b. In the center-of-mass frame, both particles, a and b, in the initial state approach each other with equal but opposite momentum. Only the energy available in the center-of-mass frame can be used to produce new particles or to excite internal degrees of freedom. In order to obtain the relation between the energies in the laboratory and center-of-mass systems, we utilize Lorentz invariance. We define the following Lorentz scalar quantity, s, which is one of the Mandelstam variables:

$$s \equiv (p_a + p_b)^2 \equiv (p_a + p_b)_\mu (p_a + p_b)^\mu$$

where p_a (p_b) is the four-momentum of the particle a (b). By definition, s, is the same in all coordinate systems.

Consider a relativistic collision between two particles with the same rest mass m, using the equations above, we obtain

- Laboratory frame

$$\begin{aligned} p_a^{lab} &= (E^{lab}, p^{lab}) \\ p_b^{lab} &= (m, 0) \\ s &\equiv (p_a + p_b)^2 = (p_a^{lab} + p_b^{lab})^2 \\ &= (E^{lab} + m)^2 - (p^{lab})^2 = (E^{lab} + m)^2 - [(E^{lab})^2 - m^2] \\ &= 2mE^{lab} + 2m^2 \end{aligned}$$

- Centre of mass frame

$$\begin{aligned} p_a^{cm} &= (E^{cm}/2, p^{cm}) \\ p_b^{cm} &= (E^{cm}/2, -p^{cm}) \\ s &\equiv (p_a + p_b)^2 = (p_a^{cm} + p_b^{cm})^2 = (E^{cm})^2 \end{aligned} \tag{6.40}$$

and we obtain

$$E^{lab} = \frac{(E^{cm})^2}{2m} - m$$

With $E^{lab} \gg m$, which corresponds to an extremely relativistic or ultra-relativistic case, the energy $E^{cm} (= \sqrt{s})$ becomes

$$\sqrt{s} = E^{cm} \simeq \sqrt{2mE^{lab}}$$

This equation shows that the centre of mass energy which is useful for producing new particles increases only as the square root of the laboratory energy in relativistic energies. This is the reason why we have to construct relativistic collider-type accelerators.

Appendix C: Rapidity and pseudo rapidity

In relativistic mechanics, the addition law of the velocities moving along, for example, the z-axis is non-linear:

$$v = \frac{v_1 + v_2}{1 + \frac{v_1 v_2}{c^2}} \qquad \text{or} \qquad \beta = \frac{\beta_1 + \beta_2}{1 + \beta_1 \beta_2}$$

where $\beta = v/c$. Let us introduce a function $y \equiv y(\beta)$ so as to make the addition law of y linear in y.
Recalling the following addition law:

$$\tanh^{-1} \beta_1 \pm \tanh^{-1} \beta_2 = \tanh^{-1} \frac{\beta_1 \pm \beta_2}{1 \pm \beta_1 \beta_2}$$

we obtain

$$y = \tanh^{-1} \beta = \frac{1}{2} \ln \frac{1+\beta}{1-\beta}$$

which we call *rapidity*.
For small β, we have $y \simeq \beta$; i.e., the rapidity is a relativistic analogue of the velocity. The rapidity increases without bound as the particle velocity approaches the velocity of light. Since $\beta = p_z/E$, the rapidity may also be expressed as follows:

$$y = \tanh^{-1} \beta = \frac{1}{2} \, ln \frac{E + p_z}{E - p_z}$$

where p_z indicates the momentum along the z-axis (longitudinal momentum).

A Lorentz boost along the longitudinal axis from a frame **S** to a new frame **S**′ thus changes the rapidity in a simple additive way:

$$y' = y' + \tanh^{-1} \beta$$

where β is the velocity of **S**′ with respect to **S**. Consequently, a particle distribution expressed as a function of y has a shape that is invariant under such a boost.

The transverse momentum, p_T and the longitudinal momentum, p_z of a particle having rest mass m and momentum vector $p = (P_x, p_y, p_z)$ are given by

$$p_T = \sqrt{p_x^2 + p_y^2} = |p| \sin\theta, \qquad p_z = |p| \cos\theta$$

where θ is the polar angle of the vector $\boldsymbol{p}$ with respect to the z-axis. By using these variables we define the transverse mass, m_T , as

$$m_T^2 = p_T^2 + m^2, \qquad E^2 = p_z^2 + m_T^2$$

Then the rapidity can be rewritten as follows

$$y = \ln \frac{E + p_z}{m_T}$$

The four-momentum, p^μ, and the space-time coordinates are thus conveniently parametrized as

$$\begin{aligned} p^\mu = (E, p_x, p_y, p_z) &= (m_T \cosh y, p_T \cos\phi_p, p_T \sin\phi_p, m_T \sinh y) \\ &= (m_T \cosh y, p_T, m_T \sinh y) \\ x^\mu = (t, x, y, z) &= (\tau \cosh\eta, r_T, \tau \sinh\eta) \end{aligned}$$

with τ the proper time, and r_T the transverse coordinates.

This parametrization is valid also for an off-shell time-like particle if we define $m^2 = p^2$.

Next we define the pseudo-rapidity

$$\eta \equiv -\ln\left(\tan\frac{\theta}{2}\right).$$

If the particle masses are negligible, i.e. $E^2 = p^2 + m^2 \simeq p^2$, we

$$y \simeq \frac{1}{2} \ln \frac{p + p_z}{p - p_z} = \frac{1}{2} \ln \frac{1 + \cos\theta}{1 - \cos\theta} = -\ln\left(\tan\frac{\theta}{2}\right) = \eta$$

Therefore, at extremely high energies ($E \gg m$), the rapidity, and the pseudorapidity are equivalent. The pseudo-rapidity is useful because it can be determined directly from the particle production angle, θ, measured with respect to the beam axis in experiments.

BIBLIOGRAPHY

[1] Y. Nambu, in *"Preludes in Theoretical Physics: in honor of V.F. Weisskopf"*, edited by H. Feshbach A. de Shalit and L. van Hove. (North-Holland Publishing Company, Amsterdam, 1966).

[2] Chen-Ning Yang and Robert L. Mills, Phys.Rev. **96**, 191 (1954).

[3] D.J. Gross and Frank Wilczek, Phys.Rev.Lett. **30**, 1343 (1973).

[4] H. David Politzer, Phys.Rev.Lett. **30**, 1346 (1973).

[5] Kenneth G. Wilson, Phys.Rev. **D10**, 2445 (1974).

[6] K. Yagi, T. Hatsuda, and Y. Miake, *"Quark-Gluon Pasma, From Big Bang to Little Bang"* (Cambridge University Press, Cambridge, 2005).

[7] Sidney R. Coleman and David J. Gross, Phys.Rev.Lett. **31**, 851 (1973).

[8] Y. Nambu and G. Jona-Lasinio, Phys. Rev. **122**, 345 (1961).

[9] A. Friedman, Zeitschrift fur Physik **10**, 377 (1922).

[10] Edwin Hubble, Proc.Nat.Acad.Sci. **15**, 168 (1929).

[11] Arno A. Penzias and Robert Woodrow Wilson, Astrophys.J. **142**, 419 (1965).

[12] A. Hewish, S.J. Bell, J.D.H Pilkington, P.F. Scott, and R.A. Collins, Nature **217**, 709 (1968).

[13] J.R. Oppenheimer and G.M. Volkoff, Phys.Rev. **55**, 374 (1939).

[14] I. Arsene et al., Nucl.Phys. **A757**, 1 (2005).

[15] B.B. Back, M.D. Baker, M. Ballintijn, D.S. Barton, B. Becker, et al., Nucl.Phys. **A757**, 28 (2005).

[16] John Adams et al., Nucl.Phys. **A757**, 102 (2005).

[17] K. Adcox et al., Nucl.Phys. **A757**, 184 (2005).

[18] J.D. Bjorken, Lect.Notes Phys. **56**, 93 (1976).

[19] E. Iancu and R. Venugopalan, in *"Quark-Gluon Plasma 3"*, edited by R. C. Hwa and X. N. Wang. (World Scientific, Singapore, 2004).

[20] Michael L. Miller, Klaus Reygers, Stephen J. Sanders, and Peter Steinberg, Ann.Rev.Nucl.Part.Sci. **57**, 205 (2007).

[21] S.S. Adler et al., Phys.Rev. **C71**, 034908 (2005).

[22] Cheuk-Yin Wong, *"Introduction ti High-Energy Heavy-Ion Collisions"* (World Scientific, Singapore, 1994).

[23] Zhe Xu and Carsten Greiner, Phys.Rev. **C71**, 064901 (2005).

[24] F. Scardina, M. Colonna, S. Plumari, and V. Greco, (2012).

[25] L. Van Hove, Phys.Lett. **B118**, 138 (1982).

[26] Johann Rafelski, Phys.Rept. **88**, 331 (1982).

[27] Johann Rafelski and Berndt Muller, Phys.Rev.Lett. **48**, 1066 (1982).

[28] P. Koch, Berndt Muller, and Johann Rafelski, Phys.Rept. **142**, 167 (1986).

[29] T. Matsui and H. Satz, Phys.Lett. **B178**, 416 (1986).

[30] C. Pinkenburg et al., Phys.Rev.Lett. **83**, 1295 (1999).

[31] C. Adler et al., Phys.Rev.Lett. **87**, 182301 (2001).

[32] K.H. Ackermann et al., Phys.Rev.Lett. **86**, 402 (2001).

[33] Peter F. Kolb and Ulrich W. Heinz, in *"Hydrodynamic description of ultrarelativistic heavy ion collisions. Invited review for Quark-Gluon Plasma 3"*, edited by R. C. Hwa and X. N. Wang. (World Scientific, Singapore, 2004).

[34] Graziella Ferini, Maria Colonna, Massimo Di Toro, and Vincenzo Greco, PoS **HIGH-PTLHC08**, (2008).

[35] John Adams et al., Phys.Rev.Lett. **92**, 052302 (2004).

[36] S.S. Adler et al., Phys.Rev.Lett. **91**, 182301 (2003).

[37] Peter F. Kolb, AIP Conf.Proc. **698**, 694 (2004).

[38] P. Huovinen, P.F. Kolb, Ulrich W. Heinz, P.V. Ruuskanen, and S.A. Voloshin, Phys.Lett. **B503**, 58 (2001).

[39] V. Greco, C.M. Ko, and P. Levai, Phys.Rev. **C68**, 034904 (2003).

[40] Denes Molnar and Sergei A. Voloshin, Phys.Rev.Lett. **91**, 092301 (2003).

[41] J.D. Bjorken, FERMILAB-PUB-82-059-THY (1982).

[42] David A. Appel, Phys.Rev. **D33**, 717 (1986).

[43] Miklos F. Gyulassy, Ivan Vitev, Xin-Nian Wang, and Ben-Wei Zhang, in *"Jet quenching and radiative energy loss in dense nuclear matter. Published in Quark Gluon Plasma 3"*, edited by R. C. Hwa and X. N. Wang. (World Scientific, Singapore, 2003).

[44] Xin-Nian Wang, Nucl.Phys. **A750**, 98 (2005).

[45] Jorge Casalderrey-Solana and Carlos A. Salgado, Acta Phys.Polon. **B38**, 3731 (2007).

[46] Magdalena Djordjevic and Miklos Gyulassy, Nucl.Phys. **A733**, 265 (2004).

[47] Peter Brockway Arnold, Guy D. Moore, and Laurence G. Yaffe, JHEP **0206**, 030 (2002).

[48] Simon Turbide, Charles Gale, Sangyong Jeon, and Guy D. Moore, Phys.Rev. **C72**, 014906 (2005).

[49] R. Baier, Yuri L. Dokshitzer, Alfred H. Mueller, S. Peigne, and D. Schiff, Nucl.Phys. **B483**, 291 (1997).

[50] Nestor Armesto, Carlos A. Salgado, and Urs Achim Wiedemann, Phys.Rev. **D69**, 114003 (2004).

[51] Xiao-feng Guo and Xin-Nian Wang, Phys.Rev.Lett. **85**, 3591 (2000).

[52] A. Majumder, Enke Wang, and Xin-Nian Wang, Phys.Rev.Lett. **99**, 152301 (2007).

[53] Yuri L. Dokshitzer, Dmitri Diakonov, and S.I. Troian, Phys.Rept. **58**, 269 (1980).

[54] Alfred H. Mueller, Phys.Rept. **73**, 237 (1981).

[55] John C. Collins, Davison E. Soper, and George F. Sterman, Nucl.Phys. **B261**, 104 (1985).

[56] V.N. Gribov and L.N. Lipatov, Sov.J.Nucl.Phys. **15**, 438 (1972).

[57] Yuri L. Dokshitzer, Sov.Phys.JETP **46**, 641 (1977).

[58] Guido Altarelli and G. Parisi, Nucl.Phys. **B126**, 298 (1977).

[59] K.J. Eskola, H. Honkanen, C.A. Salgado, and U.A. Wiedemann, Nucl.Phys. **A747**, 511 (2005).

[60] K.J. Eskola and H. Honkanen, Nucl.Phys. **A713**, 167 (2003).

[61] S. Albino, B.A. Kniehl, and G. Kramer, Nucl.Phys. **B725**, 181 (2005).

[62] Bernd A. Kniehl, G. Kramer, and B. Potter, Nucl.Phys. **B582**, 514 (2000).

[63] K.P. Das and Rudolph C. Hwa, Phys.Lett. **B68**, 459 (1977).

[64] M. Adamovich et al., Phys.Lett. **B305**, 402 (1993).

[65] E.M. Aitala et al., Phys.Lett. **B371**, 157 (1996).

[66] Eric Braaten, Yu Jia, and Thomas Mehen, Phys.Rev.Lett. **89**, 122002 (2002).

[67] C. Gupt, R.K. Shivpuri, N.S. Verma, and A.P. Sharma, Nuovo Cim. **A75**, 408 (1983).

[68] J.A. Lopez, J.C. Parikh, and P.J. Siemens, Phys.Rev.Lett. **53**, 1216 (1984).

[69] T.S. Biro, P. Levai, and J. Zimanyi, Phys.Lett. **B347**, 6 (1995).

[70] T.S. Biro, P. Levai, and J. Zimanyi, J.Phys. **G28**, 1561 (2002).

[71] J. Zimanyi, T.S. Biro, T. Csorgo, and P. Levai, Phys.Lett. **B472**, 243 (2000).

[72] Rudolph C. Hwa, C.B. Yang, and R.J. Fries, Phys.Rev. **C71**, 024902 (2005).

[73] R.J. Fries, J.Phys. **G30**, S853 (2004).

[74] R.J. Fries, Berndt Muller, C. Nonaka, and S.A. Bass, Phys.Rev. **C68**, 044902 (2003).

[75] Carl B. Dover, Ulrich W. Heinz, Ekkard Schnedermann, and Joszef Zimanyi, Phys.Rev. **C44**, 1636 (1991).

[76] Yi Zhang, George Fai, Gábor Papp, Gergely G. Barnaföldi, and Péter Lévai, Phys. Rev. C **65**, 034903 (2002).

[77] Rainer J. Fries, Kyongchol Han, and Che Ming Ko, Nucl. Phys. **A956**, 601 (2016).

[78] S.S. Adler et al., Phys.Rev. **C69**, 034909 (2004).

[79] S.S. Adler et al., Phys.Rev.Lett. **91**, 072301 (2003).

[80] G. Agakishiev et al., Phys.Rev.Lett. **108**, 072302 (2012).

[81] J. Adams et al., Phys. Rev. Lett. **98**, 062301 (2007).

[82] G. Agakishiev et al., Phys. Rev. Lett. **108**, 072301 (2012).

[83] Rainer J. Fries, Vincenzo Greco, and Paul Sorensen, Ann. Rev. Nucl. Part. Sci. **58**, 177 (2008).

[84] Betty Abelev et al., Phys.Rev.Lett. **109**, 252301 (2012).

[85] G. Conesa Balbastre, J.Phys. **G38**, 124117 (2011).

[86] Betty Bezverkhny Abelev et al., Phys. Rev. Lett. **111**, 222301 (2013).

[87] D. D. Chinellato, J. Phys. Conf. Ser. **446**, 012055 (2013).

[88] Kyong Chol Han, Rainer J. Fries, and Che Ming Ko, J. Phys. Conf. Ser. **420**, 012044 (2013).

[89] K. Werner, Phys. Rev. Lett. **109**, 102301 (2012).

[90] Betty Bezverkhny Abelev et al., Phys. Lett. **B736**, 196 (2014).

[91] Zi-wei Lin and C. M. Ko, Phys. Rev. Lett. **89**, 202302 (2002).

[92] Betty Bezverkhny Abelev et al., Phys. Rev. **C91**, 024609 (2015).

[93] C. Peterson, D. Schlatter, I. Schmitt, and Peter M. Zerwas, Phys. Rev. **D27**, 105 (1983).

[94] H. van Hees, M. Mannarelli, V. Greco, and R. Rapp, Phys. Rev. Lett. **100**, 192301 (2008).

[95] W. M. Alberico, A. Beraudo, A. De Pace, A. Molinari, M. Monteno, M. Nardi, and F. Prino, Eur. Phys. J. **C71**, 1666 (2011).

[96] Pol Bernard Gossiaux, Joerg Aichelin, Marcus Bluhm, Thierry Gousset, Marlene Nahrgang, Sascha Vogel, and Klaus Werner, PoS **QNP2012**, 160 (2012).

[97] Thomas Lang, Hendrik van Hees, Jan Steinheimer, Yu-Peng Yan, and Marcus Bleicher, J. Phys. Conf. Ser. **426**, 012032 (2013).

[98] Min He, Rainer J. Fries, and Ralf Rapp, Phys. Rev. Lett. **110**, 112301 (2013).

[99] A. Beraudo, A. De Pace, M. Monteno, M. Nardi, and F. Prino, Eur. Phys. J. **C75**, 121 (2015).

[100] Santosh K. Das, Francesco Scardina, Salvatore Plumari, and Vincenzo Greco, Phys. Lett. **B747**, 260 (2015).

[101] Jan Uphoff, Oliver Fochler, Zhe Xu, and Carsten Greiner, Phys. Rev. **C84**, 024908 (2011).

[102] Jan Uphoff, Oliver Fochler, Zhe Xu, and Carsten Greiner, Phys. Lett. **B717**, 430 (2012).

[103] Santosh K. Das, Francesco Scardina, Salvatore Plumari, and Vincenzo Greco, Phys. Rev. **C90**, 044901 (2014).

[104] Shanshan Cao, Tan Luo, Guang-You Qin, and Xin-Nian Wang, Phys. Rev. **C94**, 014909 (2016).

[105] Salvatore Plumari, Wanda M. Alberico, Vincenzo Greco, and Claudia Ratti, Phys. Rev. **D84**, 094004 (2011).

[106] L. Adamczyk et al., Phys. Rev. Lett. **113**, 142301 (2014).

[107] Matteo Cacciari, Stefano Frixione, Nicolas Houdeau, Michelangelo L. Mangano, Paolo Nason, and Giovanni Ridolfi, JHEP **10**, 137 (2012).

[108] G. Ferini, M. Colonna, M. Di Toro, and V. Greco, Phys. Lett. **B670**, 325 (2009).

[109] M. Ruggieri, F. Scardina, S. Plumari, and V. Greco, Phys. Lett. **B727**, 177 (2013).

[110] David Tlusty, Nucl. Phys. **A904-905**, 639c (2013).

[111] Betty Abelev et al., JHEP **09**, 112 (2012).

[112] Cheuk-Yin Wong, Phys. Rev. **C25**, 1460 (1982).

[113] G. F. Bertsch and S. Das Gupta, Phys. Rept. **160**, 189 (1988).

[114] W. Cassing, V. Metag, U. Mosel, and K. Niita, Phys. Rept. **188**, 363 (1990).

[115] H. Kruse, B. V. Jacak, and Horst Stoecker, Phys. Rev. Lett. **54**, 289 (1985).

[116] Charles Gale, Sangyong Jeon, and Bjoern Schenke, Int. J. Mod. Phys. **A28**, 1340011 (2013).

[117] Salvatore Plumari, Giovanni Luca Guardo, Francesco Scardina, and Vincenzo Greco, Phys. Rev. **C92**, 054902 (2015).

[118] A. Adare et al., Phys. Rev. **C92**, 034913 (2015).

[119] Betty Bezverkhny Abelev et al., JHEP **06**, 190 (2015).